Institute for Geophysics, Astrophysics, and Meteorology
University of Graz
Atmospheric Remote Sensing and Climate System Research Group
ARSCliSys - on the art of understanding the climate system

IGAM/UniGraz Technical Report for ASA No. 2/2004

Final Report

on the

Envisat Project AO-620, Teil I (ENVI-ATCHANGE Programme)

"Atmospheric Change Analysis based on Spaceborne High-Vertical-Resolution T, q, O_3
Sounding involving GOMOS, MIPAS and GPS Limb Sensors"

Stellar Occultation Algorithms and Validation for GOMOS on Envisat and a Performance Analysis for the Complementary Solar Occultation Concept SMAS

by

Christian Retscher, Christoph Rehrl, Andreas Gobiet, and Gottfried Kirchengast
(IGAM/University of Graz, Graz, Austria)

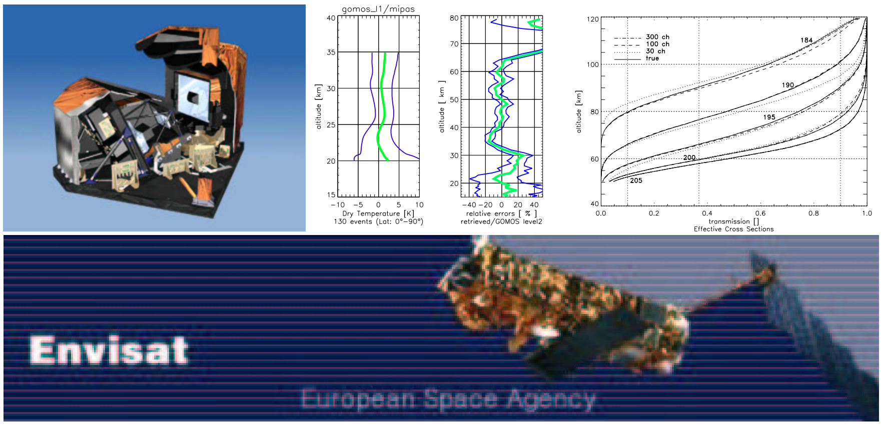

July 2004

Contents

Acronyms and Abbreviations

ACRI-ST	ACRI-ST Observations de la Terre et Sciences de l'Environnement
AFGL	Air Force Geophysics Laboratory
ASA	Austrian Space Agency
BIRA	Belgisch Instituut voor Ruimte-Aëronomie
BEAT	Basic Envisat Atmospheric Toolbox
BMVIT	Bundesministerium für Verkehr, Innovation und Technologie
CCD	Charge-Coupled Device
CFC	Chlorofluorocarbons
CHAMP	Challenging Minisatellite Payload
CIRA	Cooperative Institute for Research in the Atmosphere
CNRS	Centre National de la Recherche Scientifique
DARA	Deutsche Agentur für Raumfahrtangelegenheiten
DLR	Deutsches Zentrum für Luft- und Raumfahrt
ECMWF	European Centre for Medium Range Weather Forecast
EGOPS	End-to-end Occultation Sounding Simulator
ERS	European Remote Sensing Satellite
ESA	European Space Agency
ESL	Expert Support Laboratory
EUV	Extreme Ultraviolet
FMI	Finnish Meteorological Institute
GFZ	Geo Forschungs Zentrum Potsdam
GOME	Global Ozone Monitoring Experiment
GOMOS	Global Ozone Monitoring by Occultation of Stars
GPS	Global Positioning System
HRTP	High Resolution Temperature Profiles
IGAM	Institut für Geophysik, Astrophysik und Meteorologie
IASB	Institut d'Aéronomie Spatiale de Belgique
IMK	Institut für Meteorologie und Klimaforschung
LEO	Low Earth Orbit
METOP	Meteorological Operational Satellite
MIPAS	Michelson Interferometer for Passive Atmospheric Sounding
MSIS	Mass Spectrometer Incoherent Scatter
MUV	Middle Ultraviolet
NIVR	Nederlands Instituut voor Vliegtuigontwikkeling en Ruimtevaart
PI	Principal Investigator
POEM	Polar-Orbit Earth Observation Mission

RO	Radio Occultation
RMS	or rms, Root Mean Square
SA	Service d'Aéronomie
SATU	Star Acquisition and Tracking Unit
SCIAMACHY	Scanning Imaging Absorption Spectrometer for Atmospheric Chartography
SFA	Steering Front Assembly
SMAS	Sun Monitor and Atmospheric Sounder
SPOT	Satellite/Systéme Probatoire/Pour l'Observation de la Terre
UV	Ultraviolet
UVVIS	Ultraviolet and Visible

Executive Summary

The overall scientific objective of the ENVI-ATCHANGE Programme is the investigation of the global climate change monitoring potential of novel atmospheric sensors. Of particular interest is the GOMOS stellar occultation sensor together with the GPS radio occultation sensor on the German CHAMP satellite. The key parameters of interest are the fundamental atmospheric variables temperature and ozone. The goal is to arrive at quantitative conclusions on the climate monitoring utility of the sensors and methods involved, most important of the occultation technique, but also of high-resolution infrared spectro-radiometry as employed by the Envisat MIPAS sensor.

The understanding of actual atmospheric processes is of crucial importance to daily life and to future conditions on our home planet. The Earth's atmosphere cannot be seen as an isolated system, in contrary it interacts with the land mass, the ice sheets and the oceans. Envisat accounts for that with three separated instruments covering complementary wavelength ranges, resolutions and observed parameters: GOMOS, MIPAS, and SCIAMACHY use different measurement techniques, which makes an intercomparison of results interesting.

The stellar occultation technique in general was first described by P.B. Hays and R.G. Roble in 1968, who showed the possibility of using stars as a light source for extinction experiments. Five years later the first measurements of the Earth atmosphere were performed. In more recent times G.R. Smith and D.M. Hunton in 1990 showed a review of using absorptive occultations for planetary atmospheres. The investigation of the atmospheres of planets like Jupiter, Saturn and Uranus (and some of their satellites) was primarily driven by such remote sensing techniques. Absorptive occultation data bear a great capability of providing profiles of atmospheric key quantities.

The SMAS (Sun Monitor and Atmospheric Sounder) sensor concept utilizes the solar occultation method for temperature and ozone sounding in the mesosphere in order to complement the GOMOS soundings focusing on the stratosphere. While there is not yet a mission secured for SMAS, it is very fitting to study and thereby advance this highly complementary solar occultation concept together with work on the already existing GOMOS stellar occultation and GPS radio occultation sensors.

In this study we developed an optimal estimation algorithm for retrieval of atmospheric profiles from Envisat/GOMOS-measured level 1b transmission data. Ozone and temperature profiles were retrieved, which is the primary focus of the algorithm, though the whole processing chain is capable of retrieving other trace gases (e.g., NO_2) simultaneously.

We applied refractive occultation retrieval to bending angle data from GOMOS star tracker data (SFA/SATU) gaining refractivity, density, pressure, and temperature

profiles. This allows to improve the background fields required by the raytracing in the ozone retrieval part.

For the SMAS sensor concept the measured limb transmission data can be related to height profiles of the major absorbing species which are for the mesosphere, at middle ultraviolet wavelengths, molecular oxygen and ozone. Molecular oxygen profiles can be converted into pressure and temperature profiles. These data are of major importance for atmospheric analysis and process studies as well as for middle atmosphere modeling.

The approach adopted for an efficient retrieval of GOMOS ozone profiles has yielded encouraging results for simulated data, with ozone profile accuracy <3% from mid stratospheric up to high mesospheric regions. The application to real data clearly showed errors depending on transmission data quality and the selected star magnitude. The ozone retrieval performs best for bright stars at low and mid latitudes for heights from 25 km to 65 km. There the signal coming from the measurement enables to accurately see ozone structures. Ozone profiles at high latitudes suffer from occultations for dim stars only, which leads to biases and higher standard deviations. Comparisons with ECMWF ozone profiles show biases of up to 20% throughout all latitude regions.

Simulated temperature errors based on optimally initialized bending angle profiles show a high retrieval quality with errors of <2 K below 35 km and <1 K below 25 km. Real GOMOS data was then incorporated successfully into our retrieval. GOMOS SFA/SATU temperatures where compared to CHAMP, MIPAS, and ECMWF analysis data and showed rms-errors of 2 - 3 K from 25 km upwards. Below 25 km, temperature errors increase due to the small set of data reaching < 25 km as well as due to large fluctuations in SFA/SATU data.

The SMAS retrieval algorithm computes robustly atmospheric data within the required accuracy (temperature errors less than 2 K at 2 km vertical resolution up to a height of about 100 km), including a realistic noise level.

In this study the exploitation of data from two different occultation techniques was discussed and results show in general good performance. Stellar occultation with GOMOS on Envisat, once developed to monitor ozone, is now in a phase were data became reliable and one can start to use them for long term trend studies. For SMAS, a solar occultation sensor concept, we showed its feasibility and presented results of a simulation study, which left us with the desire for a real mission in future. Comparing both instruments there is still a lot of potential for cross-validation and exploitation of retrieval techniques.

Part 2 of the ENVI-ATCHANGE Programme ("Envisat Project AO-620, Teil II", proposed to ASA-BMVIT) is planned to start using the validated Envisat/GOMOS and MIPAS data for climate change monitoring and analysis.

1 Introduction

Once developed for exploring the atmospheres of planets in our solar system, remote sensing techniques are nowadays widely in use for mapping the Earth's gaseous envelope.

The Global Ozone Monitoring by Occultation of Stars (GOMOS) instrument (Chapter 2) is dedicated to perform high-accuracy altitude-resolved global ozone monitoring as well as measurements of other atmospheric trace gases and of temperature. Measurements are carried out within an altitude range of about 15 to 100 km.

We present results of a GOMOS temperature profile retrieval compared to CHAMP, MIPAS, and ECMWF analysis data. A second focus lies on the presentation of GOMOS ozone profiles, determined from GOMOS transmission data, validated against operational GOMOS ozone profiles and ECMWF analysis data. GOMOS temperatures are gained by exploiting pointing data of the Steering Front Assembly (SFA) and the Star Acquisition and Tracking Unit (SATU), which provide information on the refraction of the star light in the atmosphere and thus allow to derive refractive bending angle profiles. The bending angle profiles are then converted via refractivity and pressure profiles to temperature profiles (Chapter 3). According to the SFA sampling rate and retrieval algorithm requirements we performed the retrieval at 10 Hz including downsampled SATU data from 100 Hz. Bending angles were found with errors of $\sim 3\mu$rad. Statistical optimization of observed bending angles with model bending angles was used to provide adequate data quality for the Abel transform from the stratopause region upwards, which led to a significant gain in temperature retrieval accuracy up to 40 km height due to suppressed downward propagation of errors induced by Abel transform and hydrostatic integral. A validation setup based on co-located sets of CHAMP GPS occultation profiles, Envisat/MIPAS temperature profiles and analysis profiles of the European Centre for Medium-range Weather Forecasts (ECMWF) is discussed (Chapter 4). All three comparison sets show errors below 2 K from 20 km up to 40 km (Chapter 5). Below about 20 km the accuracy of GOMOS bending angle data is degraded, which leads to biases.

Together with the SFA/SATU-based refractivity and temperature retrieval, we developed an optimal estimation retrieval scheme for ozone (Chapters 3 and 4) using sensibly selected channels from the Spectrometer A transmission spectra within 260-340 nm and 602-634 nm. A validation set of GOMOS ozone is discussed (Chapter 5), where low and mid latitude profiles show biases as low as $\sim$5%. High latitude profile suffer from a small set of available stars contributing to the statistics.

For the planned Sun Monitor and Atmospheric Sounder (SMAS) instrument (Chapter 6) we discuss a realistic forward modeling and retrieval algorithm for temperature and ozone sounding (Chapter 7). The SMAS sensor concept employs the solar occultation technique and is primarily aiming at mesospheric profiles. The SMAS sensor provides self-calibrated transmission data, which allows for accurate derivation of molecular oxygen, and ozone density as well as temperature in the mesosphere.

The SMAS retrieval algorithm computes robustly atmospheric data within the required accuracy (temperature errors less than 2 K at 2 km vertical resolution up to a height of about 100 km), including a realistic noise level (Chapter 8).

A concise Summary and Conclusions Section, gathering the main findings of the study, completes the report.

Part I GOMOS Global Ozone Monitoring by Occultation of Stars

2 The Envisat polar platform

2.1 History and Overview

Initially a Polar Orbiting Earth Observation Mission (POEM-1) was planned as a combined mission with instruments for scientific application, research, and operational meteorology. Planned to be the successor of ERS it was designed for a polar platform. The development activities for the polar platform started in 1990, following the selection of the polar platform as a derivative of SPOT-4 by the council of the European Space Agency (ESA). At the Ministerial ESA council meeting in December 1993 POEM-1 was split into Envisat and METOP-1 and the development of the payload instruments for Envisat started.

The Envisat satellite has an ambitious and innovative payload that will ensure the continuity of the data measurements of the ERS satellites. Envisat data supports Earth science research and allows for monitoring of the evolution of changes of the Earth's environment and climate. Furthermore, the data will facilitate the development of operational and commercial applications. Envisat is the so far largest satellite build within an ESA contract.

In March 2002, after several years of delay, an Ariane 5 heavy-lift launcher successfully started with Envisat (Fig. 2.1) the advanced polar-orbiting Earth observation satellite. The satellite was lifted up to an altitude of ∼800 km above the Earth surface into a sun-synchronous orbit of 98.5° inclination and shall remain there operational for at least five years. The platform carries ten instruments on-board and provides measurements of the atmosphere, ocean, land, and ice. Amongst these instruments GOMOS, MIPAS and SCIAMACHY (Section 2.3) are dedicated to the observation of physical and chemical processes in the Earth atmosphere.

Another milestone in the story of a successful Envisat mission was achieved in spring 2003, when full data download from Envisat to its processing centers and to its users was guaranteed in near real time. Artemis, the Advanced Relay Technology Mission, was brought to its assigned geostationary orbit after a 18-month recovery operation from an orbit far lower than intended. A new ion propulsion system, combined with innovative operations of its chemical thrusters raised the satellite to its nominal geostationary position at 21.5 degrees East. Envisat transmits now about half of its sensor data in the Ka-band through Artemis straight to the Envisat data processing center at ESRIN, Italy. Data is also downloaded to the Envisat ground station and data processing center in Kiruna, Sweden. With the data relay satellite the Envisat data network has now been offered several important new capabilities.

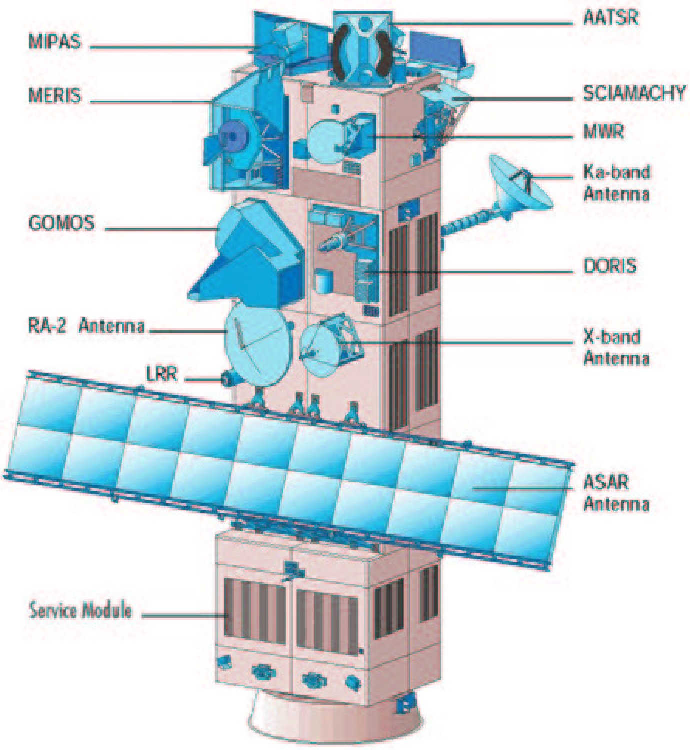

Figure 2.1. The Envisat satellite with all mounted instruments. The solar array is not shown. (http://envisat.esa.int)

2.2 Scientific Motivation

One of the most interesting and important research areas in atmospheric science is the determination of global ozone budgets and related temperature profiles [1, 2]. Since the 1970s the density of stratospheric ozone has decreased continuously. The most spectacular loss of ozone is reported above the South Pole, where the hole in the ozone layer now opens annually and is a dramatic symbol of our atmosphere's inherent unpredictability. Each year, when temperatures significantly fall in the beginning southern hemispheric winter and favored by singular meteorological circumstances such as polar winds, the ozone hole builds up and remains for several month with a minimum of column ozone in the antarctic spring around October. Nonetheless stratospheric ozone loss can be measured as well in the northern hemisphere, where industrialized countries are the main contributors to the global air pollution in general.

The culprits for such dramatic changes, in heights where the atmosphere is very sensitive to variations in the balance of several chemicals, were found to be chloroflurocarbons (CFCs) once developed as stable, non-polluting chemicals widely used in aerosols and refrigerators. But CFCs turned out to circulate throughout the globe and sometimes moved up into stratospheric regions. Whereas CFCs seemed to be inert in lower altitudes, they were broken up at high altitudes by intense solar ultraviolet radiation. The ozone layer is highly reactive with chlorine once liberated from CFCs. A single chlorine molecule has a devastating effect, taking apart a large number of ozone molecules.

The ozone layer protects the Earth and its biosphere from harmful UV radiation. The highest concentration of ozone is typically found between 25 and 35 km. More than 90% of the total atmospheric ozone contains the stratosphere where it is due to the absorption of UV radiation the main heat source. Decreasing ozone densities lead to lower temperatures and have therefore an impact on the climate system as well. The remaining 10% tropospheric ozone is known to have direct toxic effects on humans and on the vegetation.

Over time scales of days up to many years, depending on altitude, ozone is in balance between production and destruction. Molecular oxygen is photo-dissociated into two oxygen atoms

$$O_2 + h\nu \rightarrow 2O \tag{2.1}$$

shortly after recombined with molecular oxygen to form ozone,

$$O_2 + O + X \rightarrow O_3 + X \tag{2.2}$$

where X stands for any third body absorbing liberated excess energy. Ozone itself also splits due to dissociation

$$O_3 + h\nu \rightarrow O_2 + O \tag{2.3}$$

into molecular and atomic oxygen, where the latter almost immediately recombines to new ozone. This process is very effective in the absorption of solar energy in the UV, because no net loss of components is involved. Life on Earth is thought to be unimaginable without the removal of harmful radiation. While the ozone production cycle has only a small set of reactions, the depletion of ozone is far more complex due to the existence of a number of processes such as the hydrogen, the nitrogen and the chlorine cycle. Here we only gave a brief introduction to ozone chemistry. A far more elaborated discussion on ozone depletion can be found in [3].

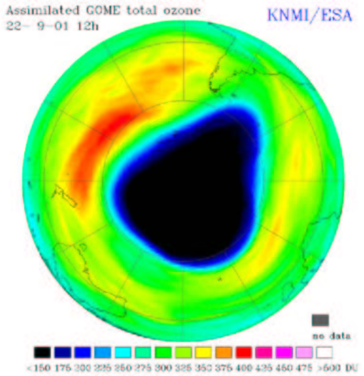

Figure 2.2. Ozone hole over the South Pole, September 2001. (http://envisat.esa.int)

From now 17 years ago the Montreal Protocol banned the production and use of CFCs, but too late to stop a 28 million km^2 ozone hole opening over Antarctica each spring. Since then science teams all over the world hope for a response of the ozone layer. The first sign of a reconstruction of stratospheric ozone may have been found in the now famous small-area ozone hole in 2002 followed by a split into two separated holes. In 2003 the ozone hole was back at its extension measured in years before 2002.

2.3 Atmospheric Chemistry Instruments

The understanding of actual atmospheric processes is of crucial importance to daily life and to future conditions on our home planet. The Earth's atmosphere cannot be seen as an isolated system, in contrary it interacts with the land mass, the ice shields an the oceans. Envisat accounts for that with three separated instruments covering complementary wavelength ranges, resolutions and observed parameters. GOMOS, MIPAS and SCIAMACHY use different measurement techniques which makes an intercomparison of results interesting. Possible flaws in instrument design, measurement principles and retrieved quantities are highly transparent to the user of the end product. This Section will introduce to the instrument design and the measurement principle of GOMOS and shortly outline the MIPAS and the SCIAMACHY instrument.

2.3.1 GOMOS

The Global Ozone Monitoring by Occultation of Stars instrument [4] is a completely new developed tool to investigate the Earth atmosphere. It exploits stellar occultation in the ultraviolet, visible and the near infrared bands. The major objective is the monitoring of upper tropospheric, stratospheric and mesospheric ozone. It therefore serves as a further high quality data acquisition unit in order to sharpen up our comprehension of the global ozone distribution.

GOMOS was first proposed in 1988 as an Announcement of Opportunity instrument dedicated to be a part of the Earth Observation Polar Platform Mission (c.f. 2.1), the former name of Envisat. In 1992 it was decided that GOMOS will be developed as an ESA-funded instrument.

Figure 2.3. Artist impression of the GOMOS instrument. (http://envisat.esa.int)

The sensor provides data on trace gases such as ozone, NO_2, NO_3, BrO, OClO, as well as O_2 and water vapor. A special instrument design makes it possible to measure reference atmospheric profiles under dark and bright limb conditions obtaining very good global coverage with about 300 high-quality profiles per day and a height resolution of about 1.5 km. GOMOS records the transmission of radiation passing the atmosphere along a path from the star to the instrument. The so-called spectrometer A measures ozone, NO_2, NO_3, BrO, and OClO within a wavelength range from 250 nm to 675 nm and provides a resolution of 1.2 nm. The Spectrometers B1 and B2 are sensitive within 756-773 nm and 926-952 nm, respectively, with 0.2 nm resolution, and were designed to measure O_2 and water vapor. GOMOS, once fixed on a star, measures transmitted stellar light, e.g. during a setting event and due to the motion of the satellite, the line of sight descends through the atmosphere, while the signal gets increasingly attenuated.

The instrument ensures high climate data quality obeying the principle of selfcalibration (normalized intensities), wherefore instrumental long-term drifts can be neglected. GOMOS faces other problems due to the fact that the measured stellar light is occasionally a subject to perturbations from other light sources. Scattered solar light under bright limb conditions, lunar radiation or light coming from auroral emissions into the atmosphere may dominate the stellar signal, what in turn makes an estimation of such radiation indispensable. Also signal scintillations due to the turbulent atmosphere can be challenging.

The performance of the CCD puts a technical constraint on the selection of the star signal, which has to be a stable flux at visual magnitude brighter than 4 with a star temperature range of favorably 3000 - 30000 K. By observing about 30 stars per orbit GOMOS can produce as much data daily as 360 separate ground stations.

In addition to the two spectrometers GOMOS is equipped with two fast photometers which account for measuring fast scintillations in the atmosphere. As a side product, but now reviewed for the next few month, photometer data can be used to get high resolution temperature profiles (HRTP).

2.3.2 MIPAS

Like GOMOS the Michelson Interferometer for Passive Atmospheric Sounding (MIPAS) is a complete new development. It is a Fourier transform spectrometer with a spectral range of 4.15 - 14.6 μm at a resolution of 0.2 nm for the measurement of high-resolution gaseous emission spectra at the Earth's limb. In the near to mid infrared many of the atmospheric trace-gases have important emission features and thus play a major role in atmospheric chemistry. The objective of MIPAS is the simultaneous and global measurement of geophysical parameters in the middle atmosphere. Stratospheric components like O_3, H_2O, CH_4, N_2O, and HNO_3 are determined. It enables the study of the chemical composition, the dynamics, and the radiation budget of the middle atmosphere. The horizontal resolution is found to be between 300 and 500 km along track. Another scientific goal of MIPAS is the measurement of precise temperature profiles. Thermal emissions in the infrared are very sensitive to temperature changes.

2.3.3 SCIAMACHY

The instrument is designed and built as a joint German/Dutch project funded by the German (DLR, formerly DARA) and Dutch (NIVR) national space agencies, with a contribution from Belgium BIRA/IASB. SCIAMACHY the Scanning Imaging Absorption Spectrometer for Atmospheric Cartography is the far more enhanced successor of GOME, which has been flying on ERS2 since 21 April 1995. SCIAMACHY is designed to measure sunlight, transmitted, reflected and scattered by the Earth atmosphere or surface. Samples are taken in the ultraviolet, visible and near infrared wavelength

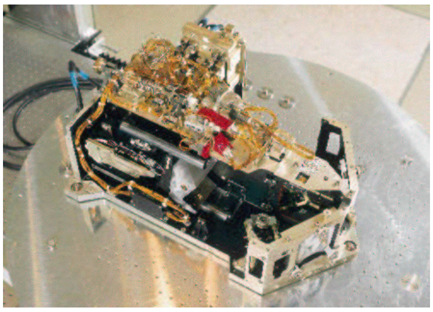

Figure 2.4. The MIPAS instrument. (http://envisat.esa.int)

region from 240 nm - 2380 nm at a spectral resolution of 0,2 nm - 1,5 nm. With different viewing geometries the absorption, reflection and scattering characteristics of the atmosphere are determined by measuring the extraterrestrial solar irradiance and the upwelling radiance. The ratio of such irradiances and radiances are inverted into profiles of densities and distribution of atmospheric constituents such as O_3, NO_2, H_2O, N_2O, CO, CO_2, CH_4, ClO, OClO, BrO, H_2CO, SO_2 and aerosols, known to absorb or scatter light, and the reflectance of the Earth's surface. Furthermore pressure and temperature profiles as well as the cloud cover and the cloud top height are determined. The MIPAS and SCIAMACHY instruments simultaneously show how CFCs and other trace gases make their way up from the lower troposphere across the boundary of the stratosphere.

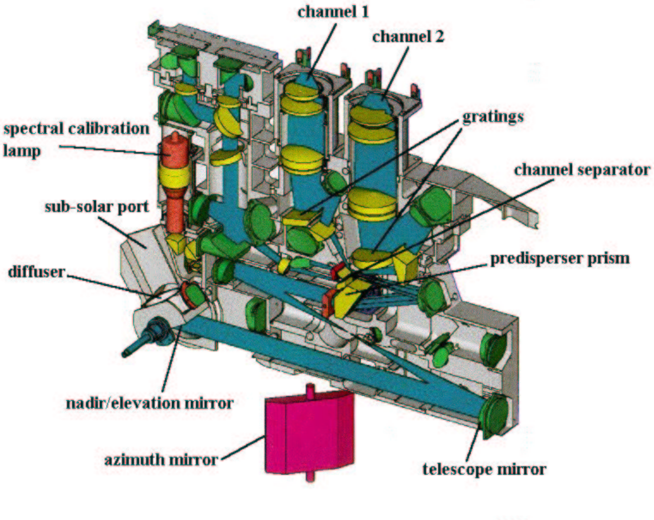

Figure 2.5. The SCIAMACHY instrument. (http://www-iup.physik.uni-bremen.de)

3 Retrieval of Atmospheric Parameters

3.1 Occultation Geometry and Forward Model Setup

The stellar occultation technique in general was first described by Hays and Roble in 1968 [5], who showed the possibility of using stars as a light source for extinction experiments. Five years later the first measurements of the Earth atmosphere were performed. In recent times Smith and Hunton [6] showed a review of using absorptive occultations for planetary atmospheres. The investigation of the atmospheres of planets like Jupiter, Saturn and Uranus (and some of its satellites) was primarily driven by such remote sensing techniques.

A formulation of an appropriate signal propagation geometry is of major importance in order to develop a realistic forward model procedure. We use a realistic yet fast raytracing algorithm, which solves the refractive raypath problem

$$\frac{d^2\mathbf{x}}{d\tau} = n(\mathbf{x})\nabla n(\mathbf{x}) \tag{3.1}$$

with the star and the satellite position as boundary conditions. The $n(\mathbf{x})$ denote the refractivity field of the used atmospheric model (e.g. MSISE-90 [7, 8, 9]), while $d\tau$ is the along-ray arc length divided by the refractivity n.

The atmospheric transmission is given by Beer-Bouguer-Lambert's law, at each frequency of interest ν, as

$$T_\nu = \frac{I_\nu(s)}{I_\nu(0)} = \exp\left[- \int_{s_1}^{s_2} \sum_i n_i(s')\sigma_{i\nu}(s')ds' \right]. \tag{3.2}$$

The transmission T_ν is a ratio of the radiation intensity measured in the atmosphere, $I_\nu(s)$, relative to the one, $I_\nu(0)$, measured above (height ~120 km) the atmosphere. The integral is carried out along a refracted ray path s from the star s_1 to the sensor s_2. In our context the number densities n_i and the cross sections $\sigma_{i\nu}$ are associated with the species ozone, NO_2 and NO_3, respectively. In order to reflect the bulk medium, especially important in the lower stratosphere, a factor for the bulk air density with the Rayleigh scattering cross section was introduced as well. In this work a term for the aerosol extinction was neglected, nevertheless, we plan to introduce it in future refinements. Since stars can be assumed to provide a point signal, no further integration over a finite field of view has to be carried out, which is in turn indispensable for solar or lunar occultations.

3.2 Ozone Retrieval

Having a forward model established, we have to find an inverse connection between measurements (transmission data) and targeted state (ozone profile) of the atmosphere. Discrete inverse theory provides such a framework [10], where the forward model can be seen as an algebraic mapping of the state space into the measurement space.

3.2.1 Optimal Estimation

We introduce an operator $\mathbf{K}$, which here will be the Jacobian matrix with the dimension $m \times n$ for m measurements and n elements of the state vector. By taking the measurement error ε into consideration the forward modeling reads

$$\mathbf{y} = \mathbf{K}\mathbf{x} + \varepsilon. \tag{3.3}$$

The sensitivity of measured transmissions $\mathbf{y}$ to the state $\mathbf{x}$, the ozone density profile, can be interpreted as "weighting functions" and seen represented by the rows of $\mathbf{K}$. Because of the generally non-linear Eq. (3.3), it is obvious that a straightforward solution for $\mathbf{x}$ by direct inversion is not feasible. The direct inverse mapping, if $\mathbf{K}(\mathbf{x}) = \mathbf{K} \cdot \mathbf{x}$ (e.g., linearity applies), would be

$$\mathbf{x}_r = \mathbf{K}^{-g}\mathbf{y}, \tag{3.4}$$

where $\mathbf{K}^{-g}$ denotes a general inverse matrix and $\mathbf{x}_r$ is the retrieved state. As the problem of interest here is ill-posed at high altitudes due to low signal to noise ratio (it may also be over-determined if we use more measurements than unknown states; $m > n$), we cannot directly employ Eq. (3.4) but rather constrain the solution by incorporating sensible *a priori* information. The Bayesian approach is the method of choice to solve such inverse problems perturbed by noise, where we have rough but reliable prior knowledge of the behavior of a state of interest. We can enhance this prior knowledge in a consistent way by incorporating the measurements.

If the problem is only moderately non-linear we can use a Gauss-Newton method (omitting small residual terms from Newtonian iteration, when applying on non-linear cases) for an iterative approach to an optimal solution. Assuming Gaussian probability distributions and a linearized forward model, the primary task of a retrieval method is to find a state by satisfying optimal criteria from an ensemble of states which agree with the measurement within experimental errors.

Here we make use of a fast converging iterative optimal estimation algorithm [10],

$$\mathbf{x}_{i+1} = \mathbf{x}_{ap} + \mathbf{S}_i \mathbf{K}_i^T \mathbf{S}_\varepsilon^{-1} \Big[(\mathbf{y} - \mathbf{y}_i) + \mathbf{K}_i \left(\mathbf{x}_i - \mathbf{x}_{ap}\right) \Big] \tag{3.5}$$

with the associated retrieval error covariance matrix

$$\mathbf{S}_i = \left(\mathbf{K}_i^T \mathbf{S}_\varepsilon^{-1} \mathbf{K}_i + \mathbf{S}_{ap}^{-1} \right)^{-1}. \tag{3.6}$$

In Eq. (3.5), $\mathbf{x}_{i+1}$ is the retrieved, $\mathbf{x}_{ap}$ the *a priori* profile, $\mathbf{y}$ the measurement vector, and $\mathbf{y}_i = \mathbf{K}(\mathbf{x}_i)$ the forward-modeled measurement vector. Key ingredients of Eq. (3.6) are the *a priori* covariance matrix $\mathbf{S}_{ap}$ and the measurement error covariance matrix

$\mathbf{S}_\varepsilon$ (c.f. below). The Jacobian (weighting) matrix $\mathbf{K}_i$ represents the mapping involved. Index i is the iteration index, which is started by using $\mathbf{x}_0 = \mathbf{x}_{ap}$.

The raytracer-simulated actual transmission measurements $\mathbf{y}$, where superimposed by stochastic error realizations ε (cf. Eq. 3.3) consistent with the $\mathbf{S}_\varepsilon$ matrix. This was done with the "error pattern method" outlined below for $\mathbf{S}_{ap}$. The forward-modeled measurement vector estimate at any iteration step i, $\mathbf{y}_i = \mathbf{K}(\mathbf{x}_i)$, is used without modification, however.

In general, an error analysis and characterization of atmospheric profile retrievals is an important task for every sensor. Bayesian optimal estimation provides a very suitable framework for this purpose also in case of occultation data [11].

A priori Covariance Matrix

For the elements of $\mathbf{x}_{ap}$ we considered typical errors expected in prior ozone and NO_2 profiles and assumed uncertainties of 30% and 40%, respectively, for the diagonal elements. Off-diagonal elements were modeled by an exponential drop-off correlation of the form (c.f. Fig. 3.1)

$$S_{ij} = \sigma_i \sigma_j \exp\left[-\frac{|z_i - z_j|}{L}\right], \tag{3.7}$$

where z_i and z_j denote the height levels between which the covariance is expressed, and where L denotes a correlation length set to 6 km in order to reflect the fact that prior profiles are usually fairly smooth at scales smaller than an atmospheric scale height. Measured ozone profiles may in turn show strong laminar structures with much smaller scales. The standard deviation σ_i at a specific height level corresponds to $\sigma_i = (\mathbf{S}_{ap})_{ii}^{1/2}$.

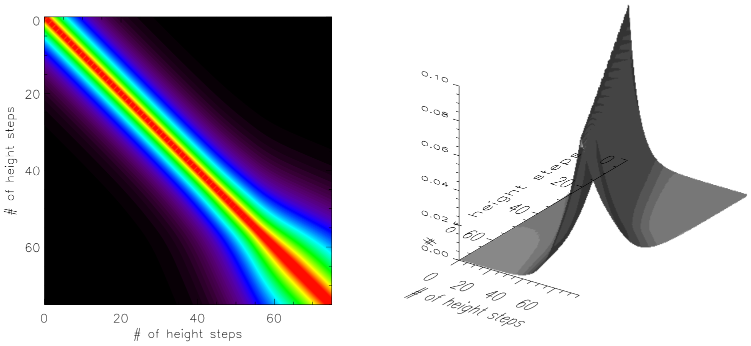

Figure 3.1. Typical *a priori* ozone covariance matrix with 6 km correlation length and exponential drop-off.

Error Covariance Matrix

The $\mathbf{S}_\varepsilon$ matrix was designed by adopting a 1% standard error at unity transmission and increasing errors with decreasing transmission according to the square-root law (photon detection noise), e.g.,

$$(\mathbf{S}_\varepsilon)_{jj} = \frac{0.01}{\sqrt{y_j}}. \tag{3.8}$$

No interchannel correlation was assumed, thus the off-diagonal elements were set to zero. These error assumptions roughly reflect the measurement error specifications of the GOMOS sensor [12].

Error Pattern Method

The method was applied for the calculation of *a priori* and measurement error vectors in general, but for simplicity reasons it is only outlined in the notation of the *a priori* profile.

The *a priori* profiles $\mathbf{x}_{ap}$ where derived by superimposing on the "true" state $\mathbf{x}$ error realizations consistent with the *a priori* error covariance matrix $\mathbf{S}_{ap}$. For this purpose we exploits the fact that one can decompose $\mathbf{S}_{ap}$ (e.g., [10, 13]) into so-called error patterns obeying $\mathbf{e}_i = \sqrt{\lambda_i}\mathbf{l}_i$. The error patterns $\mathbf{e}_i$ (c.f. Fig. 3.2) are the eigenvectors $\mathbf{l}_i$ of $\mathbf{S}_{ap}$ weighted by the square-root of the eigenvalues λ_i. In order to construct $\mathbf{x}_{ap}$ statistically consistent with $\mathbf{S}_{ap}$, one adds an error vector $\sum_i a_i\mathbf{e}_i$ to the "true" state $\mathbf{x}$, where the scalar coefficients a_i are normal random deviates drawn from a normalized (zero mean and unit variance) Gaussian distribution.

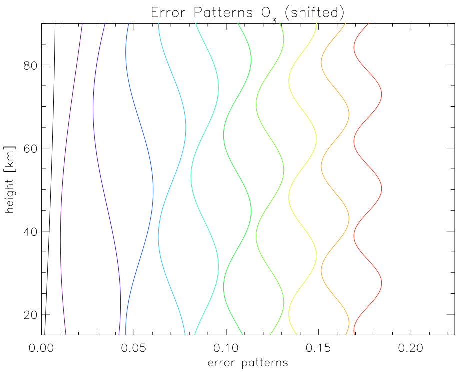

Figure 3.2. An example of error patterns (scaled eigenvectors) for a covariance matrix.

3.3 Temperature Retrieval

Light coming from stellar sources not only undergoes a refractive bending before the signal gets measured, moreover it may be influenced by turbulence in atmospheric layers. The so-called scintillation effects have their origins in differing temperature, refractive indices or velocities. Especially at heights above 30 km, this and other noise sources severely degrade the measured signal. Temperature profiles are calculated by applying an inverse Abel transform. Here a sensible use of good-quality bending angle data for high-altitude initialization is needed.

3.3.1 Abel Transform

In this work, in addition to ozone retrieval, we perform a temperature retrieval based on bending angles profiles, which is well known for radio occultation measurements (e.g. [14, 15, 16]).

Bending angles are extracted from SFA and SATU data gained by the GOMOS sensor. These data products present the movement of the whole CCD within an elevation angle of $61.7^\circ - 69^\circ$ and $11^\circ - 91^\circ$ in the azimuthal direction with a sampling rate of 10 Hz for the SFA. The star image is kept inside the CCD with with a sampling of 100 Hz and errors of $\pm\ 10\mu$rad from the central position.

Once we have a total bending angle profile α and accompanying impact parameters a we can apply an inverse Abel transform [14]

$$n(z) = \exp\left[\frac{1}{\pi}\int_{\alpha=\alpha(a_0)}^{\alpha=0} \ln\left(\frac{a(\alpha)}{a_0}\sqrt{\left(\frac{a(\alpha)}{a_0}-1\right)}\right) d\alpha\right] \tag{3.9}$$

written here in a favorable from for numerical use by avoiding poles. The $\alpha(a_0)$ and a_0 are the bending angle respectively impact parameter associated with height z, the bottom height of the Abelian integration extending over the height domain above z. The refractivity follows with $N(z) = (n(z) - 1) \times 10^6$, which can be converted into pressure p by integrating the hydrostatic equation. A temperature profile can be subsequently derived from p and N by the equation of state (ideal gas law).

At heights above 30 km, where the bending angles become small due to the increasingly tenuous atmosphere, the decreased signal-to-noise ratio calls for suitable high-altitude initialization of the bending angle profiles in order to feed the Abel transform Eq. (3.9) with adequate data.

3.3.2 Statistical Optimization

The statistical optimization [15] optimally combines measured and background (*a priori*) bending angle profiles leading to the most probable bending angle profile [16]. An optimal solution is feasible via

$$\alpha_{opt} = \alpha_b + \left(\mathbf{B}^{-1} + \mathbf{O}^{-1}\right)^{-1} \mathbf{O}^{-1}(\alpha_o - \alpha_b), \tag{3.10}$$

where α_b is the background and α_o the observed bending angle profile, respectively. The matrices $\mathbf{B}$ and $\mathbf{O}$ express the background and the observation error covariances, respectively. Similar to Eq. (3.7) we define

$$B_{ij} = \sigma_i \sigma_j \exp\left[-\frac{|a_i - a_j|}{L}\right], \tag{3.11}$$

with impact parameters a at different height levels i and j. The correlation length L was set to 6 km for $\mathbf{B}$, while we find $L = 1$ km appropriate for $\mathbf{O}$, which used the same form as Eq. (3.11). As a background profile we chose a CIRA-86 climatology. Background errors σ_i were assumed to be 20% in line with radio occultation literature (e.g. [16, 17]). The observation errors were estimated from the rms deviation of the observed data from the background at high altitudes (70 - 80 km), where noise dominates the measured signal. Details on the statistical optimization scheme used are found in [17, 18], which also provides further information on the full retrieval chain from bending angle to temperature.

3.4 Error Statistics

We give a small introduction into error statistics applied throughout this report (c.f. [19, 20]). We assume having a set of measurements $\mathbf{x}_i$ out of an ensemble $\mathbf{x}$ of possible states in a system of interest, then we can find estimators of several statistical properties like the mean value the variance and the standard deviation. In general such quantities are moments of distributions of random variables.

An appropriate estimator for the mean value (first moment) and for the variance (second moment) can be found with

$$\hat{\mathbf{x}} \equiv \frac{1}{n} \sum_{i=1}^{N} \mathbf{x}_i, \quad \hat{\sigma}^2 \equiv \frac{1}{n} \sum_{i=1}^{N} \left(\mathbf{x}_i - \hat{\mathbf{x}}\right)^2 . \tag{3.12}$$

Having defined such estimators we can now find equivalent definitions for differences of profiles

$$\Delta\mathbf{x} = \mathbf{x}_m - \mathbf{x}_r, \tag{3.13}$$

where $\mathbf{x}_m$ represents the measurement and $\mathbf{x}_r$ a corresponding reference profile. Here entities are more generally given in a vector notation due to the fact that we are interested in vertical distributions of geophysical quantities.

We are now interested in expectation values of our estimators in Eq. 3.12. The expectation value of $\hat{\mathbf{x}}$ is

$$\langle \hat{\mathbf{x}} \rangle = \frac{1}{n} \sum_{i=1}^{N} \langle \mathbf{x}_i \rangle = \langle \mathbf{x} \rangle \equiv \mu_{\mathbf{x}}, \tag{3.14}$$

while for the variance follows

$$\langle \hat{\sigma}^2 \rangle = \frac{1}{n} \sum_{i=1}^{N} \left\langle \left(\mathbf{x}_i - \hat{\mathbf{x}}\right)^2 \right\rangle = \sigma_{\mathbf{x}}^2 - \sigma_{\hat{\mathbf{x}}}^2 = \frac{n-1}{n} \sigma_{\mathbf{x}}^2, \tag{3.15}$$

where $\sigma_{\mathbf{x}}^2$ and $\sigma_{\hat{\mathbf{x}}}^2$ are the variances for $\mathbf{x}$ and $\hat{\mathbf{x}}$, respectively. Obviously Eq. 3.15 does not appropriately represent the expected mean value for the variance. We therefore have to correct Eq. 3.15 by the factor $n/(n-1)$.

Superseding now $\mathbf{x}_i$ in Eq. 3.12 by $\Delta\mathbf{x}$ we find an estimator for a so-called bias profile

$$\hat{\mathbf{b}} \equiv \frac{1}{n} \sum_{i=1}^{N} \Delta\mathbf{x}. \tag{3.16}$$

Applying this to Eqs. 3.12 and 3.15 we find

$$\hat{\mathbf{s}}^2 \equiv \frac{n}{n-1} \hat{\sigma}^2 = \frac{1}{n-1} \sum_{i=1}^{N} \left(\Delta\mathbf{x} - \hat{\mathbf{b}}\right)^2 , \tag{3.17}$$

where $\hat{\mathbf{s}}$ is an estimator of the standard deviation of a bias-free profile

$$\mathbf{x}_f = \Delta\mathbf{x} - \hat{\mathbf{b}}. \tag{3.18}$$

More generally one can now define an error covariance matrix

$$\mathbf{C} = \frac{1}{n-1} \sum_{i=1}^{N} \mathbf{x}_f \mathbf{x}_f^T, \tag{3.19}$$

where the diagonal elements are variances at different height levels k, while off-diagonal elements stand for covariance elements. Another quantity often used is the rms

$$\mathbf{r} = \sqrt{\hat{\mathbf{b}}^2 + \hat{s}_{kk}}. \tag{3.20}$$

Finally we define an error correlation matrix

$$\mathbf{R} = \frac{s_{kl}}{\sqrt{s_{kk} s_{ll}}}, \tag{3.21}$$

where off-diagonal elements denote vertical error cross-correlations.

4 Validation Setup

This chapter is dedicated to a resume of setups for IGAM retrieval schemes for ozone and temperature profiles, based on GOMOS data. The main focus lies on the comparison of GOMOS level 1b data with CHAMP/RO, MIPAS and ECMWF analysis data. Besides a comparison of GOMOS/HRTP (level 2) data was prepared and discussed in [18]. The GOMOS/HRTP are subject to a code review and error analysis within an ESA-study, which is led by ACRI-ST in collaboration with SA/CNRS, BIRA/IASB, FMI and IGAM/UniGraz.

4.1 Ozone Retrieval

For the IGAM ozone retrieval GOMOS transmission spectra and geolocation data were taken and processed with an optimal estimation technique (c.f. Section 3.2). The forward model and its derivative are iteratively called and form the core of the retrieval. The model is capable of processing real and simulated data providing a basis for the feasibility of the whole scheme. Once we were convinced in the simulated model [21] it had to be adapted in order to accept non smoothed transmission data input.

4.1.1 Simulated Data

We first prepared a study on ozone and NO_2 data by using an end-to-end simulator (EGOPS [22, 23]) providing quasi-true Envisat orbits, geodetical positions of Envisat as well as the approximated position of an occulted sample star. One selected occultation event (Fig. 5.1) is shown in the next chapter. The star image was modeled in a simplified manner only providing light at different wavelengths, where a further dependence of the model on the star temperature was not considered.

Physical interpretations and realizations of scintillation and dilution effects were here neglected in the first place, but resulting modeled transmissions account for these effects with an imposed random error (forward model error gained by the error pattern method c.f. Section 3.2.1) with reasonable size of ∼1%.

The $\mathbf{S}_{ap}$ were chosen to have a standard deviation of 30% for ozone and 40% for NO_2, respectively. The error characteristic was designed as outlined in Section 3.2.1. As a basis for quasi-true and *a priori* ozone and NO_2 number densities we used CIRA-86 and MSISE-90 data. Cross sections were taken form the official temperature dependent GOMOS cross section database.

The main reason why NO_2 was included into our retrieval scheme is given by its high absorption of the star image in wavelength regions between 350 and 450 nm. This

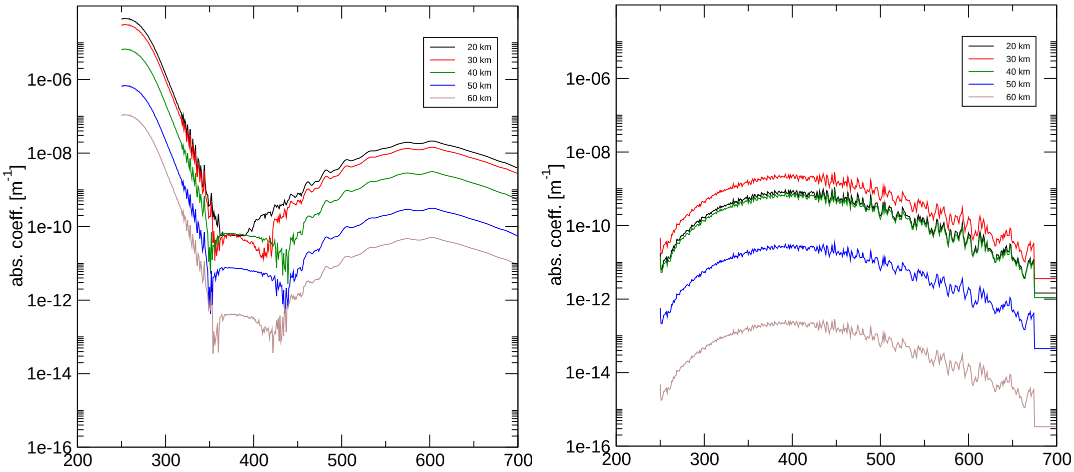

Figure 4.1. Absorption coefficients of ozone (left) and NO_2 (right) at typical GOMOS wavelengths from 250 - 700 nm at heights of 20, 30, 40, 50, and 60 km.

coincides with the region of low signal absorption by ozone. Fig. 4.1 shows ozone and NO_2 absorption coefficients for all GOMOS wavelengths. Our simulated joint ozone-NO_2 retrieval perfectly reflects the effects of the NO_2 interference in this regime, nevertheless in this validation setup NO_2 was not retrieved with considerable quality.

In this simulation study we restricted ourselves to include a small set of well selected wavelength channels perfectly placed to cover ozone absorption bands [2] such as the Hartley (200 - 310 nm), the Huggins (310 - 400 nm) and the Chappuis band (400 - 850 nm), which is especially important for absorptions below 25 km. Our set of channels (260, 280, 288, 295, 302, 309, 317, 328, 334, 602 and 634 nm) therefore provides the maximum possible information coming from the measurement by simultaneously reducing the elapsed time to retrieve one profile.

4.1.2 Real GOMOS Data

For the retrieval of real ozone and NO_2 profiles we used official GOMOS level 1b and level 2 data provided by ACRI-ST in Sophia Antipolis, France. ACRI-ST is one of four (ACRI-ST, SA/CNRS, FMI, IASB) expert support laboratories (ESL) for the GOMOS instrument. The data was then reprocessed with the so-called BEAT-software (c.f. http://www.science-and-technology.nl/beat/), which is now available for reading raw data as well as displaying graphs of measured data. BEAT is an ESA-funded software tool developed to ease the life for users of Envisat atmospheric instruments (GOMOS, MIPAS, and SCIAMACHY) data. The GOMOS data products are stored in several files shown in Tab. 4.1, where we used `GOM_TRA_1` and `GOM_NL__2` products corresponding to our previously introduced notation of GOMOS level 1b and level 2 data.

This study summarizes retrieved data for three periods (Tab. 4.2), which includes more than 1700 single occultation events. In this report we reduced the set of available data due to large errors in level 1b transmission and reference level 2 ozone data. Such errors significantly diminish the performance of our retrieval. The remaining transmission profiles where first selected by arguments of an optimal set of wavelengths

`GOM_TRA_1P`	Geolocated Calibrated Transmission Spectra
`GOM_LIM_1P`	Geolocated Calibrated Background Spectra (Limb)
`GOM_NL__2P`	GOMOS Temperature and Atmospheric Constituents Profiles
`GOM_EXT_2P`	GOMOS Residual Extinction
`GOM_RR__2P`	GOMOS Extracted Profiles for Meteo Users

Table 4.1. GOMOS level 1b/2 data products.

September	2002	20 - 27
October	2002	11 - 13
December	2002	02

Table 4.2. Periods with available GOMOS data.

(c.f. Section 4.1.1) and then adapted to our needs of retrievals for upper and lower stratospheric ozone profiles. The quality of transmission data is strongly dependent on the star magnitude. Light coming from bright stars is able to penetrate the Earth's atmosphere down to lower heights than light stemming from weak stars. In general the penetration depth of light into the atmosphere is known to be wavelength dependent.

Moving Average and Bias Correction

Once we have selected an optimal set of profiles due to the upper arguments we had to smooth transmission data for better retrieval performance. A moving average calculation was performed for every height step in the profile. A given sequence for one selected wavelength l and height level i dependent transmissions $\{T_{li}\}_{i=1}^{N}$ is replaced by a new sequence of smoothed transmissions $\{(T_s)_{li}\}_{i=1}^{N-n+1}$ with

$$(T_s)_{li} = \frac{1}{\sum_n k_n} \sum_{j=i}^{i+n-1} k_j T_{lj}. \tag{4.1}$$

The average was taken by n subsequences of T_{lj} each weighted with different k_j. In general moving averages are given with equal weights. Here the weights were chosen such that $\sum_n k_n = 1$. For a subsequence of $n = 5$ we find weights with $k_n = \frac{1}{2 \cdot 5}[1, 2, 4, 2, 1]$, where k_3 can always be seen as the weight for the original T_i before taking the mean.

After a real transmission profile has been smoothed it was then compared to a modeled transmission profile and corrected for large biases. Such biases exist due to a different forward model realization. Neglecting the majority of measured (and modeled beforehand) transmissions is intrinsic to our model, where we only select a small subset of available data. A further reason why we observe deviations from measured transmissions lies in the physics of the forward model itself, where e.g. Mie scattering was not considered for this study. Nonetheless after correcting for inherent biases the results show the expected behavior.

4.1.3 ECMWF Analysis Data

ECMWF T511L60 analysis data was taken for the same period, where GOMOS data was available. ECMWF T511L60 ozone data allows for a comparison with GOMOS ozone data up to ∼60 km. Ozone is fully integrated into the ECMWF forecast model and analysis system as an additional three-dimensional model and analysis variable similar to humidity. The ECMWF forecast model includes a prognostic equation for the ozone mass mixing ratio with a parameterization of sources and sinks of ozone.

4.2 Temperature Retrieval

The temperature retrieval follows a new approach for occultations in the optical spectral range, but is a method well known in the Radio Occultation (RO) community. Once we have bending angles exploited from real measurements, data was statistically optimized (c.f. Section 3.3.2) and then used to gain refractivity and temperature profiles via Abel transform (c.f. Section 3.3.1). GOMOS provides SFA/SATU internal mirror position data, which had to be further processed in order to get real bending angles [24, 25].

Tab. 4.3 and 4.4 show latitude separated sets of total available GOMOS, CHAMP, MIPAS and ECMWF data, as well as coincidences between these products. The coincidence interval is defined such that compared temperature profile must lie within 300 km of distance and the occultation time shall not differ for more than 3 hours.

	0°to ± 30°	±30°to ± 60°	±60°to ± 90°	Total
GOMOS	698	699	322	1719
CHAMP	1280	1558	1261	4099
MIPAS	1368	1380	1474	4222
ECMWF	698	699	322	1776

Table 4.3. Numbers of profiles in total sets of available GOMOS, CHAMP, MIPAS and ECMWF data in the period September 20 - 27, October 11 - 13 and December 2, 2002. The sets were separated into low, mid and high latitude regions.

	0°to ± 30°	±30°to ± 60°	±60°to ± 90°	Total
GOMOS - CHAMP	22	33	37	92
GOMOS - MIPAS	141	30	27	198
GOMOS - ECMWF	719	735	322	1776

Table 4.4. Numbers of profiles in coincidence sets of available GOMOS, CHAMP, MIPAS and ECMWF data in the period September 20 - 27, October 11 - 13 and December 2, 2002. The sets were separated into low, mid and high latitude regions.

4.2.1 GOMOS

The GOMOS level 1b/2 data product is separated into three latitude regions, low (0°to ± 30°), mid (±30°to ± 60°) and high (±60°to ± 90°) in order to account for different mean states of the atmosphere at different latitudes. A global set of retrieved data is given as well, where influences of different latitude regions to the quality of an overall profile can be seen. GOMOS SFA/SATU (level 1b) data used here and high resolution temperature profiles (HRTP) in general suffer from different influences. SFA/SATU data often show much larger errors than primarily assumed. The data set, which was

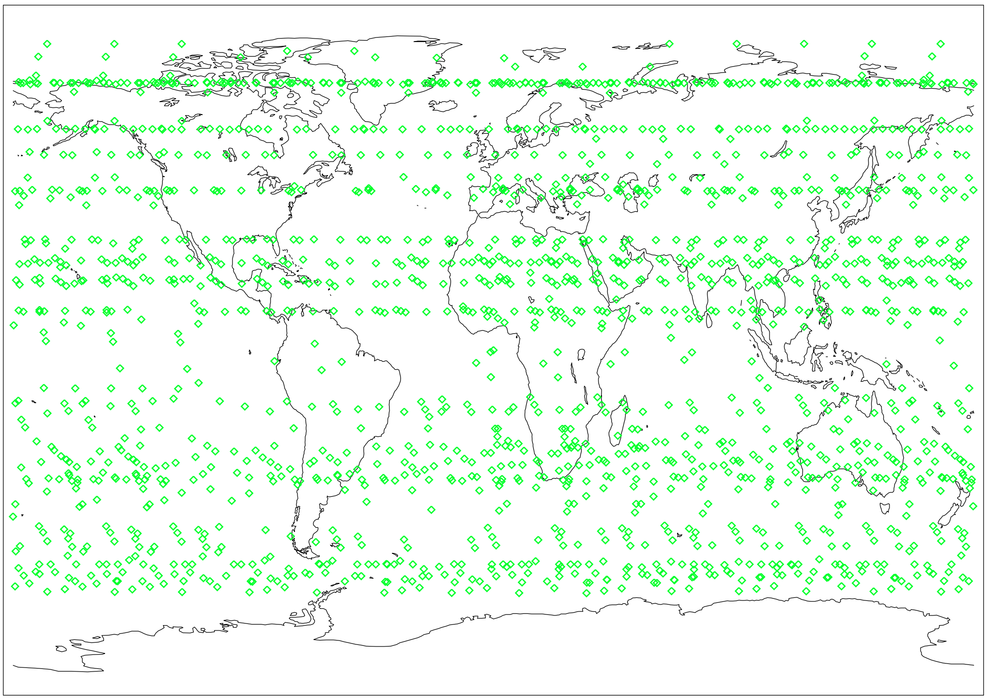

Figure 4.2. Locations where GOMOS measurements were performed. The graph displays 1719 occultation profiles available for days: September 20 - 27, October 11 - 13 and December 2, 2002. The lack of data at high altitudes is evident.

provided for this study, only includes a small set of occulted stars, what makes it especially difficult to ensure good retrieval quality at high latitudes (Fig. 4.2).

4.2.2 CHAMP/GPS

For this study we used CHAMP data provided by GFZ in Potsdam, Germany. Phase delays from the CHAMP level 2 (version 2) data served as input into our retrieval [18], which had ECMWF data as background information. Once atmospheric profiles were retrieved we separated our data set into three latitude regions (c.f. Section 4.2). The success of ionospheric corrections can be seen much better when looking at latitude subsets. Low latitudinal effects such as the equatorial anomaly, the spherical assymetry and small scale structures cause perturbations in the RO profile. In turn dry conditions in the high-latitude troposphere favor a good quality RO retrieval, but have only minor influence in the comparison to GOMOS data. GOMOS data in the selected subset seldom reaches tropospheric heights with reasonably quality. From 4099 CHAMP profiles we found 92 profiles, where our coincidence intervals with GOMOS data were reached.

4.2.3 MIPAS

Operational MIPAS level 1b data was reprocessed by IMK in Karlsruhe, Germany. From a total of 6755 available occultations with we had to reduce the data set to 4222

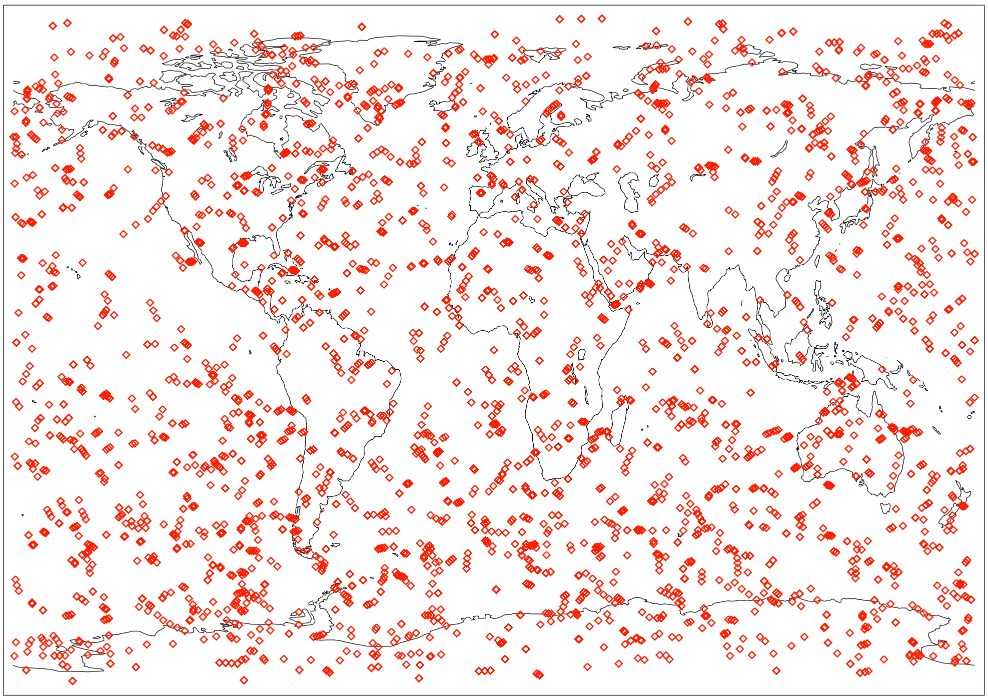

Figure 4.3. Locations where CHAMP measurements were performed. The graph displays 4099 occultation profiles available for days: September 20 - 25, 2002.

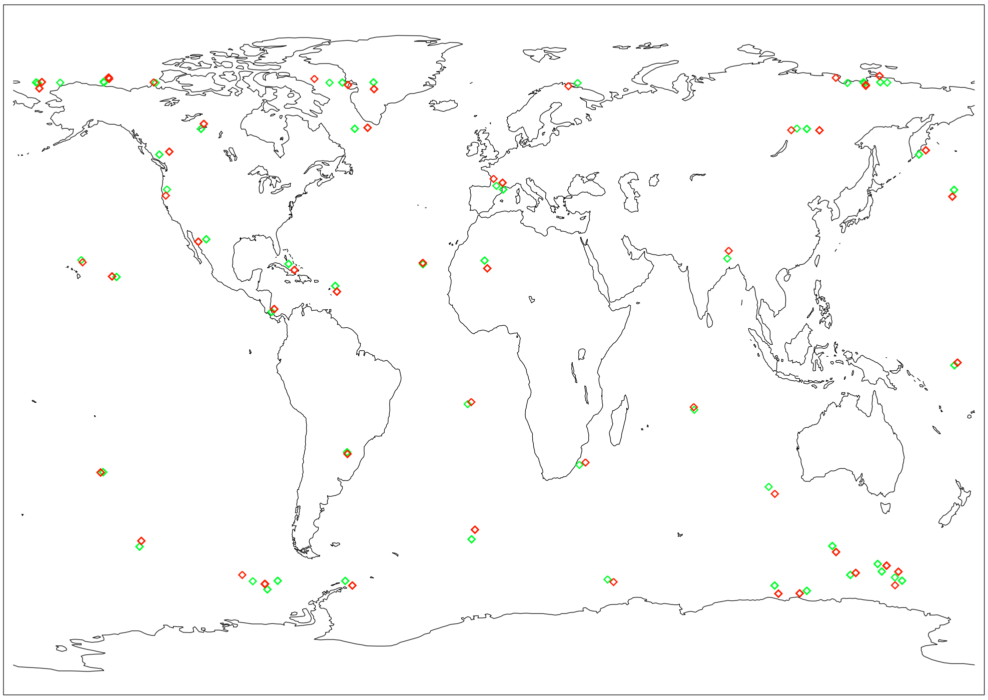

Figure 4.4. Coincidences for GOMOS and CHAMP measurements within an interval of 300 km and 3 hours. In this set 92 profiles were compared.

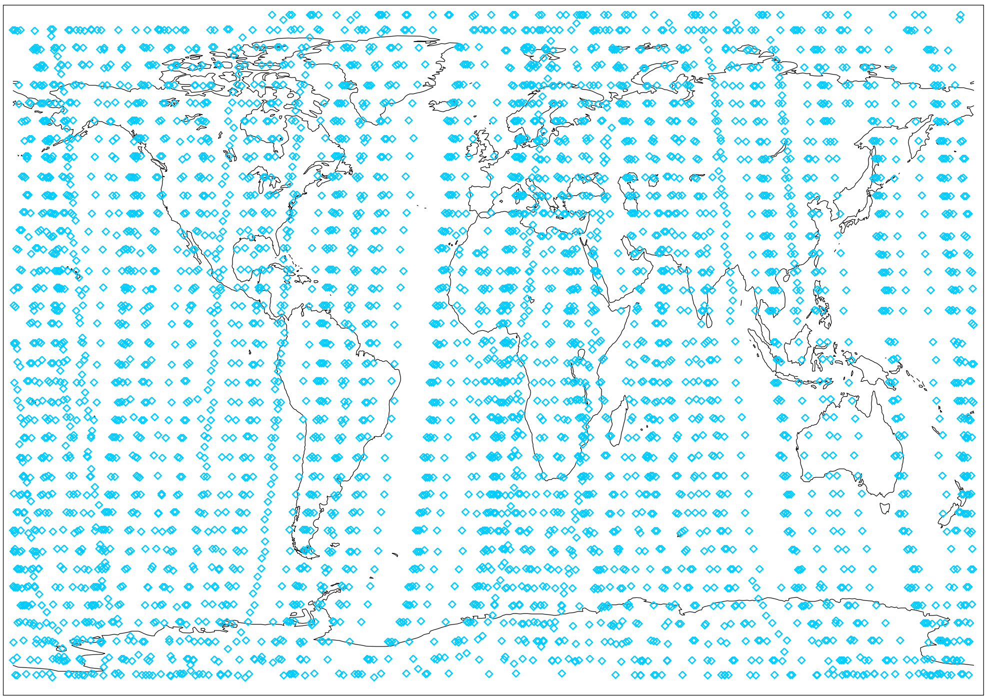

Figure 4.5. Locations where MIPAS measurements were performed. The graph displays 4222 occultation profiles available for days: September 20 - 26 and October 11 - 13, 2002.

profiles (Fig. 4.5) by selecting days, where GOMOS data was available in good quality (c.f. Section 4.2.1). After applying coincidences criteria (300 km distance and 3 hours between two occultation event) we could identify 198 profiles for our validation study. Details on the MIPAS retrieval scheme can be found in [26]. MIPAS measurements were taken between 6 and 70 km height with a vertical resolution of 3 km. The horizontal resolution lies between 300 and 500 km along track.

4.2.4 ECMWF Analysis

For the comparison of GOMOS SFA/SATU data we chose co-located vertically distributed temperatures and refractivity profiles from the nearest analysis time of 6-hourly ECMWF operational analysis data. The data fields were retrieved from ECMWF corresponding to the T511L60 spectral resolution with 60 height levels and spherical harmonics truncation 511 what gives a latitudinal/longitudinal resolution of 0.351°.

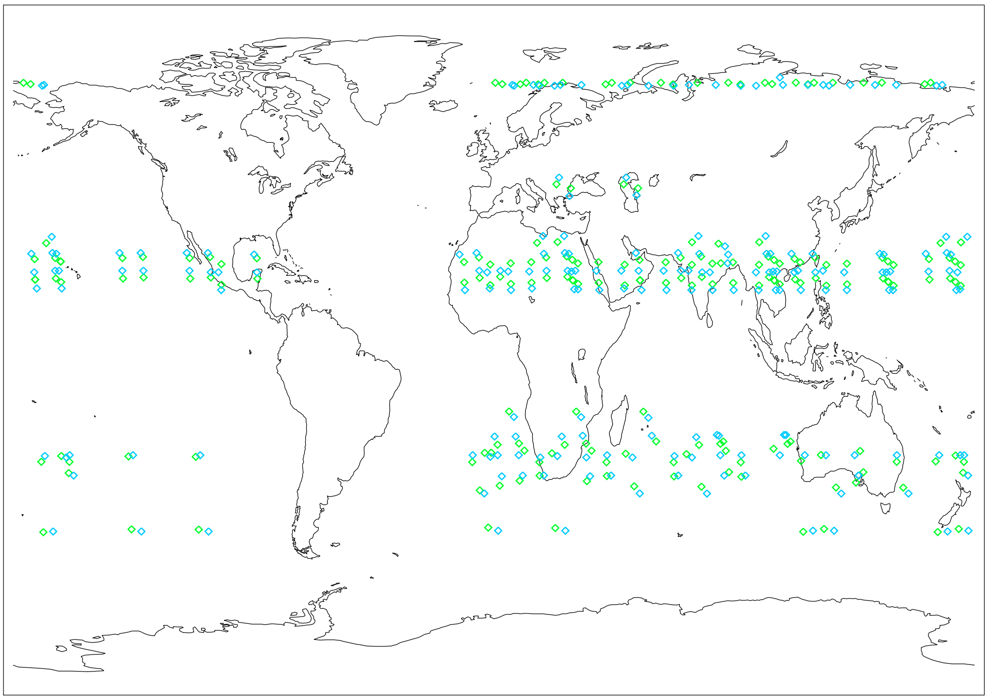

Figure 4.6. Coincidences for GOMOS and MIPAS measurements within an interval of 300 km and 3 hours. In this set 198 profiles were compared.

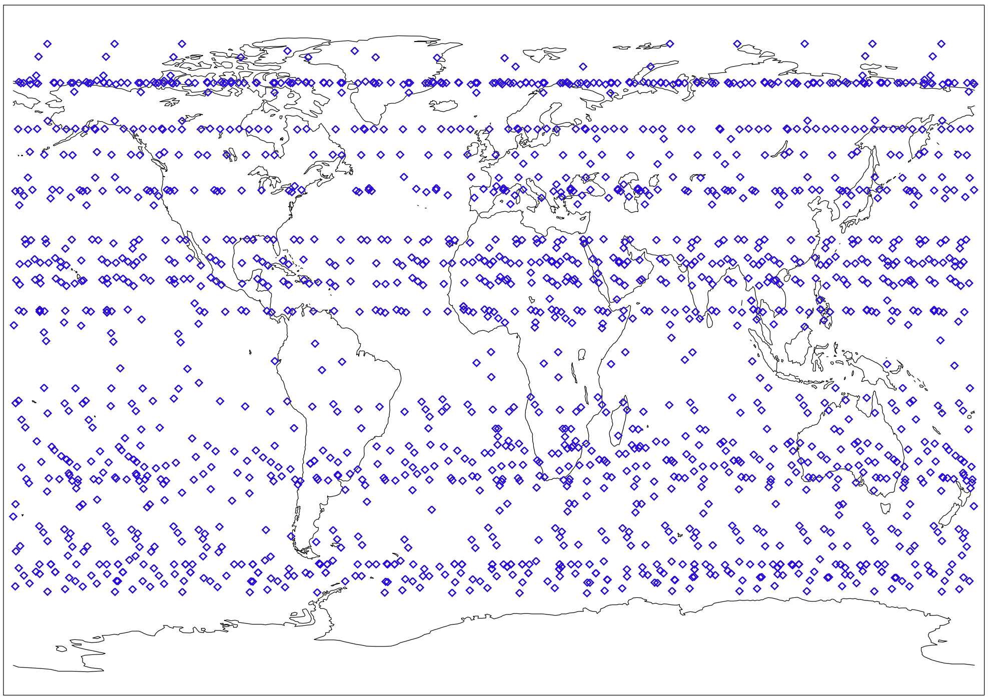

Figure 4.7. Locations where GOMOS data is validated with ECMWF analysis products.

5 Validation Results and Discussion

5.1 Ozone Retrieval & Validation

This Section summarizes the results of a feasibility study for an ozone retrieval algorithm. We show pure simulated data as well as results of an exploitation of GOMOS real transmission data.

5.1.1 Simulated Retrieval Data

Simulated data was used to show whether the algorithm meets the premises we defined. A carefully selected set of artificial data gives rise to possible leaks in the understanding of the chosen retrieval process. The shown graphs below clearly point out the capability of the algorithm to be used for operational data. Here we have selected a single event (Fig. 5.1) and present ozone profiles and their corresponding errors. Fig. 5.2 shows the bias $\hat{\mathbf{b}}$ profiles and the bias ± standard deviations $\hat{\mathbf{b}} \pm \hat{\mathbf{s}}$ of a set of 500 randomly initiated profiles calculated for the same occultation location.

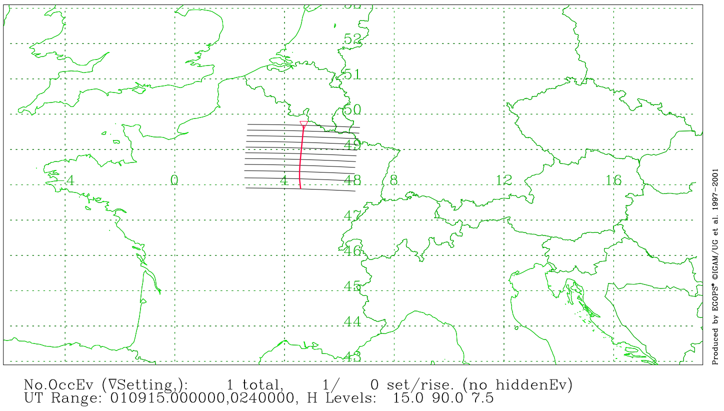

Figure 5.1. Test occultation event shown with 7.5 km spacing between rays from 15 km to 90 km along the tangent point trajectory in nadir view over north-eastern France and southern Belgium. The bundle of parallel lines illustrates the raypaths for ±150 km about the tangent point, roughly reflecting the horizontal resolution of the occultation data.

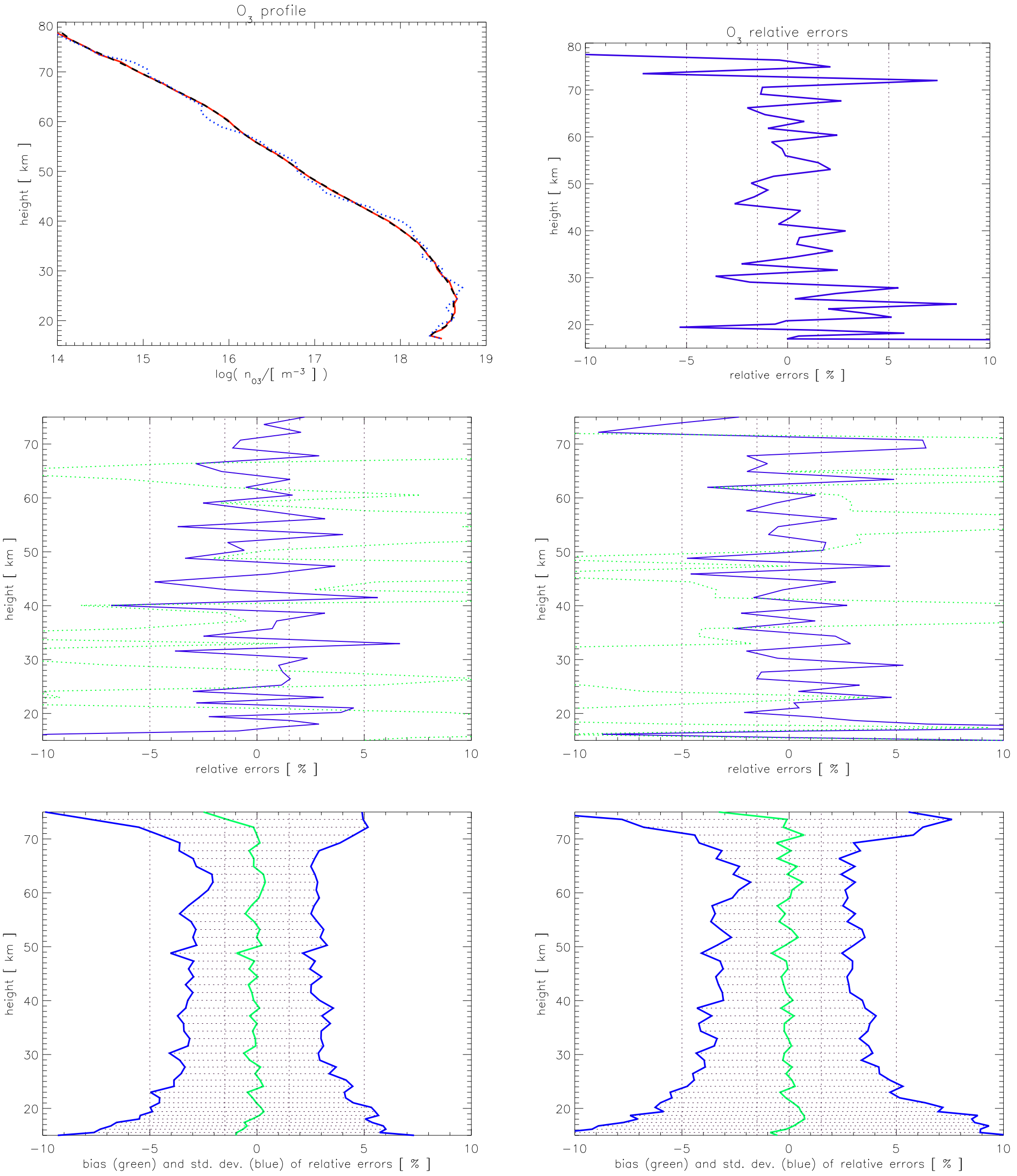

Figure 5.2. The top left panel shows a selected simulated GOMOS ozone profile, where the black dashed line is the "true" profile, the blue dotted line is the *a priori* profile, and the solid red line denotes the retrieved profile, respectively. The corresponding error profile (retrieved-minus-"true") is shown in the top right panel. The profiles were simulated at the occultation event location shown in Fig. 5.1. The mid two panels are simulated ozone profile errors, where the solid blue line indicates the error against a selected "true" profile, while the light green dotted line is the *a priori* profile deviation from the "true" reference profile. The bottom panels are randomly initiated simulated GOMOS ozone profile errors with 20% *a priori* error (left) and 30% *a priori* error (right). The light green line is the bias profile, while the dark blue lines show bias ± standard deviation $\hat{\mathbf{b}} \pm \hat{\mathbf{s}}$.

5.1.2 Ozone Profile Retrieval: Validation with GOMOS Level 2 Data

Ozone Profiles and Errors at Different Star Magnitudes

Calculations with our ozone retrieval are validated with GOMOS level 2 profiles. Each graph consists of a set of ten equally determined ozone profiles differing only in the randomly selected $x_i|_{i=0}$ (c.f. 3.5). Bias and standard deviation profiles are calculated as outlined in 3.4. The first set of ozone data validation shows error profiles with respect to operational GOMOS level 2 ozone data. The plots clearly show a star magnitude dependence for all latitude sections. For bright stars (magnitude -1.44, -0.73 and 0.45) standard deviations are found <5% from 35 km up to 60 km. In the upper stratospheric regime errors significantly rise due to a high signal (transmission $T \simeq 1$) throughout all wavelengths, which in turn makes it difficult to see clear ozone absorption structures. From the ozone layer (~25 km) downwards the star signal diminishes quickly what results in low signal to noise ratios and large fluctuations in the ozone profile.

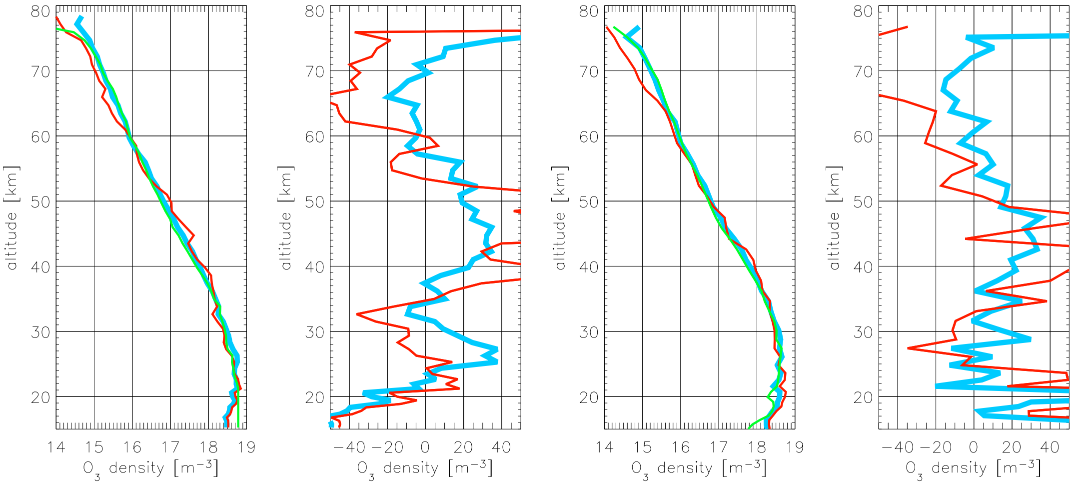

Figure 5.3. Two selected ozone and corresponding error profiles. The ozone densities are shown in a log plot, where the thick light blue line denotes the retrieved profile, the small green line is the reference GOMOS level 2 profile and the thin red line represents *a priori* data. The errors are given for validation with real GOMOS level 2 (thick light blue line) and for a comparison to an *a priori* profile (thin red line).

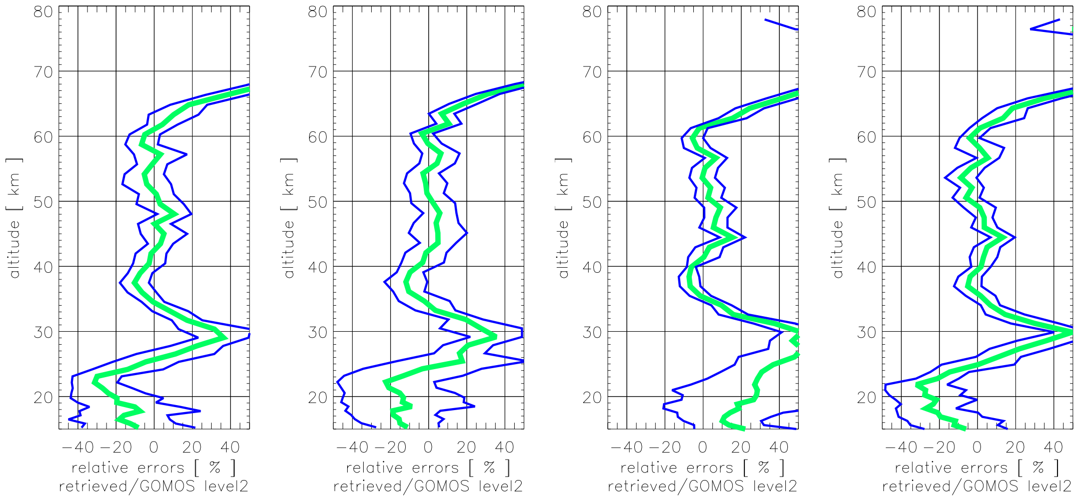

Figure 5.4. Low latitude ozone error profile (validated with GOMOS level 2 data) for **star magnitude** 0.45. The thick green line denotes the bias profile $\hat{\mathbf{b}}$, while the enveloping fine blue lines are the bias ± standard deviation profile $\hat{\mathbf{b}} \pm \hat{\mathbf{s}}$.

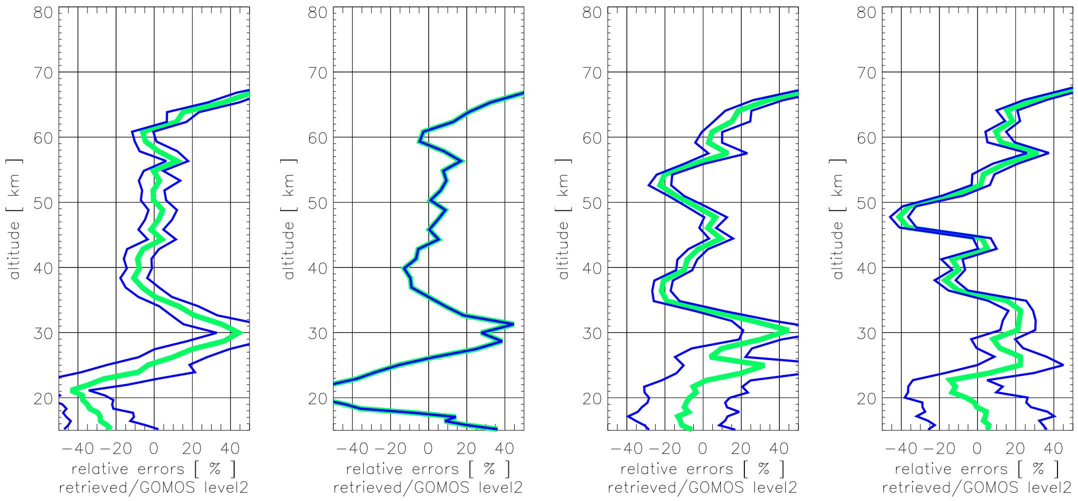

Figure 5.5. Low latitude ozone error profile (validated with GOMOS level 2 data) for **star magnitudes** -0.73 (left two) and 1.86 (right two). The thick green line denotes the bias profile $\hat{\mathbf{b}}$, while the enveloping fine blue lines are the bias ± standard deviation profile $\hat{\mathbf{b}} \pm \hat{\mathbf{s}}$.

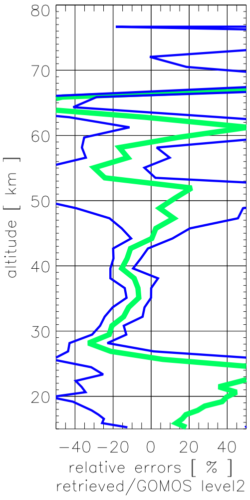

Figure 5.6. Low latitude ozone error profile (validated with GOMOS level 2 data) for **star magnitude** 2.85. The thick green line denotes the bias profile $\hat{\mathbf{b}}$, while the enveloping fine blue lines are the bias ± standard deviation profile $\hat{\mathbf{b}} \pm \hat{\mathbf{s}}$.

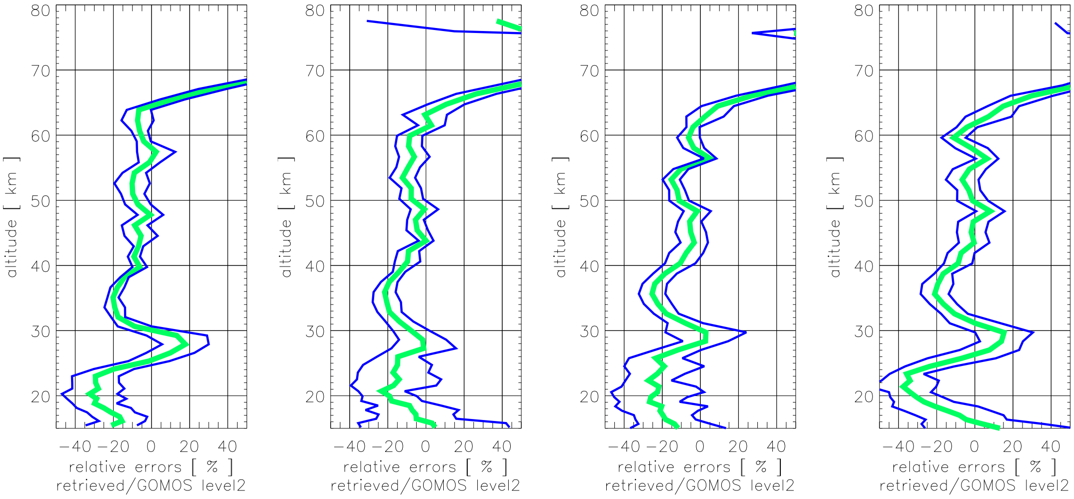

Figure 5.7. Mid latitude ozone error profile (validated with GOMOS level 2 data) for **star magnitude** 1.16. The thick green line denotes the bias profile $\hat{\mathbf{b}}$, while the enveloping fine blue lines are the bias ± standard deviation profile $\hat{\mathbf{b}} \pm \hat{\mathbf{s}}$.

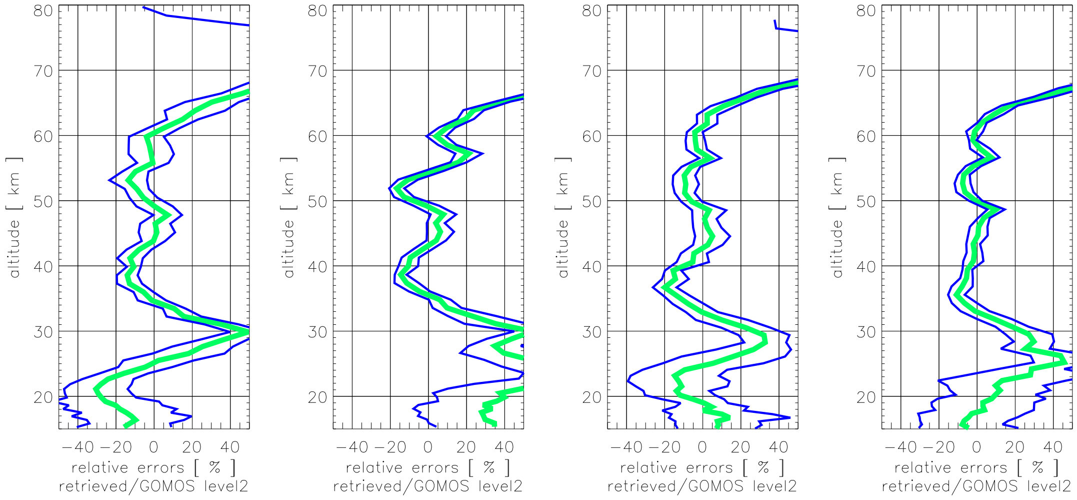

Figure 5.8. Mid latitude ozone error profile (validated with GOMOS level 2 data) for **star magnitude** 1.5. The thick green line denotes the bias profile $\hat{\mathbf{b}}$, while the enveloping fine blue lines are the bias ± standard deviation profile $\hat{\mathbf{b}} \pm \hat{\mathbf{s}}$.

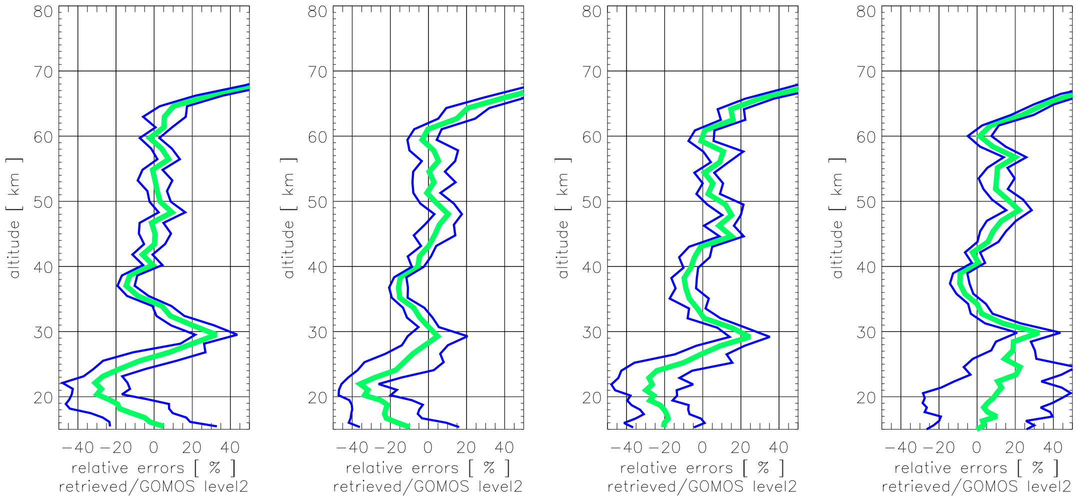

Figure 5.9. Mid latitude ozone error profile (validated with GOMOS level 2 data) for **star magnitude** 1.73. The thick green line denotes the bias profile $\hat{\mathbf{b}}$, while the enveloping fine blue lines are the bias ± standard deviation profile $\hat{\mathbf{b}} \pm \hat{\mathbf{s}}$.

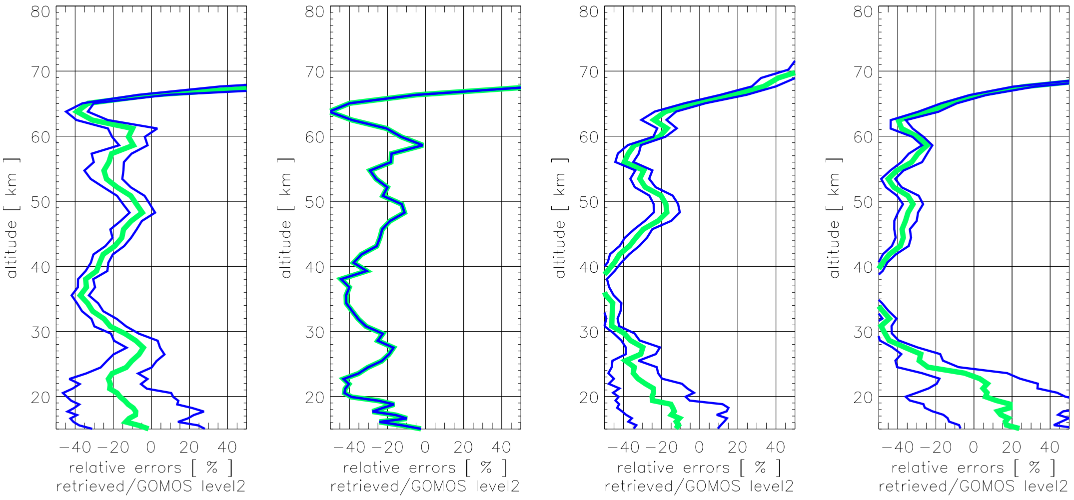

Figure 5.10. High latitude ozone error profile (validated with GOMOS level 2 data) for **star magnitude** 0.4. The thick green line denotes the bias profile $\hat{\mathbf{b}}$, while the enveloping fine blue lines are the bias ± standard deviation profile $\hat{\mathbf{b}} \pm \hat{\mathbf{s}}$.

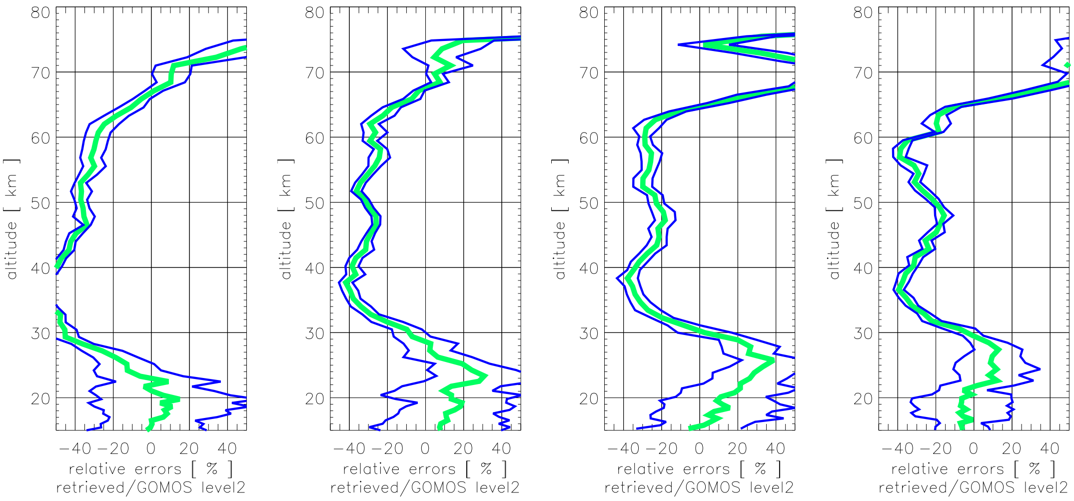

Figure 5.11. High latitude ozone error profile (validated with GOMOS level 2 data) for **star magnitude** 0.4. The thick green line denotes the bias profile $\hat{\mathbf{b}}$, while the enveloping fine blue lines are the bias ± standard deviation profile $\hat{\mathbf{b}} \pm \hat{\mathbf{s}}$.

Validation with Globally Distributed Profiles

Here we present the statistics of a selection of globally distributed occultation events separated by date and latitude (low, mid, high) regimes. The sets include occultations of stars between magnitudes -1.44 and 2. Stars with magnitudes greater than 2 show significantly larger errors. As in the single profiles statistics we see good retrieval performance in low and mid latitude regions, where biases are found ~5% from 25 - 65 km. Below 25 km we find changing biases of up to ~20%. This reflects the fact that data measured at such altitudes have small transmission values and large fluctuations, which affects the retrieval quality. In high latitudes resulting ozone profiles sometimes deviate even more than 20% due to an only small set of available stars.

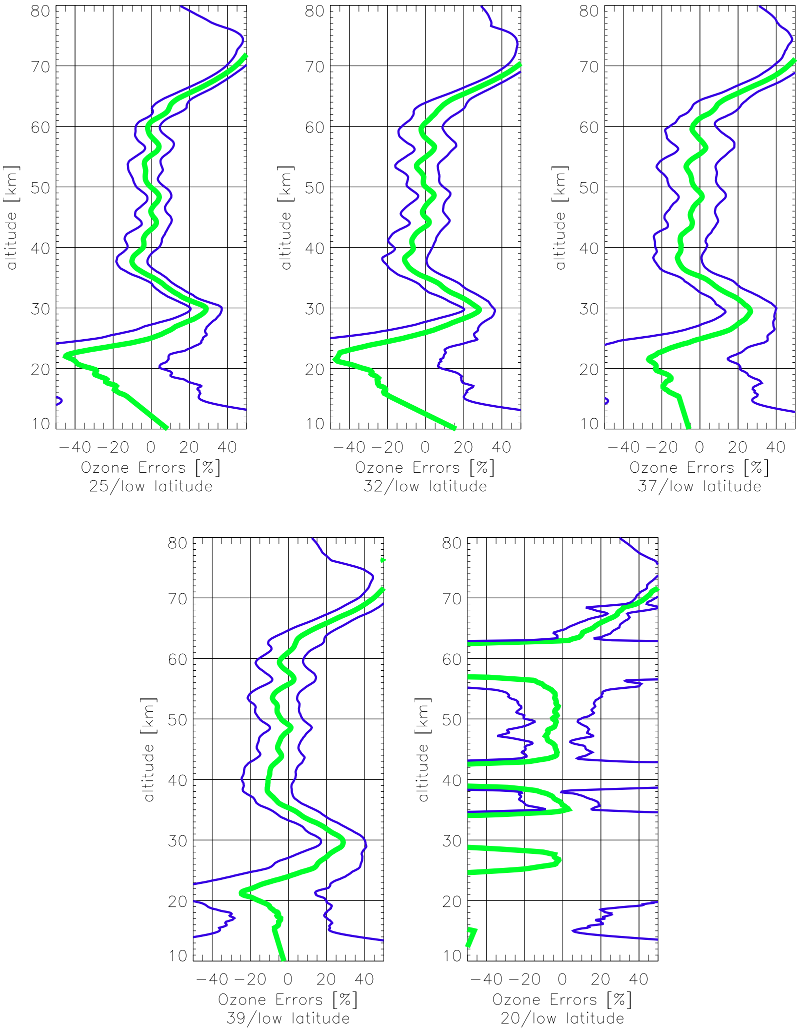

25/low latitude

32/low latitude

37/low latitude

39/low latitude

20/low latitude

Figure 5.12. Low latitudinal global ozone statistics for more day ensembles: 2002-09-20/21, 2002-09-22/23 and 2002-09-24/25 (top) and 2002-09-26/27, 2002-10-11/12/13 (bottom). The thick green line denotes the bias profile $\hat{\mathbf{b}}$, while the enveloping fine blue lines are the bias ± standard deviation profile $\hat{\mathbf{b}} \pm \hat{\mathbf{s}}$.

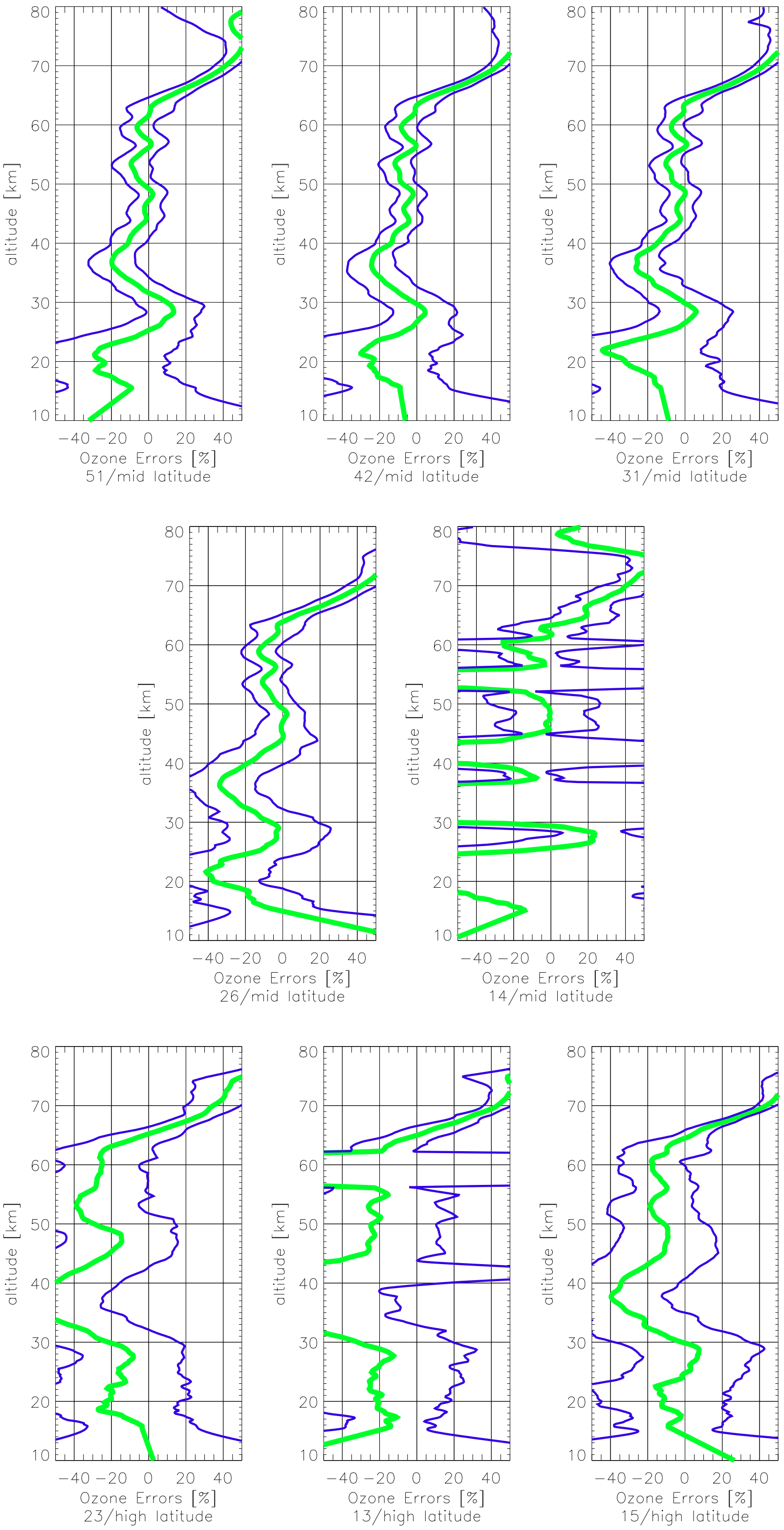

Figure 5.13. Mid latitudinal global ozone statistics for more day ensembles: 2002-09-20/21, 2002-09-22/23 and 2002-09-24/25 (top), 2002-09-26/27, 2002-10-11/12/13 (middle) and high latitudinal global ozone statistics for more day ensembles: 2002-09-20/21, 2002-09-22/23 and 2002-09-24/25 (bottom). The thick green line denotes the bias profile $\hat{\mathbf{b}}$, while the enveloping fine blue lines are the bias ± standard deviation profile $\hat{\mathbf{b}} \pm \hat{\mathbf{s}}$.

5.1.3 Ozone Profile Retrieval: Validation with ECMWF Analysis Data

Ozone Profiles and Errors at Different Star Magnitudes

Validation with ECMWF profiles is done with the same data set as discussed in the previous Section. A direct comparison of GOMOS level 2 and ECMWF data is not given here, but can be estimated qualitatively. GOMOS level 2 profiles are here replaced by corresponding ECMWF analysis profiles. While GOMOS profiles optimally reach heights of more than 150 km, in this validation set we can only use data up to ~ 60 km which is the maximum height range available for ECMWF data. For comparison reasons the profiles are given from 15 km to 80 km.

A clear bias of up to 30% was found in the validation profiles for low and mid latitudes. Standard deviations are $\sim$ 5% for bright stars an increase for dim stars, which is an effect already seen in 5.1.2. At high latitudes a bias is still existent but some profiles perform much better with biases smaller than 10%. In the following graphs the thick green line denotes the bias profile $\hat{\mathbf{b}}$, while the enveloping fine blue lines are the bias ± standard deviation profile $\hat{\mathbf{b}} \pm \hat{\mathbf{s}}$.

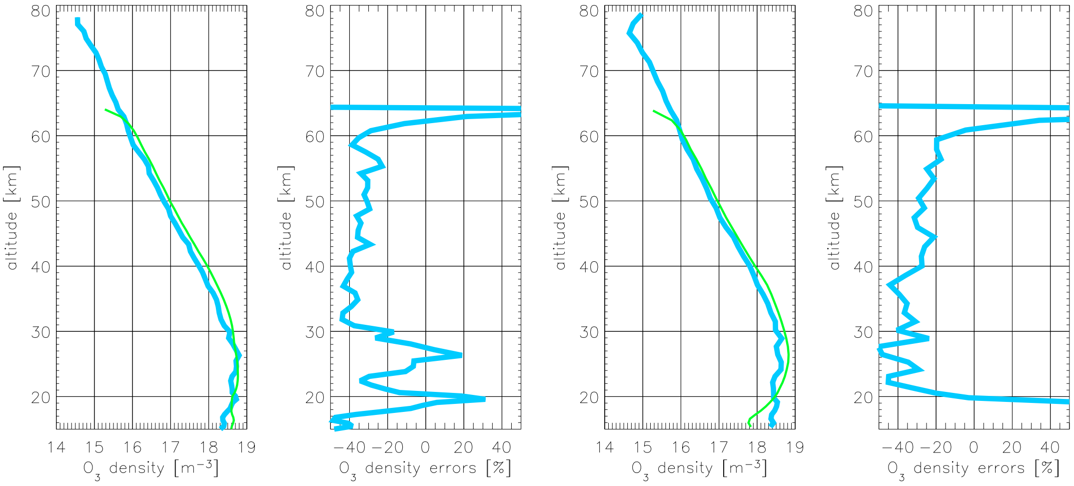

Figure 5.14. Two selected ozone and corresponding error profiles. The ozone densities are shown in a log plot, where the thick light blue line denotes the retrieved profile and the small green line is the reference ECMWF analysis profile. The errors for the validation with ECMWF analysis profiles are given with a thick light blue line.

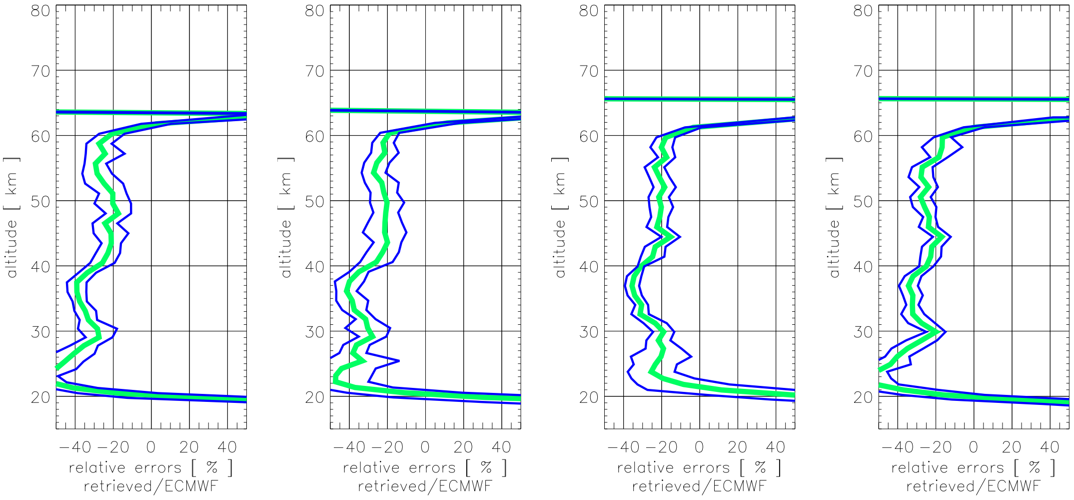

Figure 5.15. Low latitude ozone error profile (validated with ECMWF analysis data) for **star magnitude** 0.45. The thick green line denotes the bias profile $\hat{\mathbf{b}}$, while the enveloping fine blue lines are the bias ± standard deviation profile $\hat{\mathbf{b}} \pm \hat{\mathbf{s}}$.

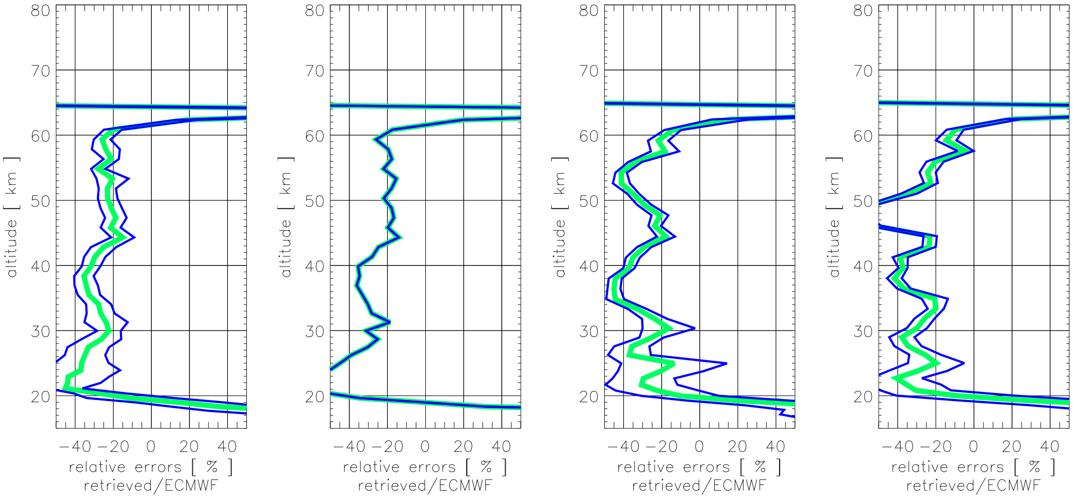

Figure 5.16. Low latitude ozone error profile (validated with ECMWF analysis data) for **star magnitudes** -0.73 (left two) and 1.86 (right two). The thick green line denotes the bias profile $\hat{\mathbf{b}}$, while the enveloping fine blue lines are the bias ± standard deviation profile $\hat{\mathbf{b}} \pm \hat{\mathbf{s}}$.

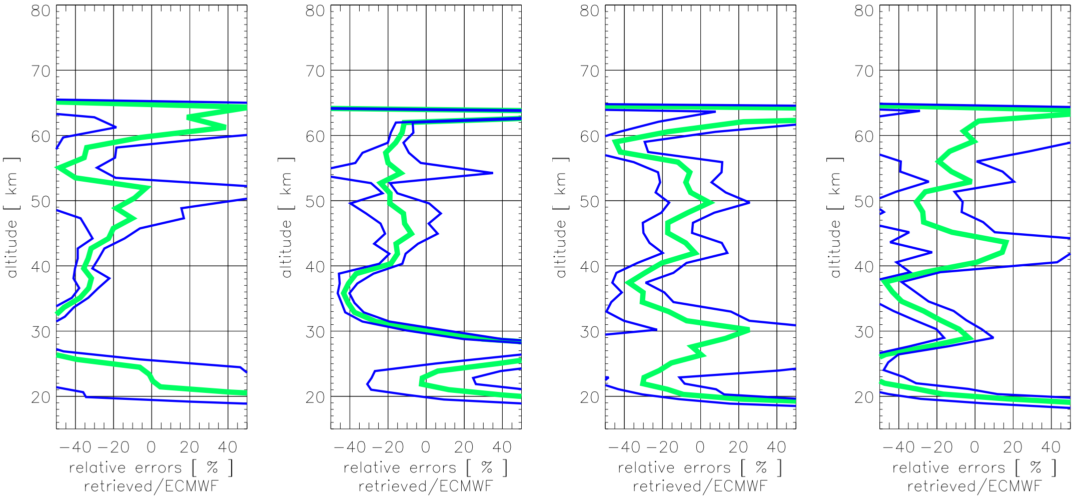

Figure 5.17. Low latitude ozone error profile (validated with ECMWF analysis data) for **star magnitude** 2.85. The thick green line denotes the bias profile $\hat{\mathbf{b}}$, while the enveloping fine blue lines are the bias ± standard deviation profile $\hat{\mathbf{b}} \pm \hat{\mathbf{s}}$.

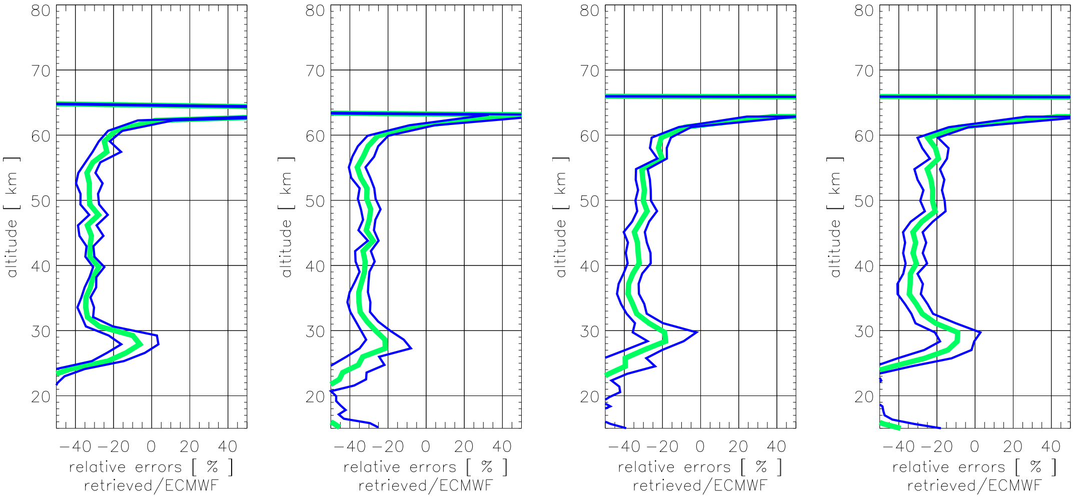

Figure 5.18. Mid latitude ozone error profile (validated with ECMWF analysis data) for **star magnitude** 1.16. The thick green line denotes the bias profile $\hat{\mathbf{b}}$, while the enveloping fine blue lines are the bias ± standard deviation profile $\hat{\mathbf{b}} \pm \hat{\mathbf{s}}$.

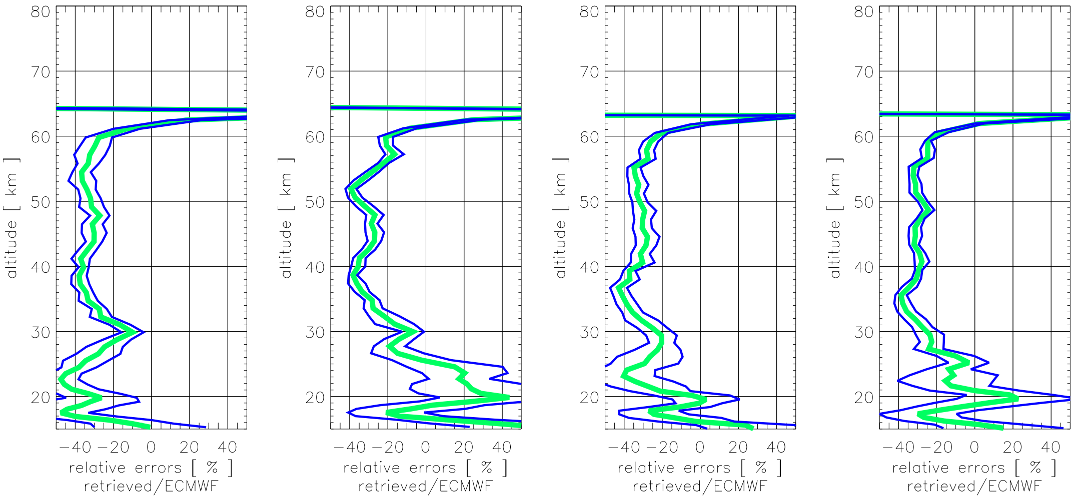

Figure 5.19. Mid latitude ozone error profile (validated with ECMWF analysis data) for **star magnitude** 1.5. The thick green line denotes the bias profile $\hat{\mathbf{b}}$, while the enveloping fine blue lines are the bias ± standard deviation profile $\hat{\mathbf{b}} \pm \hat{\mathbf{s}}$.

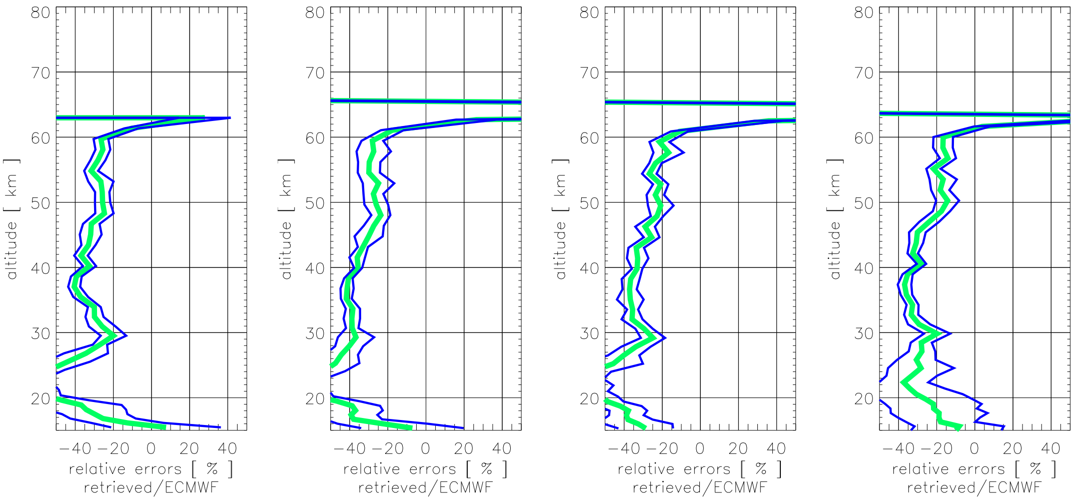

Figure 5.20. Mid latitude ozone error profile (validated with ECMWF analysis data) for **star magnitude** 1.73. The thick green line denotes the bias profile $\hat{\mathbf{b}}$, while the enveloping fine blue lines are the bias ± standard deviation profile $\hat{\mathbf{b}} \pm \hat{\mathbf{s}}$.

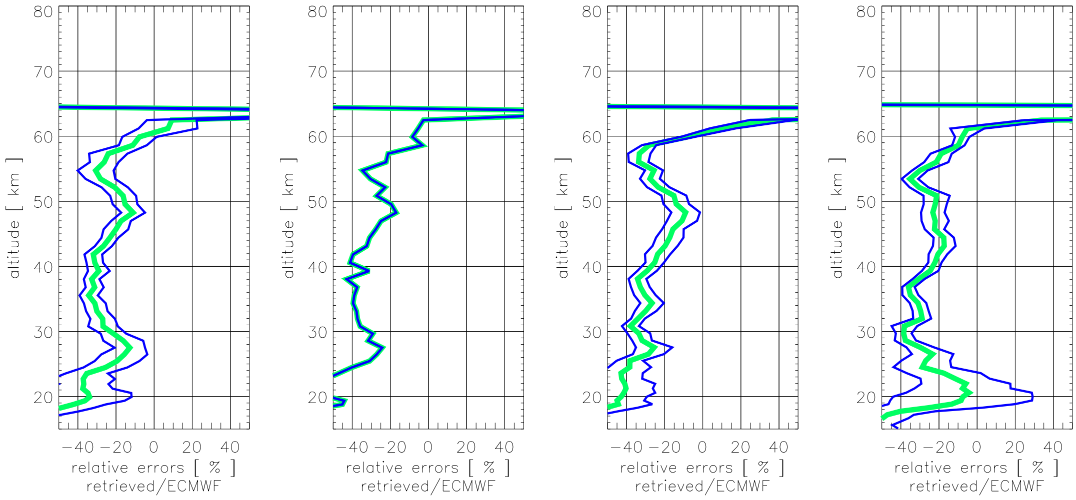

Figure 5.21. High latitude ozone error profile (validated with ECMWF analysis data) for **star magnitude** 0.4. The thick green line denotes the bias profile $\hat{\mathbf{b}}$, while the enveloping fine blue lines are the bias ± standard deviation profile $\hat{\mathbf{b}} \pm \hat{\mathbf{s}}$.

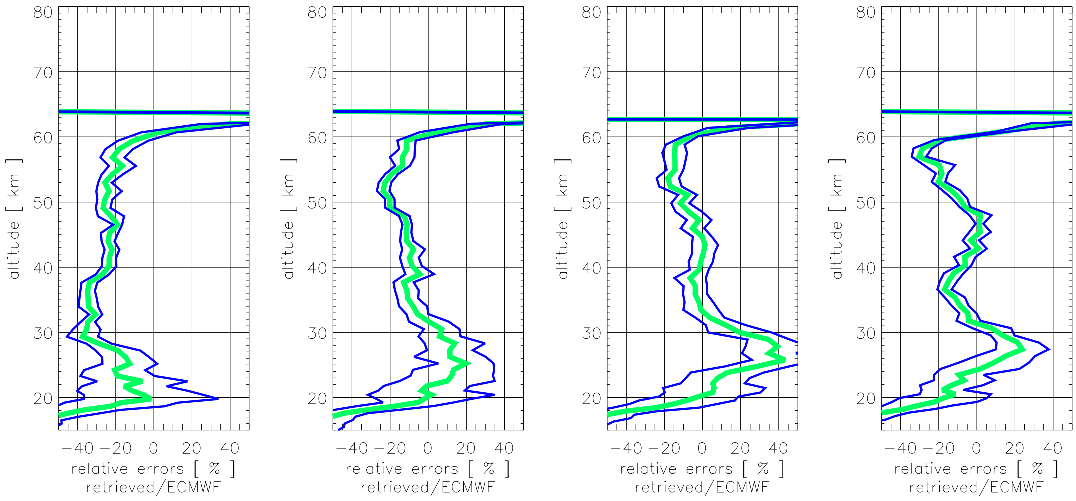

Figure 5.22. High latitude ozone error profile (validated with ECMWF analysis data) for **star magnitude** 0.4. The thick green line denotes the bias profile $\hat{\mathbf{b}}$, while the enveloping fine blue lines are the bias ± standard deviation profile $\hat{\mathbf{b}} \pm \hat{\mathbf{s}}$.

Validation with Globally Distributed Profiles

Here we present the statistics of a selection of globally distributed occultation events separated by date and latitude (low, mid, high) regimes. The sets include occultations of stars between magnitudes -1.44 and 2. Stars with magnitudes greater than 2 show significantly larger errors. As in the single profiles statistics we find biases with ~25% from 25 - 65 km for all latitude regions. Below 25 km we biases decrease from ~25%.

In the following graphs the thick green line denotes the bias profile $\hat{\mathbf{b}}$, while the enveloping fine blue lines are the bias ± standard deviation profile $\hat{\mathbf{b}} \pm \hat{\mathbf{s}}$.

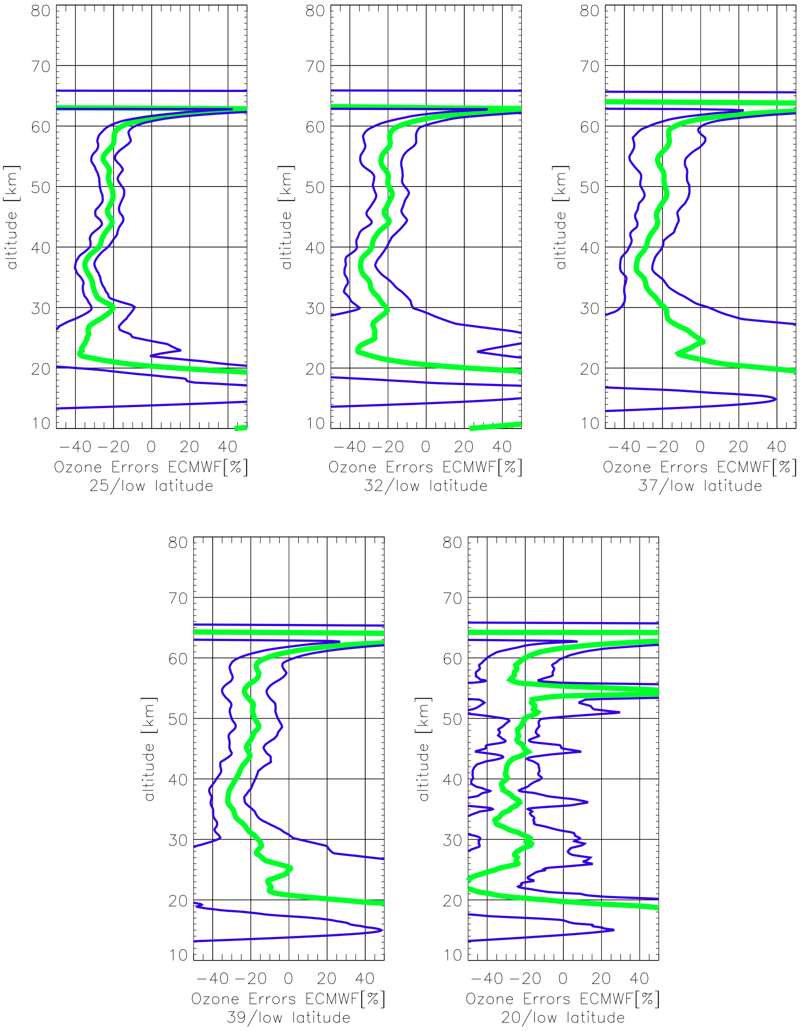

Figure 5.23. Low latitudinal global ozone statistics for more day ensembles: 2002-09-20/21, 2002-09-22/23 and 2002-09-24/25 (top) and 2002-09-26/27, 2002-10-11/12/13 (bottom). The thick green line denotes the bias profile $\hat{\mathbf{b}}$, while the enveloping fine blue lines are the bias ± standard deviation profile $\hat{\mathbf{b}} \pm \hat{\mathbf{s}}$.

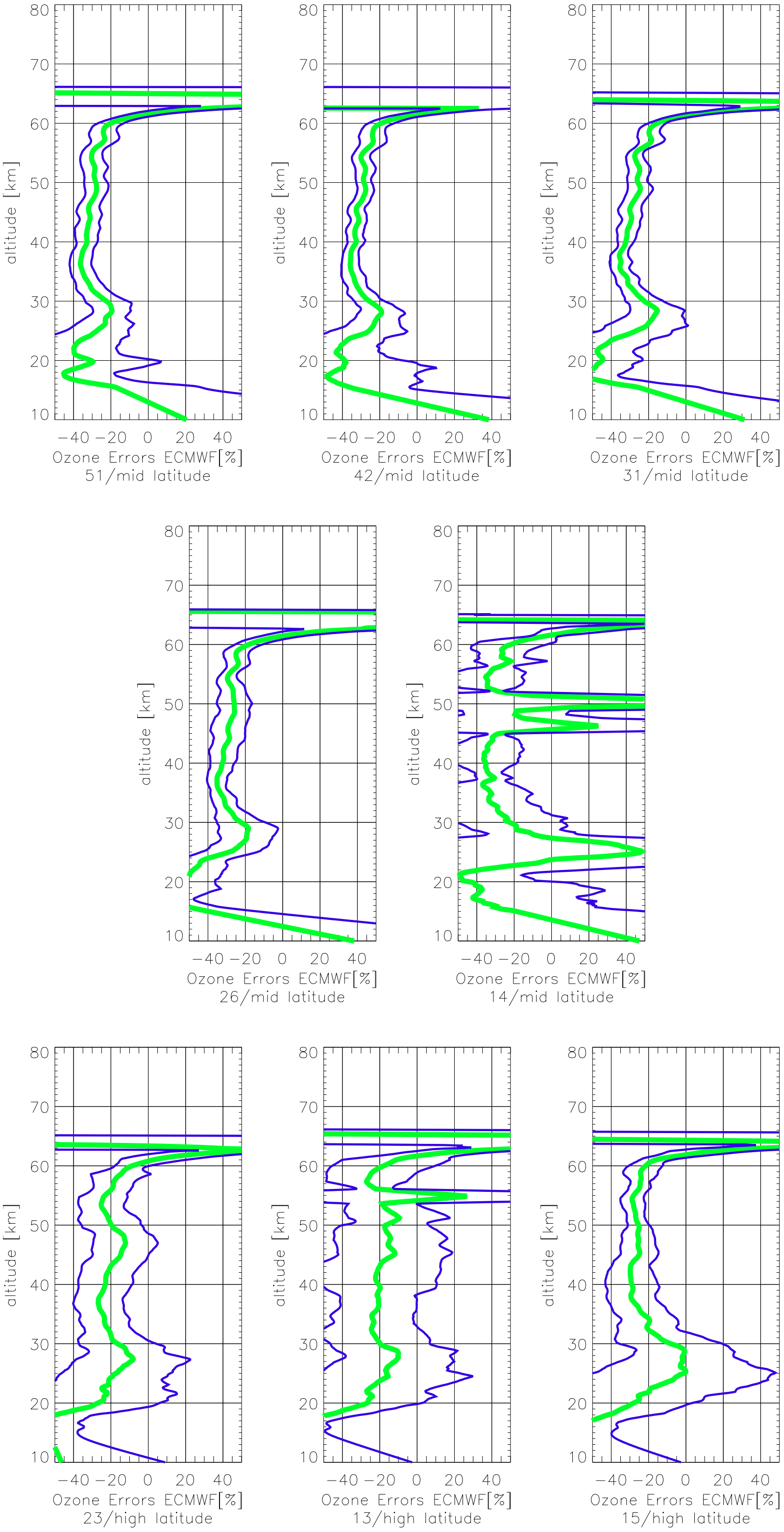

Figure 5.24. Mid latitudinal global ozone statistics for more day ensembles: 2002-09-20/21, 2002-09-22/23 and 2002-09-24/25 (top), 2002-09-26/27, 2002-10-11/12/13 (middle) and high latitudinal global ozone statistics for more day ensembles: 2002-09-20/21, 2002-09-22/23 and 2002-09-24/25 (bottom). The thick green line denotes the bias profile $\hat{\mathbf{b}}$, while the enveloping fine blue lines are the bias ± standard deviation profile $\hat{\mathbf{b}} \pm \hat{\mathbf{s}}$.

5.2 Temperature Retrieval & Validation

In this Section we discuss the results of our real GOMOS SFA/SATU data temperature retrieval (c.f. [27]). Statistical optimization was used to optimize bending angles, what has a significant impact on the resulting temperatures. GOMOS SFA/SATU temperatures are then compared to CHAMP level 2, ECMWF T511L60 analysis and MIPAS level 2 data. For this analysis the *GeoForschungsZentrum* (GFZ) in Potsdam provided CHAMP data and the *Institut für Meteorologie und Klimaforschung* (IMK) in Karlsruhe provided preprocessed MIPAS data. Both data packages are furthermore validated with ECMWF data published in [18].

5.2.1 Simulated Retrieval Data

Simulated bending angle and temperature profiles are produced with the EGOPS [23] software. We present two realizations of profiles, which differ in the randomly selected initialization vector.

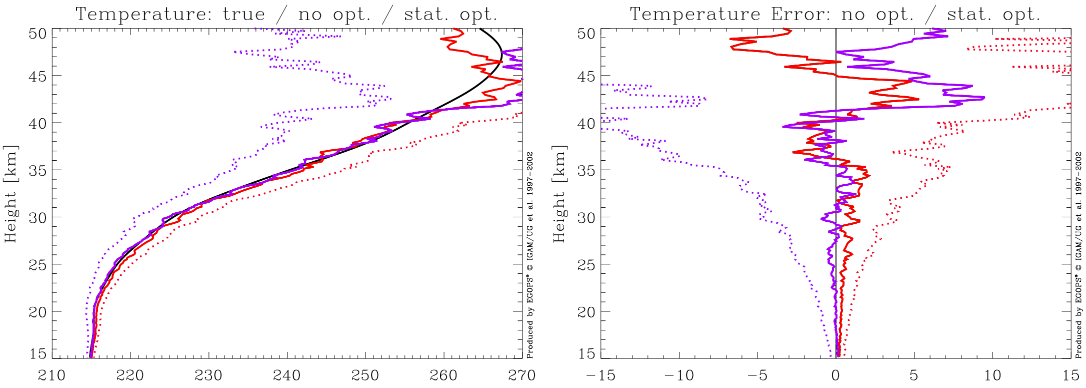

Figure 5.25. Two realizations of temperature profiles with (solid grey lines) and without (dashed grey lines) statistical optimization applied, where the smooth solid black line is the "true" profile (left). Corresponding errors (difference retrieved minus "true") of the two error realizations of temperature profiles with and without statistical optimization applied (right).

5.2.2 GOMOS SFA/SATU Profile Retrieval

Bending Angles and Temperatures at Different Star Magnitudes

The results of a GOMOS data retrieval depend on the selected star and its magnitude. In general one finds for bending angles and temperatures that a low star magnitude, favorably below 0, allows for retrievals into the troposphere down to heights of ∼5 km which is the theoretical minimum of GOMOS. In our selected data set transmission from only 50 stars are considered. Especially in the high attitude region there is a clear need of more occultation data.

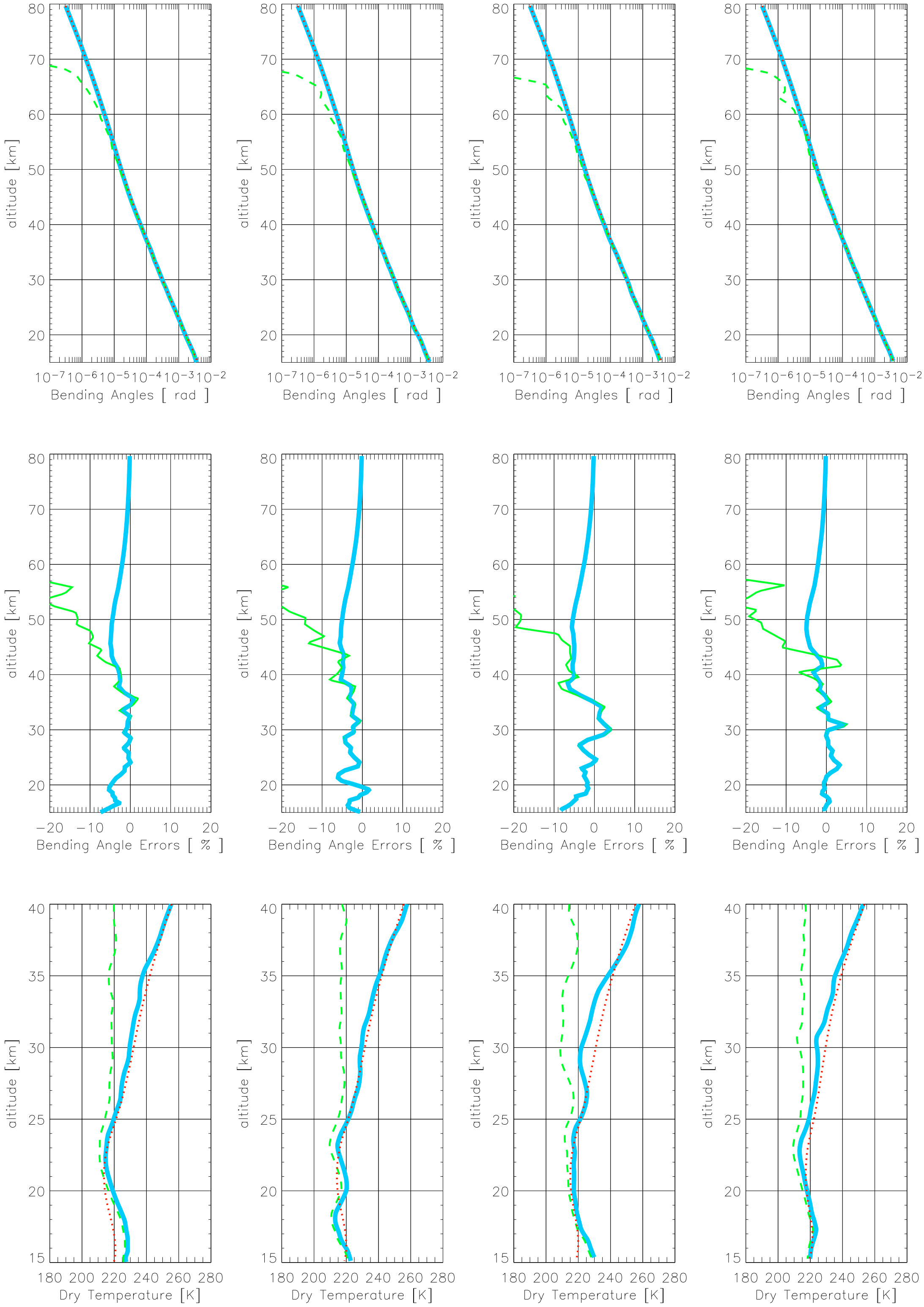

Figure 5.26. Absolute bending angle profiles (top), relative bending angle errors (middle) and corresponding temperatures (bottom) for four different occultation events with **star magnitude -1.44**. Thick light blue lines denote statistically optimized profiles. Thin red dotted lines are *a priori* profiles, while thin green solid and dashed lines are measured profiles without statistical optimization.

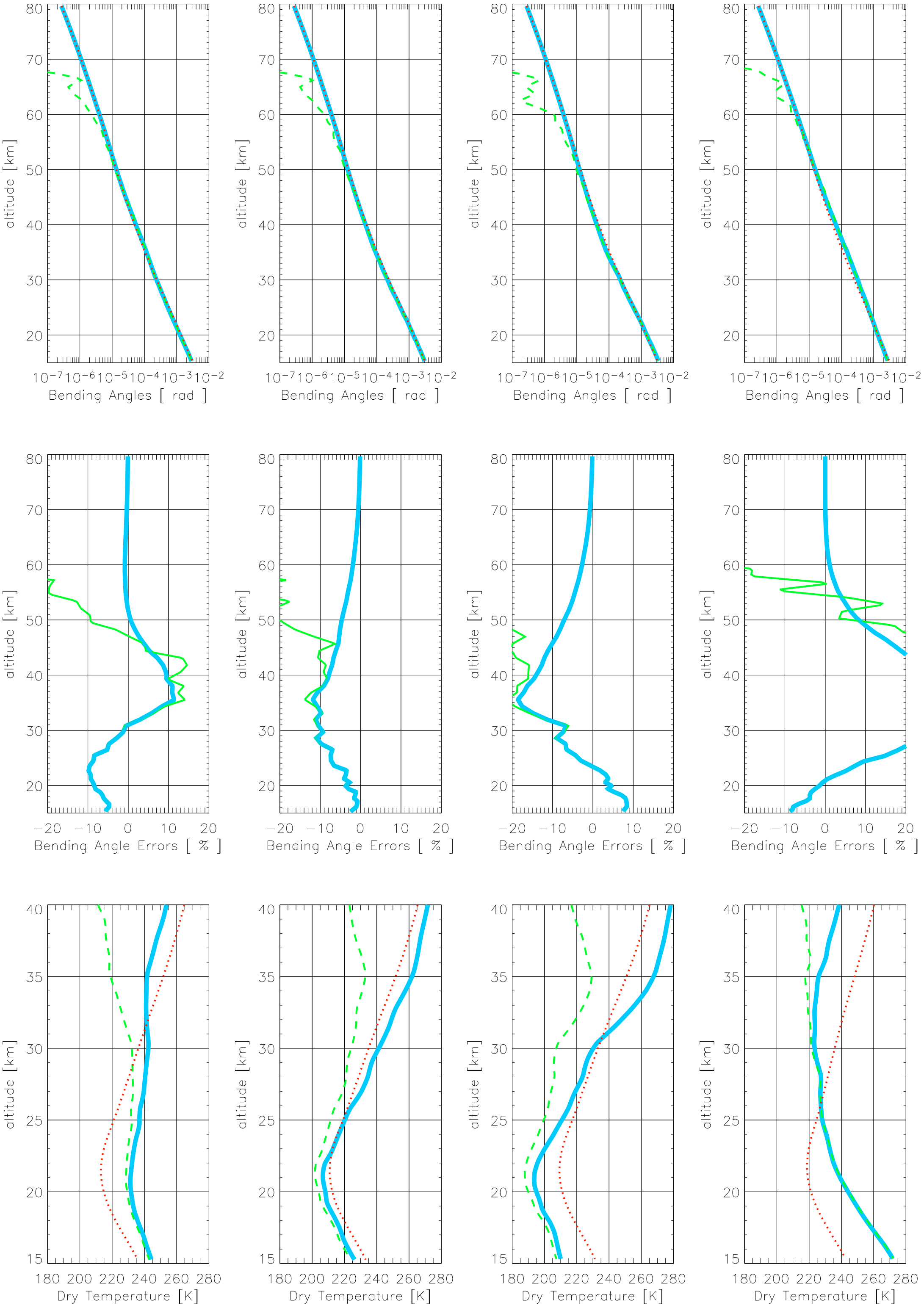

Figure 5.27. Absolute bending angle profiles (top), relative bending angle errors (middle) and corresponding temperatures (bottom) for four different occultation events with **star magnitude 0.40**. Thick light blue lines denote statistically optimized profiles. Thin red dotted lines are *a priori* profiles, while thin green solid and dashed lines are measured profiles without statistical optimization.

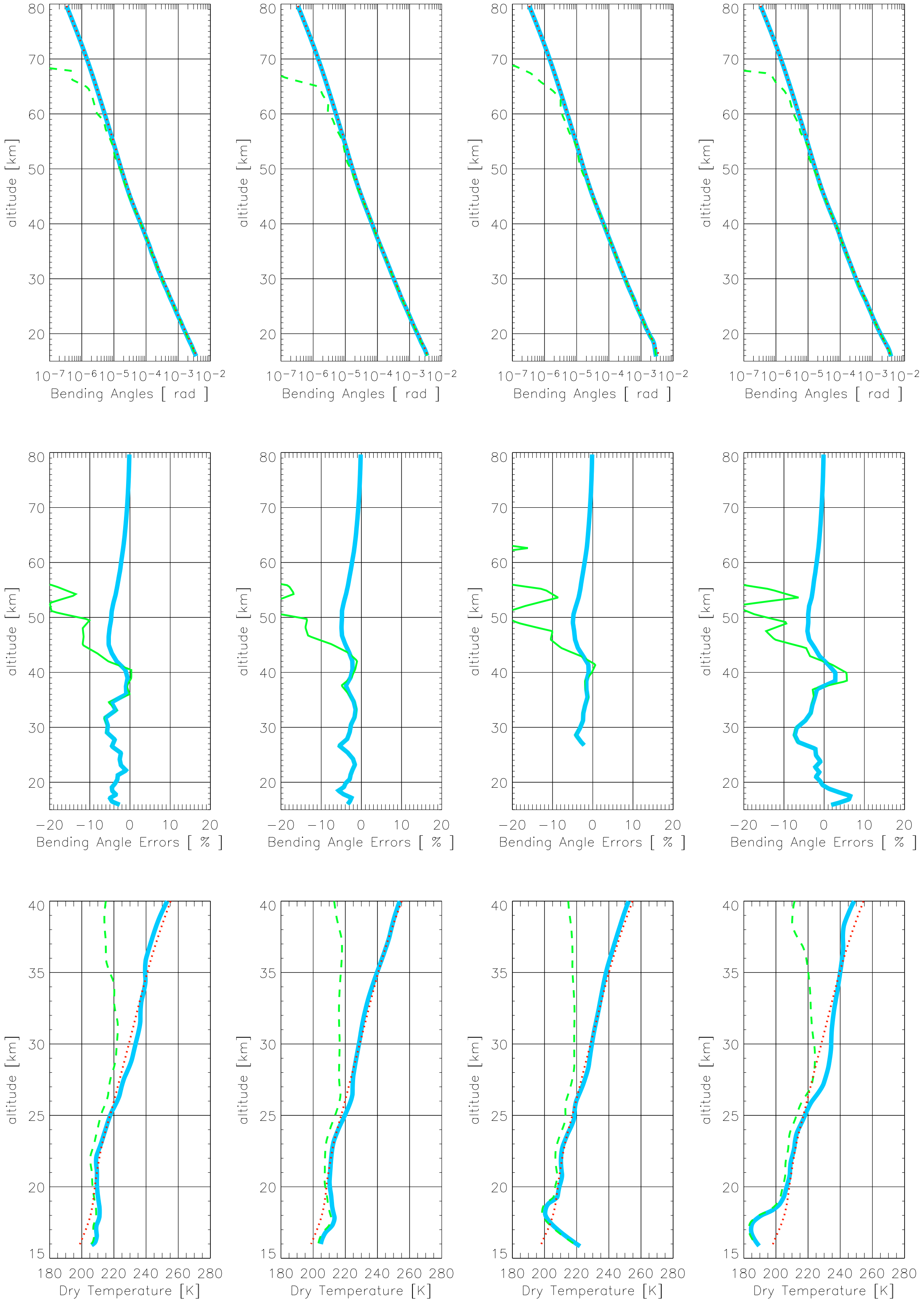

Figure 5.28. Absolute bending angle profiles (top), relative bending angle errors (middle) and corresponding temperatures (bottom) for four different occultation events with **star magnitude 0.45**. Thick light blue lines denote statistically optimized profiles. Thin red dotted lines are *a priori* profiles, while thin green solid and dashed lines are measured profiles without statistical optimization.

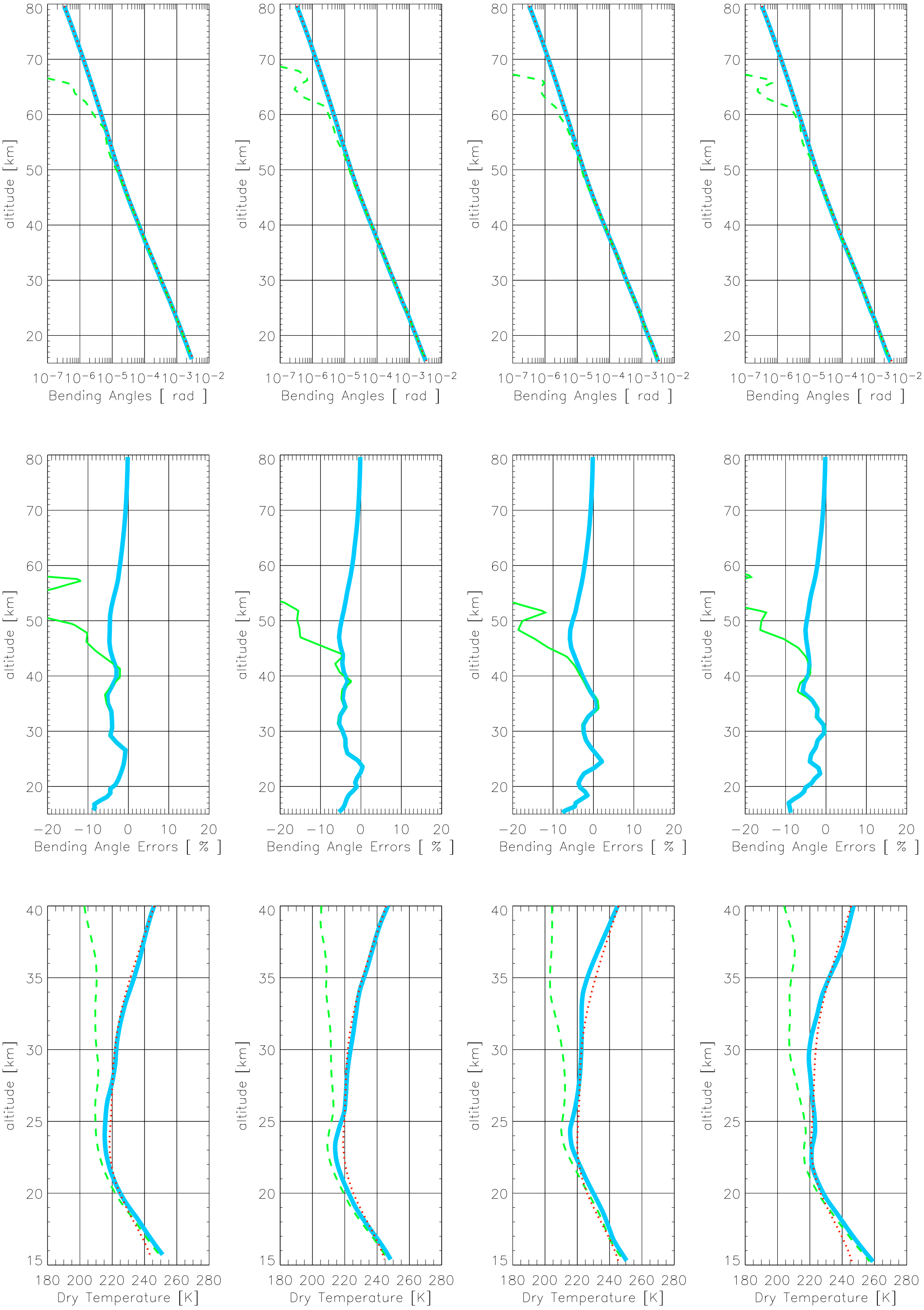

Figure 5.29. Absolute bending angle profiles (top), relative bending angle errors (middle) and corresponding temperatures (bottom) for four different occultation events with **star magnitude 1.16**. Thick light blue lines denote statistically optimized profiles. Thin red dotted lines are *a priori* profiles, while thin green solid and dashed lines are measured profiles without statistical optimization.

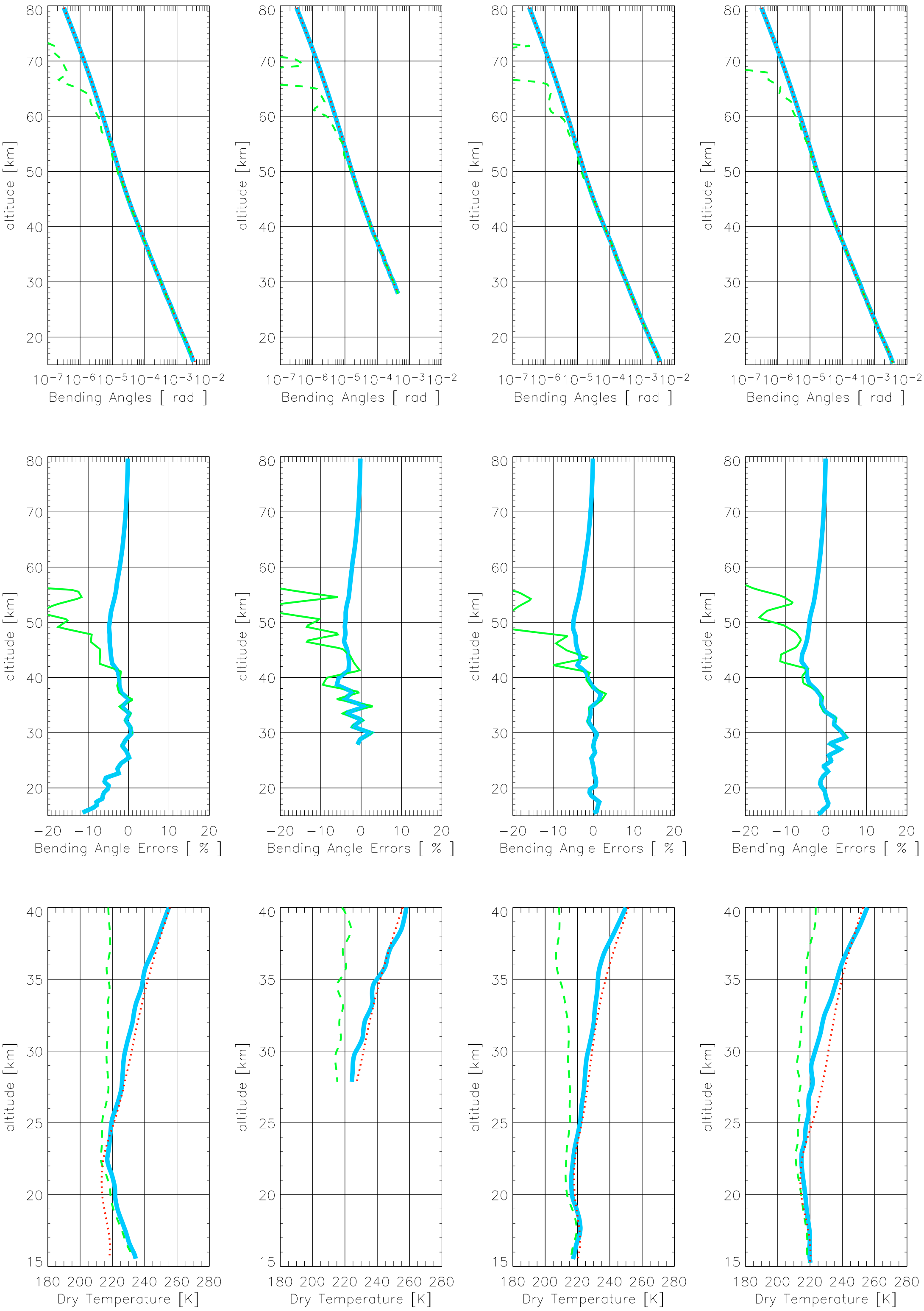

Figure 5.30. Absolute bending angle profiles (top), relative bending angle errors (middle) and corresponding temperatures (bottom) for four different occultation events with **star magnitude 1.50**. Thick light blue lines denote statistically optimized profiles. Thin red dotted lines are *a priori* profiles, while thin green solid and dashed lines are measured profiles without statistical optimization.

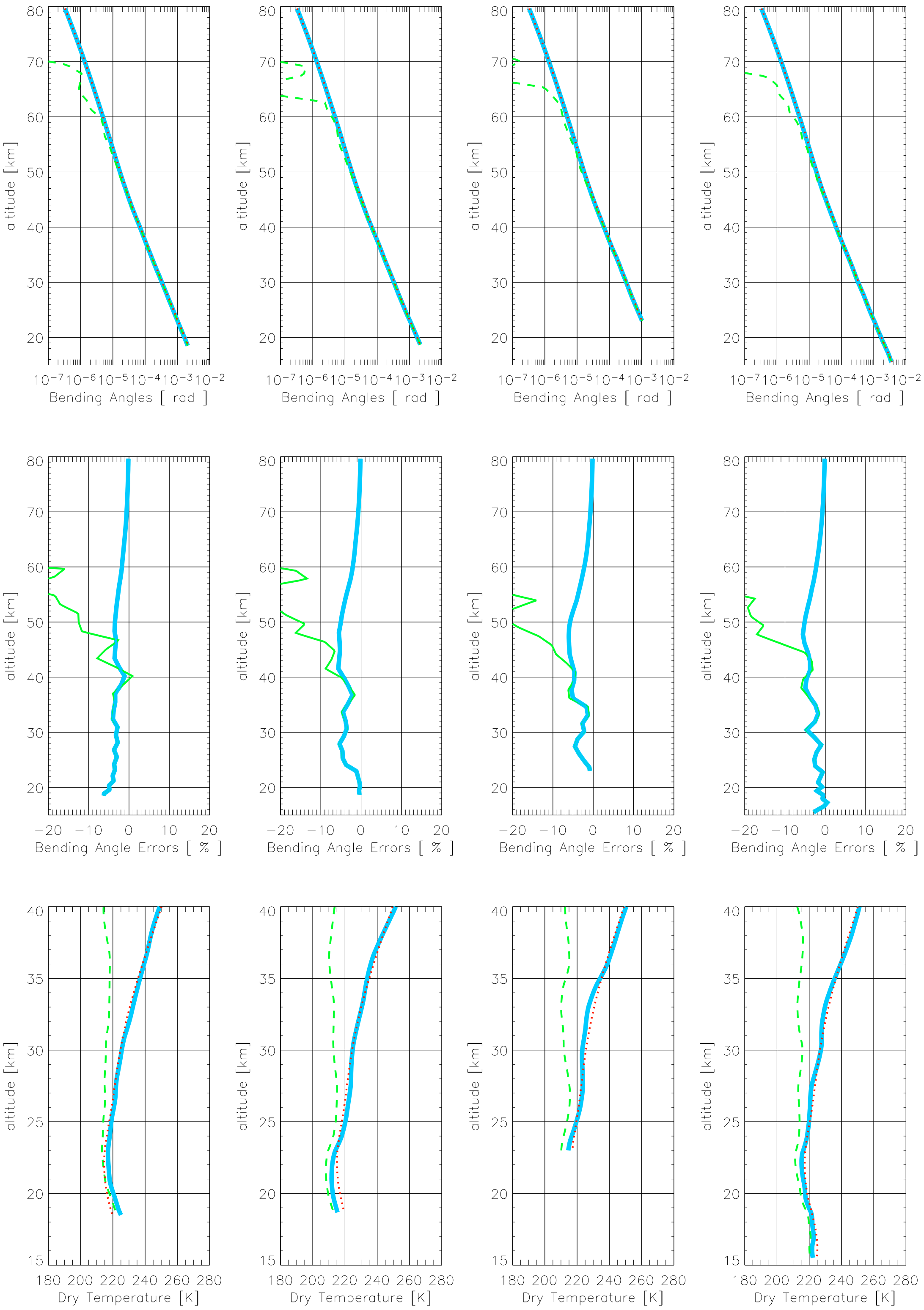

Figure 5.31. Absolute bending angle profiles (top), relative bending angle errors (middle) and corresponding temperatures (bottom) for four different occultation events with **star magnitude 1.73**. Thick light blue lines denote statistically optimized profiles. Thin red dotted lines are *a priori* profiles, while thin green solid and dashed lines are measured profiles without statistical optimization.

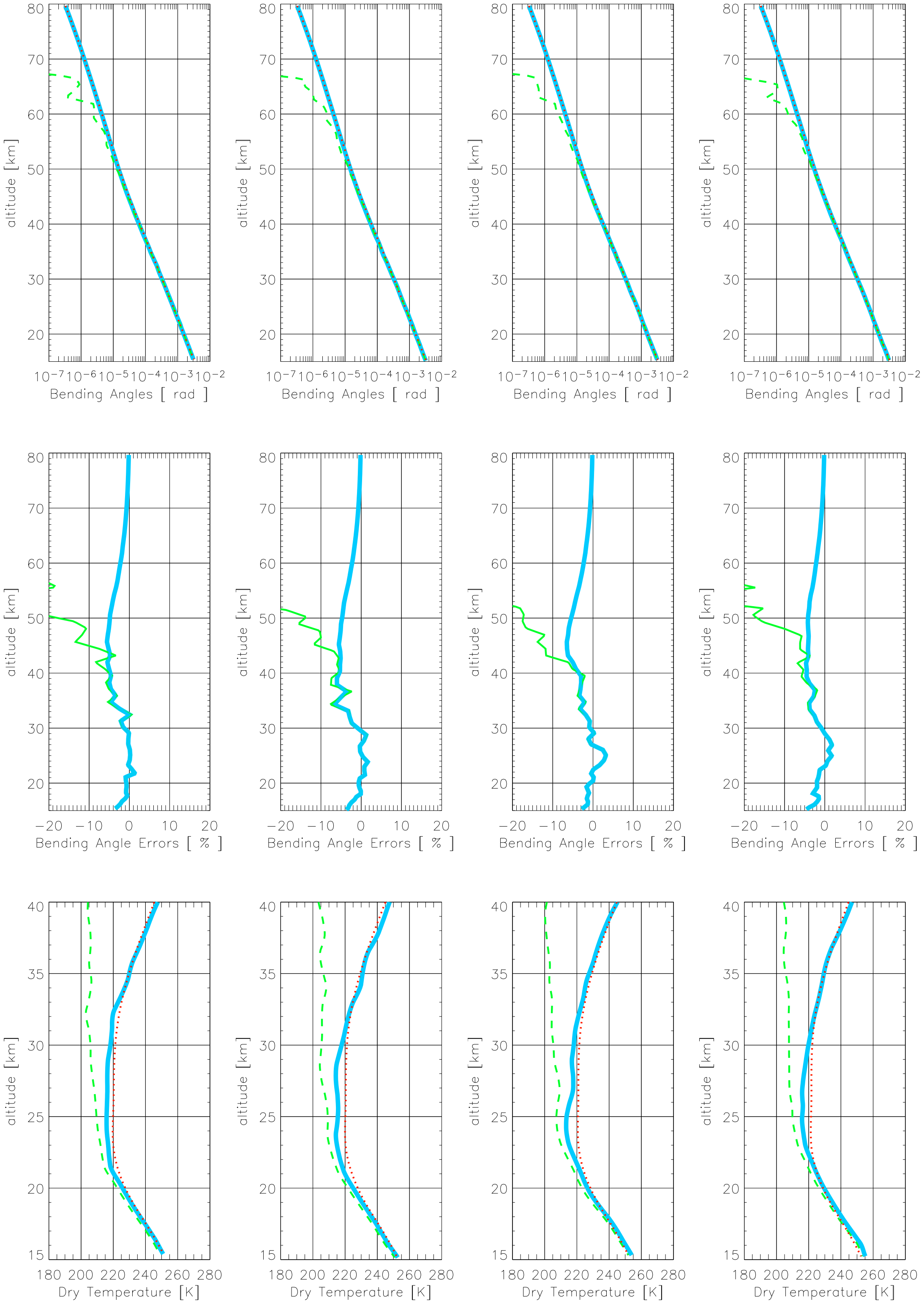

Figure 5.32. Absolute bending angle profiles (top), relative bending angle errors (middle) and corresponding temperatures (bottom) for four different occultation events with **star magnitude 2.03**. Thick light blue lines denote statistically optimized profiles. Thin red dotted lines are *a priori* profiles, while thin green solid and dashed lines are measured profiles without statistical optimization.

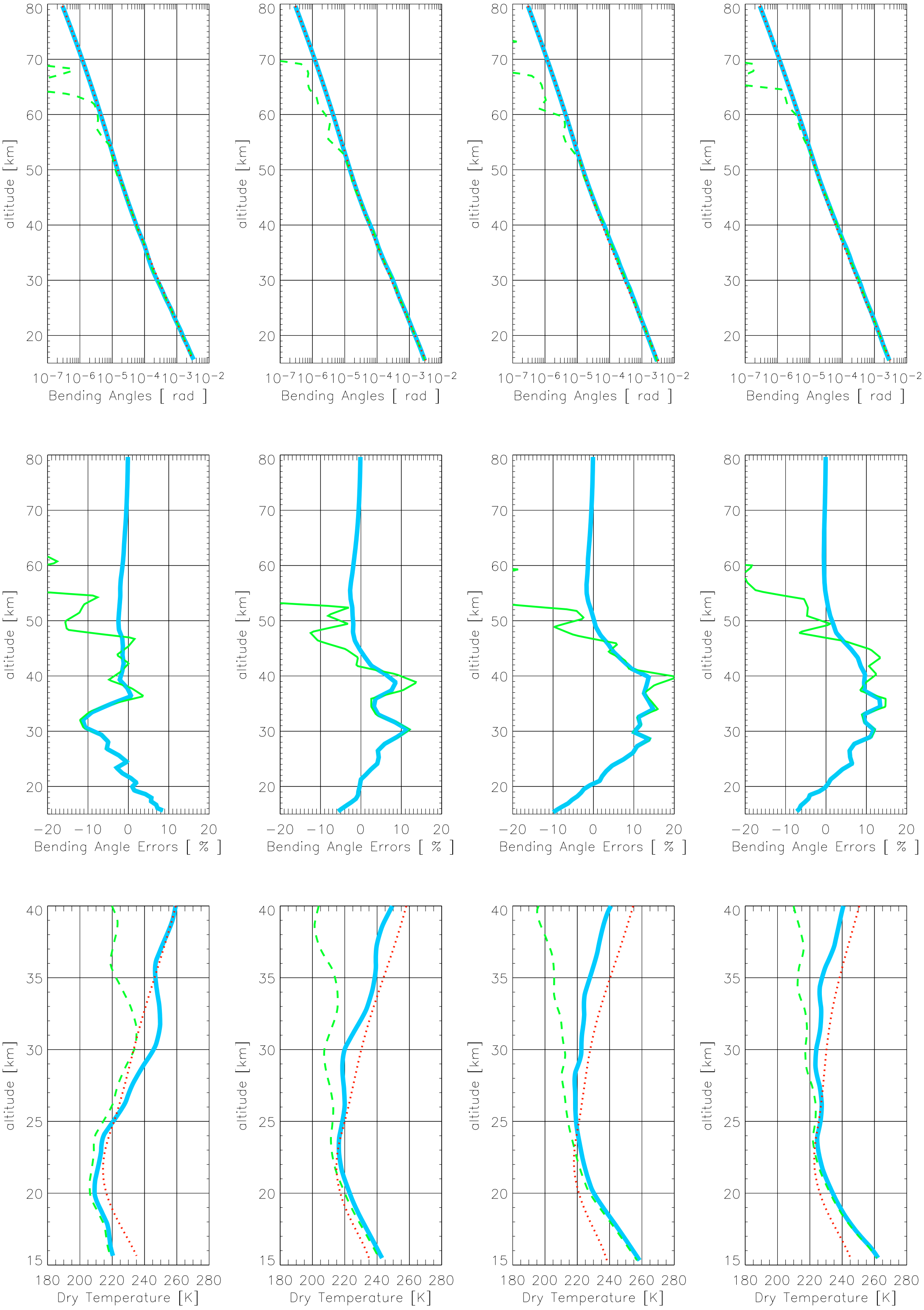

Figure 5.33. Absolute bending angle profiles (top), relative bending angle errors (middle) and corresponding temperatures (bottom) for four different occultation events with **star magnitude 2.80**. Thick light blue lines denote statistically optimized profiles. Thin red dotted lines are *a priori* profiles, while thin green solid and dashed lines are measured profiles without statistical optimization.

5.2.3 GOMOS-CHAMP Validation

We show (Fig. 5.34) GOMOS level 1b data validated with CHAMP level 2 data in altitudes between 20 and 35 km. The high attitude bias-profile $\hat{\mathbf{b}}$ is shifted to positive values for altitudes below 25 km. This may be due to the fact that only a small set of GOMOS data with very few selected stars for occultation was available. For altitudes higher than 25 km a positive bias of up to 2 K was found. In mid and high latitudes $\hat{\mathbf{b}}$ has a positive deviation below 25 km and perform equally to the hight latitude sample. The global ensemble clearly averages over negative and positive drift below 25 km and a positive tendency in $\hat{\mathbf{b}}$ can be seen.

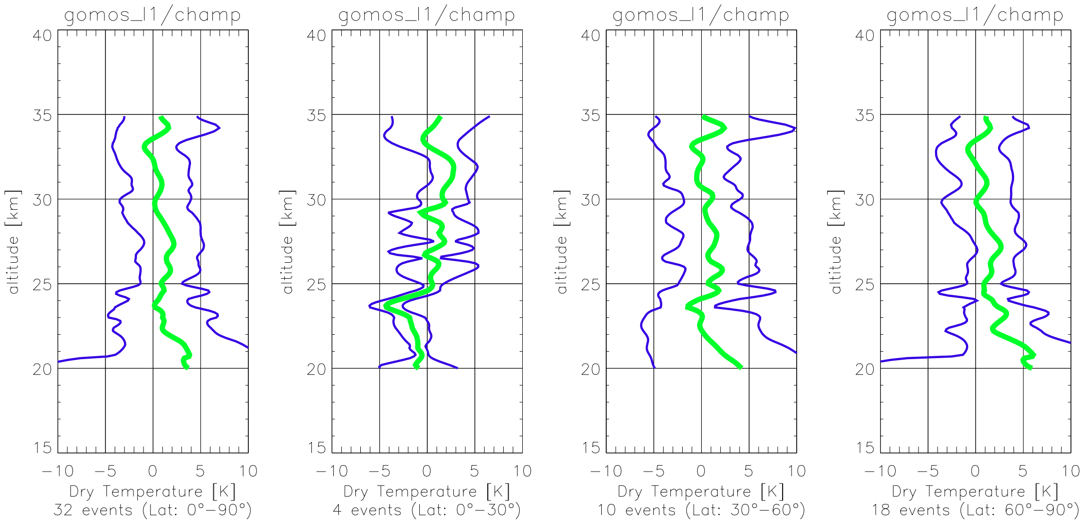

Figure 5.34. Difference profiles of GOMOS level 1b data with CHAMP level 2 with biases $\hat{\mathbf{b}}$ (bold line) and bias ± standard deviation $\hat{\mathbf{s}}$ (fine line). Criteria for coincidences: 300 km/ 3 h. From left to right profiles are shown in latitudes 0°-90°, 0°-30°, 30°-60°, 60°-90°.

5.2.4 GOMOS-MIPAS Validation

The validation with MIPAS data reveals once again the structure of retrieved GOMOS temperature profiles as already seen in the previous validation sets with CHAMP and ECMWF analysis data. In Fig. 5.35 we find small biases below 1.5 K in the low latitude regime. In the mid and high latitudes biases increase while standard deviations remain below 4 K. In high latitudes the dominant effect is an increasing bias with decreasing atmospheric altitude. The global ensemble performs equally to the ECMWF validation profiles and shows temperature biases of less than 2 K throughout the displayed regions.

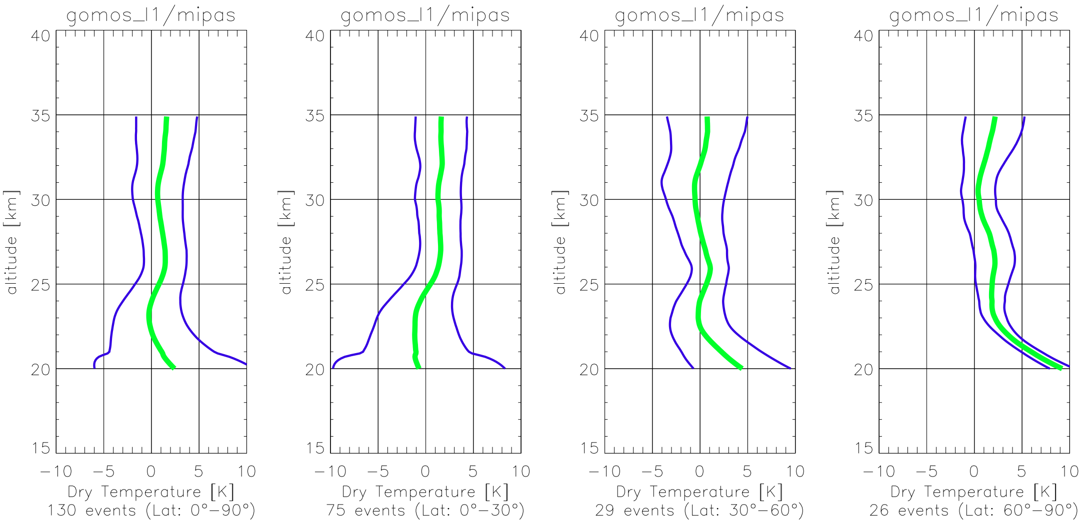

Figure 5.35. Difference profiles of GOMOS level 1b data with MIPAS level 2 with biases $\hat{\mathbf{b}}$ (bold line) and bias ± standard deviation $\hat{\mathbf{s}}$ (fine line). Criteria for coincidences: 300 km/ 3 h. From left to right profiles are shown in latitudes 0°-90°, 0°-30°, 30°-60°, 60°-90°.

5.2.5 GOMOS-ECMWF Validation

Equally to the GOMOS-CHAMP validation in Section 5.2.3 Fig. 5.36 shows similar results. GOMOS level 1b data are here validated with ECMWF T511L60 analysis data. For high latitudes and altitudes between 20 and 35 km one can see the deviation to positive values of $\hat{\mathbf{b}}$ even clearer. Due to interpolations the profiles here look more flattened than in Section 5.2.3. For altitudes higher than 25 km a positive bias of > 2 K was found. In mid and high latitudes $\hat{\mathbf{b}}$ has a positive deviation below 25 km and perform equally to the hight latitude sample. The global ensemble clearly averages over negative and positive drift below 25 km and a positive tendency in $\hat{\mathbf{b}}$ can be seen.

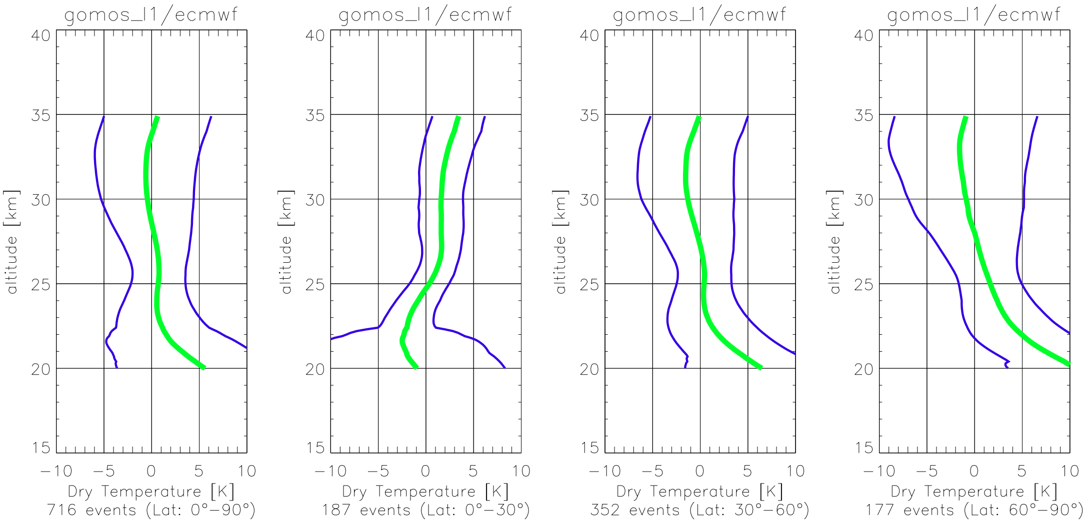

Figure 5.36. Difference profiles of GOMOS level 1b data with ECMWF T511L60 analysis data with biases $\hat{\mathbf{b}}$ (bold line) and bias ± standard deviation $\hat{\mathbf{s}}$ (fine line). Criteria for coincidences: 300 km/ 3 h. From left to right profiles are shown in latitudes 0°-90°, 0°-30°, 30°-60°, 60°-90°.

Part II SMAS
Sun Monitoring Atmospheric Sounder

6 SMAS Sensor Concept

The SMAS sensor concept was a part of the so called ACLISCOPE mission (Atmospheric and Climate Sensor Constellation Performance Explorer), developed in response to the Call for Earth Explorer Opportunity Missions [28, 29]. The primary mission objective was to provide fundamental atmospheric and solar data of highest quality for climate change research, especially on atmospheric change because the evolution of the Earth's climate system is increasingly influenced by human activities. These objective comprises climate analysis, monitoring, modeling, prediction, and process studies, all of which can be derived by the fundamental data of the mission, produced partially with the SMAS sensor concept. We discuss a realistic forward modeling and retrieval algorithm for temperature and ozone sounding developed to process data received by the planned Sun Monitor and Atmospheric Sounder (SMAS) instrument. The SMAS sensor concept employs the solar occultation technique and is primarily aiming at mesospheric profiles. The SMAS sensor provides self-calibrating transmission data, which allows accurate derivation of profiles of molecular oxygen, molecular nitrogen, atomic oxygen, and ozone and temperature. We concentrated on data between 180 nm and 250 nm to analyses transmission data for ozone and temperature profiling. In order to enable a good and fast retrieval algorithm performance, a detailed view of the absorption behavior of the solar irradiance in the considered wavelength region is necessary and will be presented in this work. In particular, some emphasis is placed on evaluating different fast forward modeling approximations for the SMAS channels in the Schumann-Runge bands.

This work only examines the SMAS sensor concept. More information about the full ACLISCOPE mission is described by [29] and in [28].

6.1 SMAS - Sun Monitor and Atmospheric Sounder

The SMAS sensor concept furnishes solar occultation measurements, which explore the Earth's atmosphere from the stratopause upwards. Further is the SMAS sensor concept self-calibrating and uses an active limb sounding technique. The self-calibration of the sensor delivers data with long-term stability, which is an important feature for climate research and monitoring. For absorptive measurements like with the SMAS sensor concept, the self-calibration results since only normalized intensities are exploited instead of absolute radiance, therefore measurements from different satellites and times can be compared without any adjustment.

The SMAS sensor primarily delivers lower atmospheric data, which are data up to the mesopause, located at about 90 km, and upper atmospheric data, which are beyond the mesopause level. Furthermore the SMAS sensor delivers solar irradiance data. From the SMAS lower atmospheric data, profiles versus height for columnar content, air and ozone density, pressure, and temperature for the mesosphere result. On the other hand, profiles versus height for columnar contents and densities of molecular oxygen, molecular nitrogen, and atomic oxygen, as well as of pressure and temperature in the upper atmosphere (the thermosphere) results from the SMAS upper atmospheric data.

The SMAS sensor is technically based on developments of the Frauenhofer Institute for Physical Measurement Techniques (FIPM) Freiburg and the University of Boulder for the SNOE (Solar Nitric Oxide Explorer) Satellite with channels at wavelength less than 35 nm and from FIPM developments for the Russian PHOTON mission. SNOE carries very similar silicon diode detectors as baselined for SMAS. Given new diamond diode detector technology is available, which furnishes even higher precision [*N. Fox*, private communications, 1999], this technology should be used for SMAS, however. A similar system is the one developed for the PHOTON mission, which includes channels at wavelengths less than 130 nm [30].

6.2 Channel Selection

Based on a sensor analysis for the SMAS sensor concept, the radiometric channels of the instrument are selected as summarized in Tab.6.1 below. The examination of the radiative interaction properties due to the Earth's atmosphere suggests a natural range in the wavelength region less than 250 nm. The spectral region therefore is the middle and extreme ultraviolet. Therefore the spectral regions for the most needed height, ranging from 50 km to 100 km, are the Schumann-Runge bands and the Herzberg continuum, both for molecular oxygen. For ozone sounding the lower edge of the continuous Hartley band is most suitable. The relevant *mesospheric channels* are thus eight channels within 180 nm and 250 nm. The signal source for such occultations needs to be the sun, because the sun provides a sufficient and continuous signal at <250 nm. Also is the brightness across the solar disk ray homogenous in the MUV wavelength region.

The locations of and distances between the eight several channels are defined such, in terms of transmission sensitivity, that a total coverage of the whole mesosphere is ensured. The bandwidth of the MUV channels is 5 nm, which is at present the technical optimum which can be obtained by the FIPM Freiburg. The baselined width of these channels and the spectral locations of and distances between the channels are defined such that, in terms of transmission sensitivity, complete coverage of the mesospheric height domain is ensured [11]. The visible channel is primarily for calibration purposes but this channel can also be used, in cloud-free situations, for tropospheric temperature evaluation based on refractive dispersion of the occulted signal amplitude profile. The 6 EUV channels are primarily for thermospheric research (temperature, densities of the absorbing species); the EUV solar radiation is responsible for photoionization at thermospheric altitudes.

The table furthermore gives some information on the source of the signal and on the intervening atmospheric species on which information is contained in SMAS occultation data. The knowledge of the density of the main atmospheric absorbing species molecular oxygen allows derivation of pressure and temperature.

Channel Number	Channel Wavelength [nm]	Solar origin of radiation	Main solar emission	Atmospheric species intervening in occultation
1 (EUV)	1-10	Corona		N_2,O_2,O
2 (EUV)	17-25	Corona	Fe X-Fe XII	N_2,O
3 (EUV)	29-35	Transition region	He II (30.4 nm)	N_2,O
4 (EUV)	50-65	Chromosphere	He I (58.4 nm)	N_2,O
5 (EUV)	70-90	Transition region	O II-O IV	N_2,O
6 (EUV)	110-130	Chromosphere	H I (121.6 nm)	O_2
7 (MUV)	184±2.5	Photosphere	continuum	O_2
8 (MUV)	190±2.5	Photosphere	continuum	O_2
9 (MUV)	195±2.5	Photosphere	continuum	O_2,O_3
10(MUV)	200±2.5	Photosphere	continuum	O_2,O_3
11(MUV)	205±2.5	Photosphere	continuum	O_2,O_3
12(MUV)	210±2.5	Photosphere	continuum	O_2,O_3
13(MUV)	224±2.5	Photosphere	continuum	O_3
14(MUV)	246±2.5	Photosphere	continuum	O_3
15(VIS)	300-700	Photosphere	continuum	Air

Table 6.1. The 15 SMAS sensor channels and characteristic parameters.

6.3 Instrument Characteristics

The SMAS sensor results from the SOL-ACES (16-220 nm UV spectroradiometer) instrument. The SMAS sensor is based on high-sensitivity, high-precision ultraviolet silicon diodes, preferably, on even more precise diamond diodes. The concept core is proven currently on the SNOE satellite and a flight model instrument with 6 channels less than 130 nm and one broadband visible channel is ready for the Russian-Ukrainian PHOTON satellite. The adaption of the available heritage for SMAS as well as the expansion of the measured wavelengths by 8 MUV channels between 180 nm and 250 nm is a rather modest modification of existing sensors.

The SMAS instrument consists primarily of three components: the *Sensor Arrangement*, the *Electronic Box* and the *Sun Pointing Assembly* (SPA). The SMAS instrument is baselined to consist of 15 radiation detector units, these are, in order to adapt to various different interfaces, designed as single small units (50 mm × 50 mm × 60 mm and with a power consumption of 0.12 W). On top there is a high-sensitivity, high-precision UV silicon or diamond diode, the sensible area is 10 mm × 10 mm and either the diode is coated with a thin metallic film or covered by a set of two interference filters. The detectors field-of-view need be limited to $\frac{1}{30}$ deg for ensuring <2 km vertical resolution.

The diode current is converted by a preamplifier, this circuit corresponds to an *Electrometer-Amplifier*. Further is the output of the preamplifier transferred via *Voltage to Frequency Converter* (VFC) to the Electronic Box.

A 16-bit-counter is involved toward the telemetry. The basic readout data rate is 10 Hz and can be directly used as sampling rate during occultation periods. For continuous solar irradiance monitoring a sampling rate of 0.1 Hz is sufficient. By trimming the offset of the preamplifier slightly to a positive value, no negative signal at the entrance of the VFCs results. For thermal stability the detector units are fixed on an aluminum plate. Furthermore, the temperature of the plate at the solar pointing assembly shall be as low as possible (below 30 deg Celsius). A variation of temperature kept less than ±3 deg during the measurement increases the accuracy of the data, therefore an electrical interface for three temperature sensors is included, providing analog signals. In the Electronic Box, the 15 VFC science signals are stored in 16 bit counters to be transferred to the telemetry. The Sun Pointing Assembly keeps the solar disk center continuously in the sensor field-of-view, with $\frac{1}{60}$ deg pointing knowledge, to ensure optimal and constant solar signal during atmospheric occultation measurements. Therefore the base plate of the SMAS Sensor Arrangement needs to be mounted on a sun pointing device, which offers constant sun pointing angles (within $\frac{1}{60}$ deg precision) during occultation.

The SMAS sensor is a small, passive, low-weight, low-power, low-data rate instrument and compatible with satellites of micro-satellite size. The main characteristics are summarized in Tab.6.2.

Characteristics	SMAS sensor
Mass	< 8 kg (total)
Power consumption	< 8 W
Max. data rate	< 2.5 kbit/sec
Total volume	$< 300\times200\times150$ mm^3
Number of channels	15 radiometric channels 1 VIS, 8 MUV, 6 EUV
Sampling rates	10/1/0.1 Hz
Precision (single indicative figure)	$< 3.10^{-3}$ (silicon diode) $< 1.10^{-3}$ (diamond diode) precision at 1 Hz rate
Sensor pointing	$< \frac{1}{30}$ deg vertical res. $< \frac{1}{60}$ deg knowledge

Table 6.2. Main characteristics of the SMAS science payload.

The primary objective is to provide with the aid of the SMAS sensor concept fundamental atmospheric and solar data for climate change research, especially on atmospheric change because the evolution of the Earth's climate system is increasingly influenced by human activities. However, indications exist that the changing thermal structure from the upper troposphere to the mesosphere is a particularly sensitive indicator of anthropogenic climate impacts. The SMAS sensor concept can furnish data to globally monitor this changing structure over the full mesosphere with very high accuracy. These solar occultation data can be used for climate monitoring and prediction, atmospheric analysis and modeling.

The main objectives for climate monitoring and prediction are to provide a global climatology of the temperature in the entire mesosphere at high absolute accuracy and vertical resolution. Further objectives are to support research into climate variability and change (inter-annual and intra-annual) and into the energetics of the climate system over the period of the mission, and thus to contribute observational input and validation of models used to predict future trends and variability. Also in addition, for atmospheric analysis and modeling, the SMAS sensor concept can provide long, consistent sets of atmospheric states for research and model development exploiting

Geographic coverage with occultation events	Globally, well balanced density over all latitudes; special feature: pairwise occ. events are needed, the mean tangent points of which shall be separated $<$ 5 min in time and $<$ 150 km horizontally
Horizontal sampling per 6 hours	$<$ 600 km latitudinally (in average)
Covered height range during occultation	50 km $<$ h $<$ 400 km (all channels together) 50 km $<$ h $<$ 120 km (8 MUV channels)
Temperature accuracy	$<$ 2 K, within 60 km $<$ h $<$ 90 km at 2 km vert. res.
Long-term stability	$<$ 0.2 K/decade (temperature)
Accuracy of other occultation variables	Consistent with the required temperature
Quality direct solar data	Continuous monitoring at 10 *sec* sampling
Radiometric precision	$< 10^{-3}(\lambda > 30$ nm),$< 10^{-2}(\lambda < 30$ nm)
Radiometric accuracy	$<$ 3% ($\lambda >$ 130 nm),$<$ 10% ($\lambda <$ 130 nm)
Timeliness	$<$ 1 day - 1 month

Table 6.3. Main requirements for the ACLISCOPE/SMAS mission.

the data of the mission together with other observations. Furthermore, a *spin-off* mission objective is that observations are provided for upper atmosphere research, e.g. for thermospheric investigations. There, observations of the densities of molecular oxygen, molecular nitrogen, and atomic oxygen, as well as pressure and temperature are provided. Also are provided direct, continuous, and accurate observations of solar irradiance for wavelengths less than 250 nm in 14 channels.

These high-utility atmospheric data can be provided with the SMAS sensor as part of the ACLISCOPE mission, which needs to be implemented as a small constellation of satellites to be able to fulfill the scientific requirements. The baseline constellation of the mission includes 6 micro-satellites in two low-earth orbits. To learn optimally about vertical and horizontal resolution properties of the occultation data, the ACLISCOPE concept includes a pair of satellites (Sat Pair) in constellation, which furnishes the necessary experimental data for research in occultation resolution and accuracy. Particularly for the horizontal resolution studies, the availability of the Sat-Pair furnishes *horizontally redundant* occultation events closely related in space (distance less than 150 km) and time (separation less than 5 min). By the aid of this Sat-Pair, investigations about *tandem retrieval* compared to single profile retrieval are possible for example. The ACLISCOPE SMAS sensors, if implemented as baselined, can provide a data set of $\sim$ 150 occultation profiles per day in the mesosphere (and above), together with continuous solar irradiance observations for wavelengths less than 250 nm. To obtain the main objectives as described above, the ACLISCOPE baseline implementation has to be compliant with the overall requirements summarized in Tab.6.3.

7 Retrieval of Atmospheric Parameters

Remote sounding of the atmospheric temperature profile and composition from Earth satellites has become a technique of major practical importance for scientific observations of the Earth's atmosphere and will clearly continue to be of importance for the foreseeable future, both for the Earth and for soundings of other planetary atmospheres.

The intensity of the sun, in certain atmospheric absorption bands, is monitored by a low orbiting satellite tracking the sun during occultation by the Earth's atmosphere. The intensity data during occultation are then used to obtain information about the absorbing species; in the SMAS case for the mesosphere and thermosphere [31, 32]. The used limb geometry is tailored to furnish a high spatial resolution, whereas the absorptive properties of the intervening medium can be related to densities of the different absorbing species. Usually absorptive occultations have been used to measure density profiles. However, from density profile of major species, pressure profiles can be calculated by integration, employing the hydrostatic equation. Furthermore, the pressure profiles can be related, by the use of the ideal gas law, to atmospheric temperature profiles.

The SMAS sensor is a self-calibrating instrument, therefore the occultation technique involves a relative measurement with normalization given by the measured solar irradiance above the atmosphere during each event. The following results are therefore independent of absolute instrument calibration or source strength (as large as a sufficiently accurate signal can be measured). This is a very important feature because it tends to negate the effects of instrument degradation over time.

The occultation technique works best for a point source, such as a star, where the vertical resolution at the tangent point is very sharp [5]. For a finite source, such as the sun, the light rays emitted from the upper and lower limb can have tangent ray heights separated by about 25-30 km (observed from low orbiting satellites).A single measurement therefore consists of light received from widely separated ray paths, which collectively sample a region of the atmosphere over which the density distribution can vary significantly. However, this problem can be solved if measurements from viewing only a small fraction of the solar disk are used [33], as is done by the SMAS sensor concept (field-of-view <2 km at tangent point). This transmission function measures the optical properties of the atmosphere in the horizontal direction, it is a good measurement of the transmissivity of the atmosphere which is a central property for the mesospheric ozone and temperature sounding. To proceed from the transmission functions to the distributions of the absorbing species (molecular oxygen and ozone for mesosphere) inversion methods must be applied. Therefore the different absorbing constituents have to be isolated first based on the total transmission function. A second step deals with the retrieval of the vertical profiles such as pressure and temperature.

7.1 Forward Model

The occultation measurement principle has been used for a long time to study the Earth's atmosphere [6]. The attenuation due to absorption is used to analyze the atmosphere. The atmospheric composition can be resolved by using the attenuation due to absorption, for the mesosphere the relevant primary absorbing constituents are molecular oxygen and ozone, absorbing the MUV solar radiation. Considering a spaceborne optical measurement device such as the SMAS ultraviolet silicon (Si) diode or diamond (Di) diode, solar radiances are measured at each height in all of the sensor channels (differing by frequency).

The SMAS sensor concept uses solar occultation with the sun as the source of radiation and satellite photo-detectors as sensors, and with the Earth's atmosphere between acting as the absorption "cell". The SMAS sensor mounted aboard a low-Earth-satellite, it measures the intensity of the solar light while the sunrays are occulted by the atmospheric limb of the Earth, either during sunrise (rising occultation event) or sunset (setting occultation event). The transmission profile (normalized intensity) thus obtained contains information about the combined limb path column density of all absorbing species. The intensity of the solar radiation passing the Earth's atmosphere is given by the combined attenuation of all absorbing species along the ray path and can be basically determined using the *Beer-Bouguer-Lambert's* law, at each frequency.

The transmission for any give individual measurement can be modeled as

$$T(t(_i)) = \int_{\Delta\lambda}\int_{\Delta\upsilon}\int_{\Delta t} T_{atm}(\lambda,\upsilon,t)W_\lambda(\lambda-\lambda_0)W_\upsilon W_t d\lambda d\upsilon dt, \tag{7.1}$$

where the transmission profile is sampled as a function of time t_i. By geometry, each sampling time corresponds to a specific tangent height. The basic sampling rate in case of the SMAS sensor is 10 Hz and corresponds to a vertical sampling of about 200 m. The integral is carried out over a wavelength band $\Delta\lambda$, properly covering the spectral width of each channel, the vertivcal field-of-view $\Delta\upsilon$, and the measurement integration time per sample, Δt. The SMAS field-of-view is pointing to sun center and designed 1/30 deg wide, corresponding to ∼2 km vertical resolution. This limited field-of-view covering only an equatorial fraction of the solar disk (<20 deg band) is useful, since the full solar disk would otherwise illuminate at any given time a height range of 25-30 km extend, severely complicating the retrieval of atmospheric profiles [34]. The channel shape function $W(\lambda-\lambda_0)$ is modeled as (normalized) Gaussian function with a half -width of 2.5 nm. Furthermore, two simple boxcar functions are used, $W = 1/\Delta\upsilon$ ($\Delta\upsilon = 1/30$ deg) and $W = 1/\Delta t$ ($\Delta t = 0.1$ sec), for properly limiting the field-of-view and time integration domains.

For given geometry and time t_i, the atmospheric transmission file $T_{atm}(\lambda,\upsilon,t)$ can be sampled as function of wavelength, field-of-view, and time, and then integrated according to Eq.7.1 to obtain the desired channel transmission $T(t_i)$. For the smooth atmospheric profiles adopted in this study, the two boxcar integrations could be well ignored and $T_{atm}(\lambda, \upsilon, t)$ was just forward modeled for different wavelengths along a single ray arriving from sun center at the time t_i.

The Schumann-Runge (SR) band region is of central importance to the absorption of solar radiation by molecular oxygen and in determining ozone concentrations. The SR bands control the limb absorption in the mesosphere from about 60 km to 100 km. The absorption system is characterized by a banded structure from 174 nm and 204 nm. The SR absorption cross section varies by about four orders of magnitude between 174 nm and 204 nm. The band system shows a regular appearance at longer wavelengths, because there exists a regularity of the spacing of vibrational and rotational energy levels. At shorter wavelengths, the number of lines from overlapping bands becomes so big that the spectrum has a quasi-random appearance. Furthermore, the SR absorption cross sections exhibit a temperature dependence, which is strongest between 192 nm and 204 nm. Fig.7.1, left panel, depicts the molecular oxygen absorption cross sections in the SR regions for a temperature of 240 K. The SR cross section data were taken from [35], computed from polynomial coefficients, including the Herzberg continuum cross section in the region between 185 nm and 204 nm. Regarding wavelengths >204 nm, the Herzberg continuum data were taken from [36] and the ozone cross section data from [37], respectively. Fig.7.1, right panel, shows exemplary SMAS transmission data modeled based on a realistic occultation event. The geometry data of the event were computed by an enhanced EGOPS (End-to-End Generic Occultation Simulator) [22, 23], an occultation software tool. Furthermore, spherically symmetric atmospheric profiles were adopted and a scanning of the atmosphere over altitude from 120 km to 50 km was used.

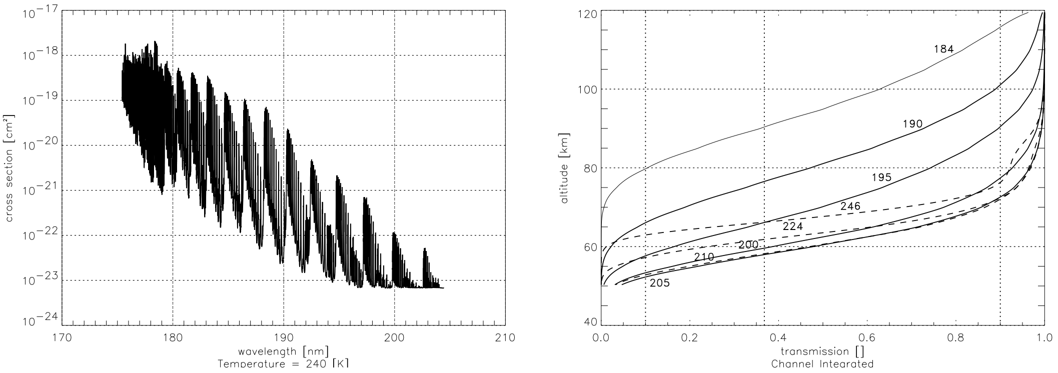

Figure 7.1. Spectral distribution of the absorption cross section of molecular oxygen in the Schumann-Runge bands (left panel) and modeled SMAS transmission profiles (right panel). In the right panel, the solid lines show the transmission profiles in the Schumann-Runge bands and the dashed lines show the transmission profiles in the Herzberg continuum and overlapping Hartley band. The annotated numbers denote the center wavelengths of the channels. The vertical dashed lines near the left and right boundary delimit the region, within which measurements are foreseen to be exploited.

For an exact calculation of the transmission profiles in the highly oscillatory SR bands, a resolution of 3000 sampling pints (0.002 nm sampling) for each channel is necessary. Using these 3000 samples of $T_{atm}(\lambda, \upsilon, t)$, Fig.7.1. right panel, shows the wavelength-integrated channel transmission profiles. For the channels >205 nm, the absorption cross sections are smooth functions - molecular oxygen Herzberg continuum and ozone Hartley band - and 0.2 nm sampling is sufficient. The Herzberg continuum comprises the wavelength region between 185 nm and 242 nm, the Hartley band those from 190 nm to 310 nm, reaching a maximum near 250 nm. Because of the large number density of molecular oxygen compared to ozone, the Herzberg continuum is important beyond 205 nm even though the cross section is small relative to the ozone cross section in the Hartley band (indicated also by the optical thicknesses illustrated in Fig.7.1). The Hartley band absorption is unimportant below 190 nm. The cross sections in the Herzberg continuum and Hartley band show a very slight temperature dependence, which can be neglected in the SMSA forward modeling.

As a result of the dense sampling needed in the SR bands, the rigorous forward model algorithm is fairly slow, and if used as part of an inversion algorithm a faster algorithm is highly desirable. In order to obtain such a faster algorithm, we evaluated the following two approximations: the piecewise integration approximation (PIA) and the optimal random selection approximation (ORSA).

Piecewise Integration Approximation (PIA)

In the PIA, SR cross sections integrated over a prescribed number of partial channels of width $\Delta\lambda$, spread over the full spectral width of a SMAS SR channel, are used to compute the channel transmissions. The needed values of the Gaussian channel shape function are properly averaged as well.

More explicitly, the PIA approximates channel transmissions $T_{ch}(s)$ as follows,

$$T_{ch}(s) = \sum_{i=\Delta\lambda_i}^{\Delta\lambda_I} T_{ch,i}(s) = \sum_{i=\Delta\lambda_i}^{\Delta\lambda_I} \exp(-\int_s \bar{\sigma}(\Delta\lambda_i, T(s))n(s)ds)\bar{W}(\Delta\lambda_i), \tag{7.2}$$

with the associated averaged temperature-dependent SR absorption cross section $\bar{\sigma}(\Delta\lambda_i, T(s))$,

$$\bar{\sigma}(\Delta\lambda, T(s)) = \frac{1}{\Delta\lambda}\int_{\Delta\lambda} \sigma(\lambda, T(s))d\lambda, \tag{7.3}$$

and averaged Gaussian weighting function $\bar{W}(\Delta\lambda_i)$, given by

$$\bar{W}(\Delta\lambda) = \frac{1}{\Delta\lambda}\int_{\Delta\lambda} W(\lambda - \lambda_0)d\lambda, \tag{7.4}$$

$$\sum_{i=\Delta\lambda_i}^{\Delta\lambda_I} \bar{W}(\Delta\lambda_i) = 1. \tag{7.5}$$

Both, the averaged SR absorption cross sections and the Gaussian weighting function are integrated over a finite equidistant wavelength region $\Delta\lambda$ for each partial channel. In turn, according to Eq.7.3, all partial channel transmissions are integrated to yield the full channel transmission. Fig.7.2, left panel (to be compared with Fig.7.1, left panel) illustrates integrated SR cross section as used in the PIA (Eq.7.4), for 30 partial channels (0.2 nm sampling). Resulting transmission profiles for the five SMAS SR channels are shown in Fig.7.2, right panel, for different numbers of partial channels.

The primary band structure of the SR bands persists to a certain degree under the PIA integration as Fig.7.2, left panel, illustrates. Fig.7.2, right panel, shows, though, that a sufficient number of partial channels is needed to accurately model the transmission. While 30 partial channels are clearly not yet a sufficient number, 300 partial channel appear to be an adequate number already, furnishing an accuracy of the approximated transmission of better than 1%. Compared to original 3000 bins per channel this is a reduction by a factor of 10 of the computational cost for sampling T_{atm}. The use of the PIA in a forward model embedded in retrieval algorithms is simple and straightforward.

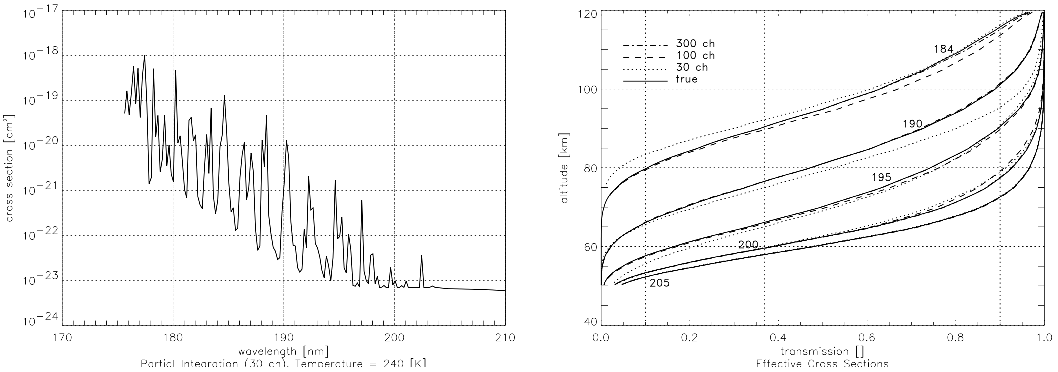

Figure 7.2. Left panel - partially integrated Schumann-Runge absorption cross sections at 240 K, for 30 partial channels. Right panel - transmission profile in the Schumann-Runge bands for full integration (true), 30 partial channels (dotted), 100 partial channels (dashed), and 300 partial channels (dashed-dotted).

Optimal Random Selection Approximation (ORSA)

The idea of ORSA is to reduce the number of sampling bins by Monte-Carlo drawing of a prescribed number of bins out of the original sample of 3000 bins. Using this Monte-Carlo drawing, for which 10^4 trials were found an adequate number of trials, we targeted to reduce the 3000 bins per Schumann-Runge channel to an optimal subset of 100 bins, i.e., a further factor of three less than what was found needed in case of the PIA discussed above. Optimality is defined in that we keep that 100 bin subset from the 10^4 randomly drawn subsets, which produces for a given atmospheric state (temperature profile) the most accurate approximated channel transmission profile compared to the exact 3000-bin per channel computation. Performing this type of ORSA for a sufficient diversity of atmospheric temperature profiles provides a number of look-up tables, which can be used in a nearest-neighbor sense for a fast algorithm based on only 100 bins per Schumann-Runge channel. Fig.7.3 illustrates the ORSA performance for a few exemplary atmospheric conditions, based on CIRA-86 profiles; the month and latitude of the profiles used is noted at each sub-panel. The left set of four sub-panels shows results for January/Equator as "true" reference, the right set for July/80 deg North. The upper-left sub-panel in both cases shows the baseline accuracy, where the ORSA results for the "true" conditions are shown. By using conditions a month and some latitudinal distance apart from the "true conditions", the other sub-panels mimic the

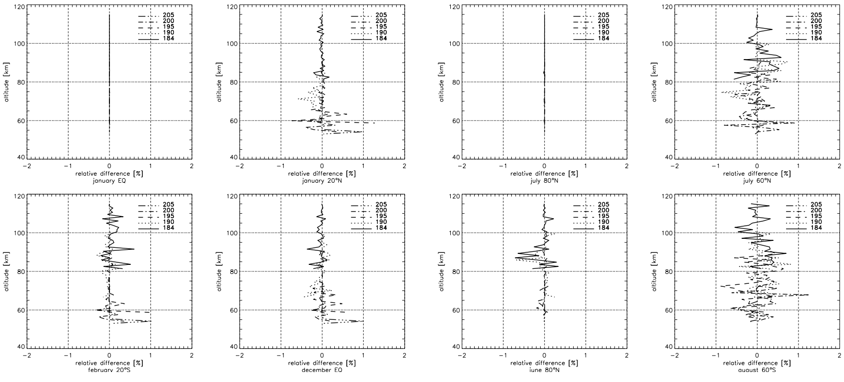

Figure 7.3. Illustration of ORSA performance for a few exemplary atmospheric conditions (January/Equator, July/80 deg North). Each sub-panel shows the accuracy of the ORSA relative to the exact forward model results, which have been taken as "true" reference.

more realistic situation, where the ORSA selection is based on *a priori* knowledge of conditions only. A set of 18 conditions over different months and latitudes seems to be sufficient for ensuring an accuracy in approximated transmissions of better than 1% for the SMAS Schumann-Runge channels based on 100 bins. Whether the factor of three advantage, in terms of reduction of bins, of the ORSA over the PIA justifies its preferred use despite of its more complicated handling (diversity of look-up tables, etc.) will be decided in the context of retrieval algorithm evaluations.

The PIA and ORSA method follows largely the in [38] described article.

7.2 Ozone and Temperature Retrieval

The wavelength dependent normalized solar intensity, as measured by the SMAS sensor device aboard of a LEO satellite during occultation of the sun by the Earth's atmosphere can be expressed with Eq.7.1. This equation corresponds to Beer-Bouguer-Lambert's law, applied to the SMAS sensor concept.

The solar intensity attenuated due to the Earth's atmosphere can be determined by considering the combined attenuation of all absorbing species along the ray path, that's exactly what the Beer-Bouguer-Lambert's law implies. The ultimate aim of the SMAS sensor concept is to deduce the atmospheric properties such as profiles about temperature, and the densities of the absorbing species, which are necessary for determination of the temperature. Hence it is necessary to establish the connection between the tangential column number densities $N_i(z)$ and the vertical number densities $n_i(z)$ of the absorbing species.

Retrieval of Ozone and Molecular Oxygen Columnar Contents with a Matrix Inversion Technique

The total optical thickness is a linear combination of the partial optical thicknesses associated with the relevant absorbing species, which are for the SMAS sensor concept molecular oxygen, ozone and a small part originate by Rayleigh scattering. The separation of the absorbing species for all involved channels will be the first step in the

SMAS retrieval before starting the vertical inversion. Step by step the SMAS retrieval scheme works as follows: (1) separation of the absorbing species and calculation of the tangential column number densities N_i (spectral inversion), (2) inversion of the Abel integral equation to obtain vertical number densities n_i, (3) from the hydrostatic equation follows the partial pressures p_i of the absorbing species and the total atmospheric pressure p, (4) the retrieval of the temperature profile from the pressure (and density) profile requires the use of the ideal gas law

$$T_\lambda(z) \rightarrow N_i(z) \rightarrow n_i(z) \rightarrow p_i(z), p(z) \rightarrow \text{Temperature}(z). \tag{7.6}$$

By definition, the column number density of the ith absorbing species is given by

$$N_i(z) \doteq \int_{-\infty}^{\infty} n_i(s) ds, \tag{7.7}$$

where ds is an element of path length along the line of sight, with origin located at the tangent point and the detector assumed to be at $s = -\infty$. The second step is made by assuming a spherically symmetric number density so that $n(s) = n(-s)$ results, this definition is general and applies to an arbitrary line of sight. Denoting the equations referring to the radius of the tangent point r_t, substituting the height coordinate z by the corresponding radius r, and furthermore by introducing the variable $r' = (s^2+r_t^2)^{1/2}$ which gives the geocentric distance of an arbitrary point along the ray path, Eq.7.6 takes the form of an *Abel integral transform* [5],

$$N_i(r_t) = 2 \int_{r_t}^{\infty} \frac{r' n_i(r')}{\sqrt{r'^2 - r_t^2}} dr', \tag{7.8}$$

where $n_i(r')$ is the number density of the ith absorbing species at a distance r' from the center of Earth. By knowing the solar spectra above the atmosphere and the absorption cross-sections, the normalized signal then is only a function of the tangential column number density $T_\lambda(r_t) = T_\lambda(N(r_t))$. These transmission data can be inverted to give the tangential column number density. Furthermore, the Abel integral equation (Eq.7.7) can be inverted to obtain the number density of the ith absorbing species at the radius r

$$n_i(r) = -\frac{1}{\pi} \int_{r_t}^{\infty} \frac{1}{\sqrt{r'^2 - r_t^2}} \frac{dN_i(r')}{dr'} dr'. \tag{7.9}$$

From the determined vertical number densities it is easy to calculate the residual atmospheric parameters as pressure and temperature. The pressure profiles can be calculated by inserting the vertical number densities in the hydrostatic equation. Furthermore, the temperature profile can be determined by inserting the pressure profile (the absolute pressure p) together with the density profile into the ideal gas law.

The spectral inversion problem for the SMAS mesospheric data involves eight channels with overlapping contributions from molecular oxygen, ozone and air because the SMAS is an eight-channel MUV radiometer in this context. The inversion program performs the conversion of the measured tangential atmospheric transmission data from the eight MUV channels into columnar contents describing the vertical distribution of the three absorbing constituents molecular oxygen, ozone and air. The transmission function is given by Beer-Bouguer-Lambert's law (Eq.7.1) which includes a wavelength dependent optical thickness according to the absorbing species. The relationship between the optical thickness and the normalized transmission function can be used for all channels, thus follows

$$\ln\left(\frac{I_k(z)}{I_{k,0}}\right) = -\sigma_{O_2,a,k}(z)N_{O_2}(z) - \sigma_{O_3,a,k}(z)N_{O_3}(z) - \sigma_{O_{Air},a,k}(z)N_{O_{Air}}(z) \qquad (7.10)$$

for $k = 1\ldots8$, where the subscript index k denotes the SMAS channels (e.g., for $k = 1 \Rightarrow \lambda = 184\,\mathrm{nm}$, and so on) - as a first approximation effective absorption cross sections are used (integrated over the spectral width of each channel). The SMAS inversion thus is an over-determined linear equation system consisting of eight equation for three unknowns, each equation corresponds to one channel. Eq.7.9 can be put into matrix form, with $\mathbf{x} = (N_{O_2}(z), N_{O_3}(z), N_{Air}(z))$ and $\mathbf{y} = \left(\ln\left(\frac{I_1(z)}{I_{1,0}}\right), \cdots, \ln\left(\frac{I_1(z)}{I_{8,0}}\right)\right)$, and a design matrix $\mathbf{K}$ with matrix elements matrix element $K_{k,i} = -\sigma_{a,k,i}$ (i corresponds to the number of absorbing species). This matrix equation $\mathbf{Kx} = \mathbf{y}$, can be inverted (generalized least-square solution; e.g., [39]) to produce the solution

$$\mathbf{x} = \left(\mathbf{K}^T\mathbf{K}\right)^{-1}\mathbf{K}^T\mathbf{y}. \qquad (7.11)$$

Eq.7.11 produces a value of the tangential column number density of molecular oxygen, ozone and air. Applying Eq.7.11 to all rays built up profiles of tangential column number density for all absorbing species. Note that practically not all eight equations (channels) are involved at each height, since only those channels are included for which $0.1 \leq T_\lambda \leq 0.9$ is fulfilled at the given height.

Abel Inversion of Columnar Contents to Density Profiles

In this paragraph a numerical inversion scheme is developed for species which decrease approximately exponentially with altitude for determining the number density profile (for both molecular oxygen and ozone). The vertical number densities of the absorbing species can be calculated with Eq.7.8. This equation is a algebraic form of the Abel integral equation relating the tangential column number densities $N_i(z)$ at different heights to vertical density profile $n_i(z)$ ($r = R_E + z$). For numerical computations, Eq.7.8 has a disadvantage because there exists a singularity at the lower integral boundary. That disadvantage can be evaded with a method developed by [40].

In order to perform the inversion with an algebraically convenient form Eq.7.8 is discretized with the so called *onion-peeling* method which corresponds to a division of the atmosphere into shells. The depth of each shell corresponds to the sampling rate of the measurement device, which is 10 Hz for the SMAS sensor concept. The inversion algorithm has to be done for all relevant absorbing species, thus the subscript index is suppressed further on. Eq.7.8 is discretized assuming first that the derivations of the tangential number densities of each species vary linearly inside each shell. The Abel integral equation can be put into matrix form, discretized into m shells (the subscript index $j = 1, 2, \cdots, m$ corresponds to a finite number of mean radii r_j) and regarded as a function of the independent impact parameters r_j or r_l corresponding to the mean radii (further on the subscript index t denoting the tangent point is neglected). Doing with thus Eq.7.8 can be written as

$$\mathbf{n} = \mathbf{A}\mathbf{N}_d, \qquad (7.12)$$

with $\mathbf{n} = (n_1, n_2 \cdots, n_m)$ and $\mathbf{N}_d = \big((\frac{dN}{dr})_1, (\frac{dN}{dr})_2, \cdots, (\frac{dN}{dr})_m\big)$, and

$$A_{jl} = \begin{cases} 0 & , \quad l < j \\ -\frac{1}{\pi(r_{j+1}-r_j)}\left[\sqrt{r_{j+1}^2 - r_i^2} - r_{j+1}\ln\left(\frac{r_{j+1}+\sqrt{r_{j+1}^2-r_j^2}}{r_l}\right)\right] & , \quad l = j \\ \frac{1}{\pi}\left\{\frac{1}{r_l-r_{l-1}}\left[\sqrt{r_l^2 - r_j^2} - \sqrt{r_{l-1}^2 - r_j^2} - r_{l-1}\ln\left(\frac{r_l+\sqrt{r_l^2-r_j^2}}{r_{l-1}+\sqrt{r_{l-1}^2-r_j^2}}\right)\right]\right. & \\ \left. -\frac{1}{r_{l+1}-r_l}\left[\sqrt{r_{l+1}^2 - r_j^2} - \sqrt{r_l^2 - r_j^2} - r_{l+1}\ln\left(\frac{r_{l+1}+\sqrt{r_{l+1}^2-r_l^2}}{r_l+\sqrt{r_l^2-r_j^2}}\right)\right]\right\} & , \quad l > j \end{cases} \tag{7.13}$$

being the elements of an $(m \times m)$ triangular matrix $\mathbf{A}$ [40]. The kernel $(r'^2 - r^2)^{-\frac{1}{2}}$ in Eq.7.8 determines the structure, thus the diagonal elements in $\mathbf{A}$ are far the largest ones and they are falling off rapidly away from diagonal. In principle, the r_j's can be chosen in arbitrarily, but we chose equidistant levels for convenience.

Retrieval of Temperature Profiles

From the retrieved density profiles pressure profiles can be calculated by integration employing the hydrostatic equation. For the SMAS data analysis only the partial pressure of molecular oxygen is useful, from the known distribution of the atmosphere as mixture of gases (for molecular oxygen 21% per volume) the total pressure result. The contribution of the ozone partial pressure to the total pressure is negligible compared to the contribution of molecular oxygen. Thus only the data of molecular oxygen will be used to retrieve the pressure and temperature profiles.

Therefore the molecular oxygen number density profile $n_{O_2}(r)$ has to be related to the molecular mass density profile $\rho_{O_2,m}(r)$. The pressure can be obtained by integrating the hydrostatic equation

$$p_{O_2}(r) = \int_r^\infty g(r')\rho_{O_2,m}(r')dr', \tag{7.14}$$

where $g(r')$ denotes the local acceleration of gravity. Using the total atmospheric pressure profile, the temperature profile of the middle atmosphere follows. The retrieval of the atmospheric temperature profile from density profiles and from the partial $p_{O_2}(r)$ and total pressure profile $p(r)$ uses the ideal gas law. In each shell, the temperature $T(r)$ can be calculated as

$$T(r) = \frac{p(r)}{n(r)k_B}, \tag{7.15}$$

where k_B denotes the Boltzmann constant.

8 Results and Discussion

In this Chapter we present retrieval results, derived from the SMAS Schumann-Runge and Hartley band channels 7 to 14. Monitoring the mesosphere by the SMAS solar occultation sensor starts with the measurement of signal intensity profiles normalized to transmission profiles, one for each channel. The sequential inversion process starts with a spectral inversion of transmission to molecular oxygen and ozone columnar content profiles, followed by a vertical inversion via Abelian transform to obtain an ozone number density profile from the ozone columnar content. The spectral inversion converts the transmission data form the eight channels into columnar contents describing the horizontally-integrated vertical distribution of the two main absorber molecular oxygen and ozone.

Month	Latitude	O_2 and temperature: CIRA-86 model	O_3 profile: FASCODE model
Januray	Equator MidLat. HighLat.	Equator 40 deg North 60 deg North	Tropical / model 5 MidLat. Winter / model 3 SubArctic Winter / model 4
March	Equator MidLat. HighLat.	Equator 40 deg North 60 deg North	Tropical / model 5 MidLat. Summer / model 2 SubArctic Summer / model 4
July	Equator MidLat. HighLat.	Equator 40 deg North 60 deg North	Tropical / model 5 MidLat. Summer / model 2 SubArctic Summer
October	Equator MidLat. HighLat.	Equator 40 deg North 60 deg North	Tropical / model 5 MidLat. Winter / model 3 SubArctic Winter / model 4

Table 8.1. Temperature and density profiles.

Tab.8.1 indicates the for the SMAS forward model and temperature and ozone retrieval used molecular oxygen, ozone and temperature profiles. The temperature and molecular oxygen profiles are calculated from the CIRA-86 model and the ozone profiles are taken from the AFGL-TR-86 data (FASCODE model), respectively. In the next two Sections results from the SMAS ozone/molecular oxygen and temperature retrieval for three different cases are shown: (1) the upper panel shows the situation at the Equator, (2) the middle panel for mid latitudes (40 deg North) and (3) the lower panel denotes the situation at high latitudes (60 deg North).

8.1 Retrieved Ozone and Molecular Oxygen Profiles

The Eqs.7.12 and 7.13 can be used to calculate the vertical number densities of both molecular oxygen and ozone from the tangential column number densities. The resulting density profiles are illustrated in Figs.8.1 - 8.4 . The lowest impact parameter r_1 corresponds to the 55 km level, where $T_\lambda > 0.1$ for the lowest-reaching channel, while the uppermost impact parameter r_m corresponds to an altitude of about 115 km. As known from similar cases in other occultation techniques (e.g., [41]), the Abel inversion of course propagate not only the signal but measurements into the density profile.

This is, in particular, visible in the retrieved ozone column number density profile at heights > 80 km. For molecular oxygen a stable inversion results up to an altitude of about 115 km. The departure from the ideal case follows from the discretized solution of the Abel integral equation. To calculate the vertical ozone number density is it needful to use the statistical optimization routine as described in Chapter 3.3.2 (Eq.7.11), where α_b is the background and α_o the observed ozone column number density profile, respectively. The correlation length L for the background and observation error covariance was set to 6 km. As a background profile a CIRA-86 climatology was chosen and the background errors σ_i and σ_j were assumed to be 20%.

The resulting profiles for four different months (January, March, July and October) are illustrated in the Figs.8.1 - 8.4, with the densities given over a logarithmic scale (left panels). The molecular oxygen density was calculated from the CIRA-86 model and the ozone density was based on AFGL-TR-86 data for three different lines of latitude (Equator - top panels, 40 deg north - middle panel, and 60 deg north - bottom panel). As reference the ideal cases are plotted for both molecular oxygen and ozone (solid black lines). Furthermore, vertical number density profiles are illustrated with some superposed noise generated by the SMAS detector.

Two cases are considered: (1) 0.1% noise at 10 Hz-sampled transmission data, corresponds to diamond diode detectors (blue dotted lines, left panel), and (2) 0.3% noise at transmission data, corresponds to silicon diode detectors (red dashed lines). The relative departure of the retrieved atmospheric molecular oxygen and ozone density profiles are shown in the middle and right panel of the Figs.8.1 - 8.4, the solid lines references molecular oxygen density and the dotted lines ozone density, respectively. The vertical resolution is about 2 km. A relative ozone retrieval error of less than ±2% in most of the height domain of interest up to 90 km is found for the 0.1% and 0.3% measurement error case and for molecular oxygen a relative difference less than ±2% is found up to an altitude of about 100 km. The error incurred by the discretized solution of the Abel transform with a matrix inversion technique and due to the numerical programming of the columnar contents profile is very small an negligible.

The strong deviation of the profiles compared with the true profile for the altitude region above 105 km results due to the transient phenomenon given by the initial value of the molecular oxygen and ozone profile at an altitude of about 120 km, these initialization is necessary to start the retrieval algorithm. Therefore only profiles up to an altitude of 105 km are reasonable and only results up to this high should be used for further applications.

The same cases are considered in the further steps in the temperature retrieval processing. The noise corresponds to the so called *Gaussian white noise* and was modeled as such. This describes a for any time normally (Gaussian) distributed random process and is noted in the plot as rms-error value which is equal to the standard deviation. The values describe the percental deviation from the noise free measured signal. Hence the spectral amplitude of white noise corresponds to $S = S(\nu)$ and the corresponding autocorrelation function is a Dirac delta function $R(t) = S\delta(t)$. Thus white noise is noise which is uncorrelated from one time instant to another [42]. Molecular oxygen absorbs MUV/EUV in the Schumann-Runge absorption system up to the upper boundary at 242 nm, ozone only absorbs for the most part in the Hartley band with the lower boundary at 200 nm.

It results, that the channels from 184 nm up to 195 nm primarily detect the molecular oxygen-attenuated solar radiation. On the other hand the channels from 210 nm up to 246 nm primarily or entirely detect ozone-attenuated solar radiation. For the inversion of the molecular oxygen vertical number density the influence of noise is very small, therefore the inversion is very stable up to the top altitude of about 110 km. The inversion of the ozone vertical number density is very sensitive against the rms-error at high altitudes. This can be readily explained considering the SMAS transmission plot (Figs.7.1), because no appreciable signal from the 210-to-246-nm-channels exists at altitudes above 80 km. Thus the ozone profile can be detected only up to an altitude of about 80 km, which is sufficient to scan the mesosphere, however. Ozone concentration above the mesosphere are generally negligible.

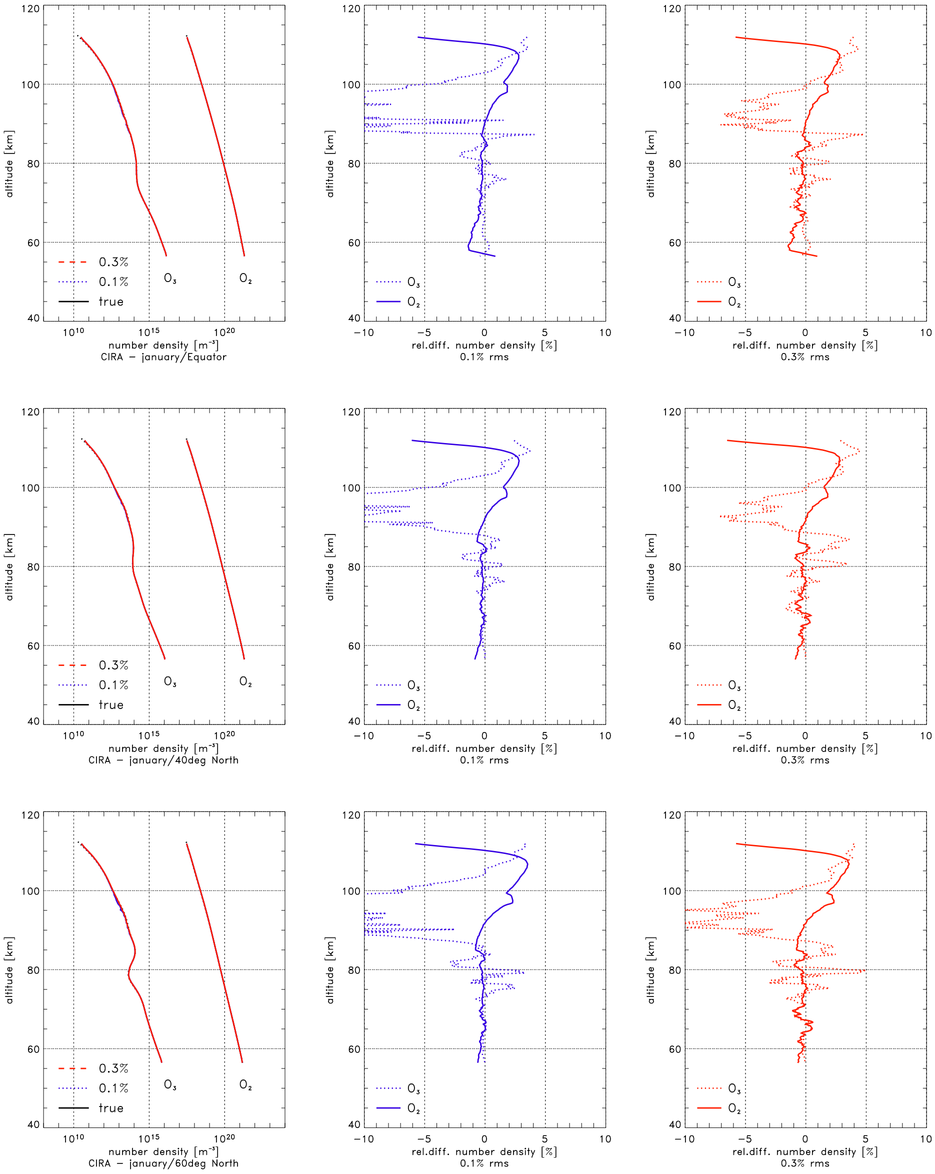

Figure 8.1. Vertical number density of molecular oxygen and ozone resulting from the SMAS forward model. The molecular oxygen density used here was calculated from the CIRA-86 model (January) and the ozone density was based on AFGL-TR-86 data. The blue lines refer the superimposed rms-error of 0.1% and the red lines refer an rms-error of 0.3%, respectively.

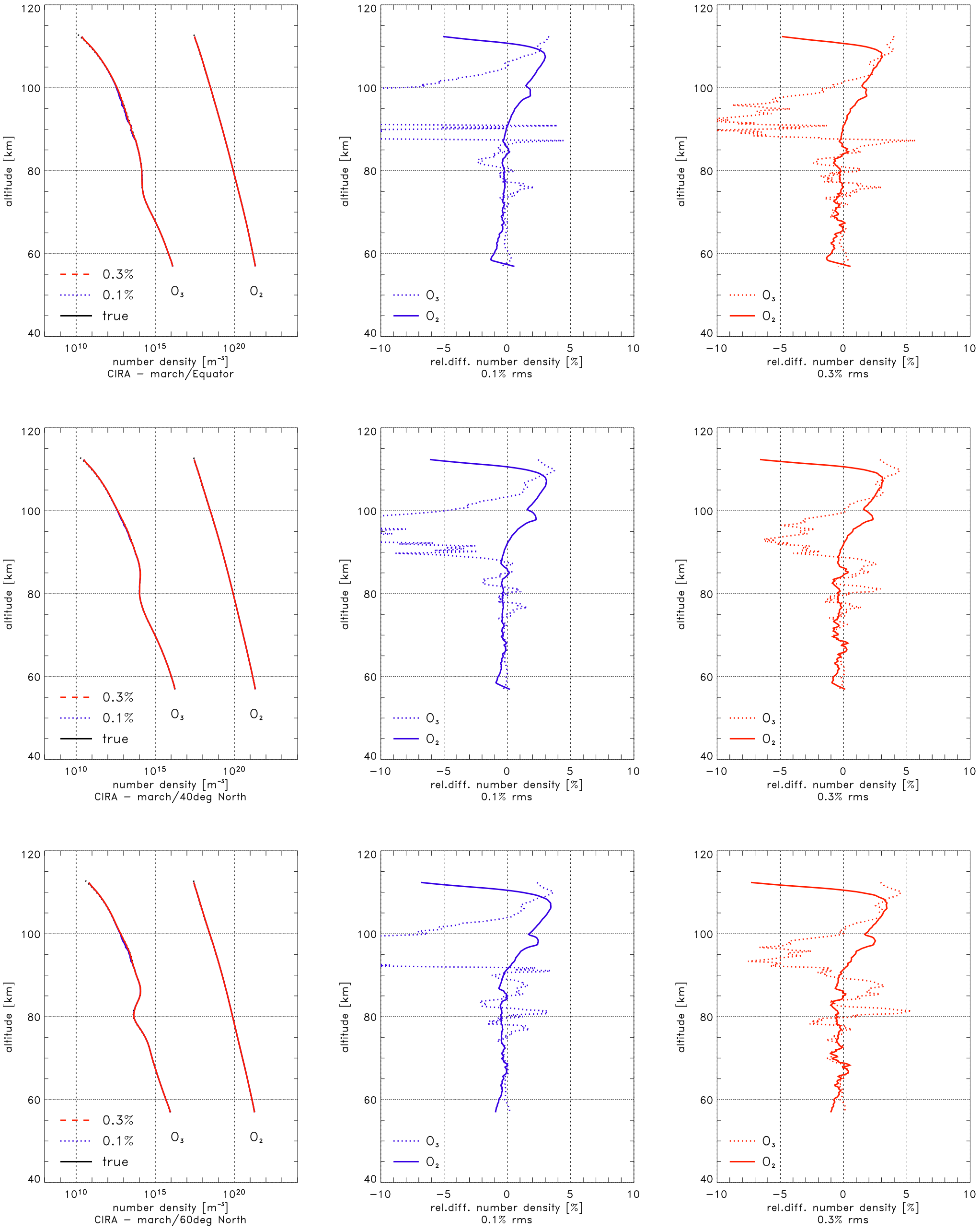

Figure 8.2. Vertical number density of molecular oxygen and ozone resulting from the SMAS forward model. The molecular oxygen density used here was calculated from the CIRA-86 model (March) and the ozone density was based on AFGL-TR-86 data. The blue lines refer the superimposed rms-error of 0.1% and the red lines refer an rms-error of 0.3%, respectively.

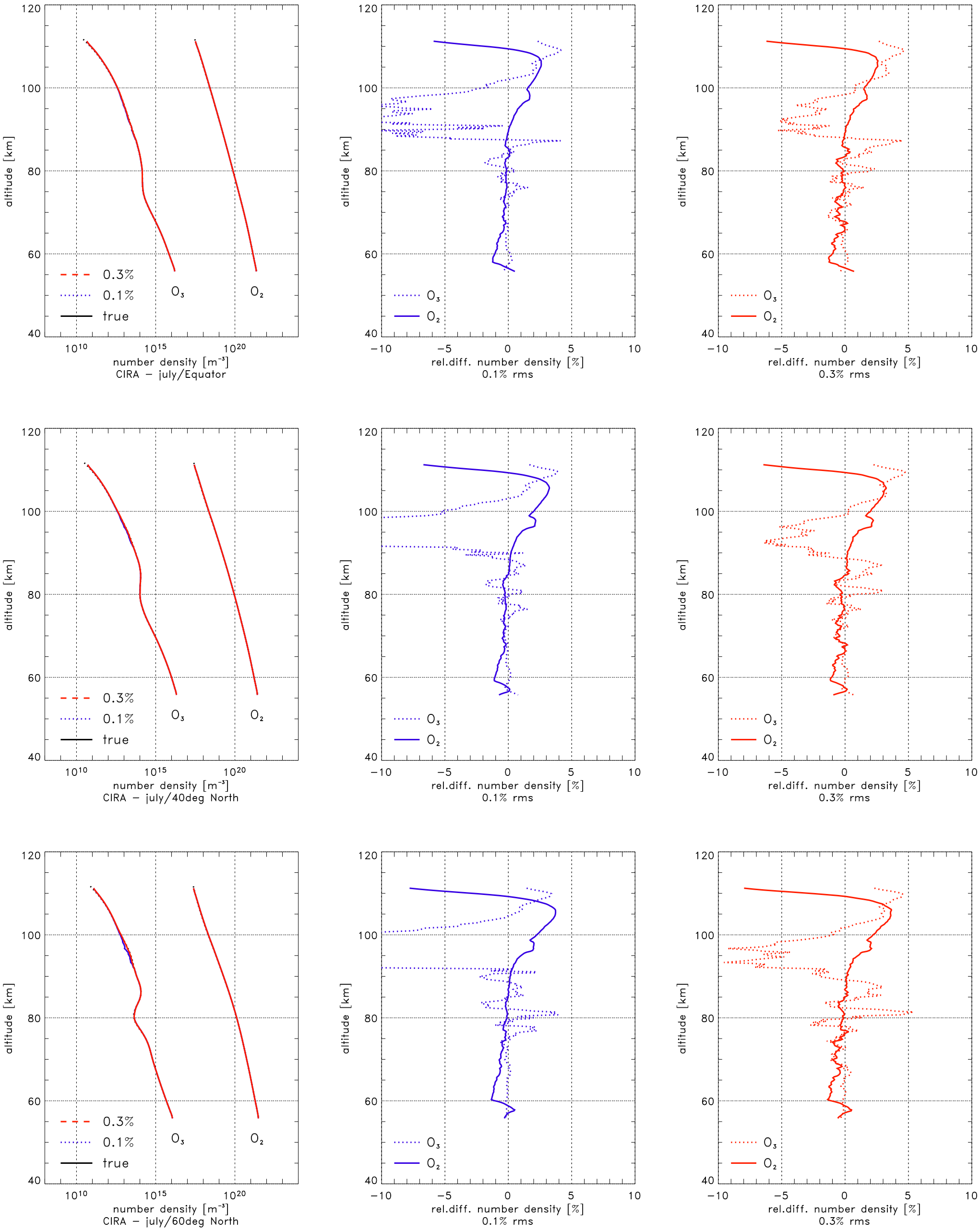

Figure 8.3. Vertical number density of molecular oxygen and ozone resulting from the SMAS forward model. The molecular oxygen density used here was calculated from the CIRA-86 model (July) and the ozone density was based on AFGL-TR-86 data. The blue lines refer the superimposed error of 0.1% and the red lines refer an rms-error of 0.3%, respectively.

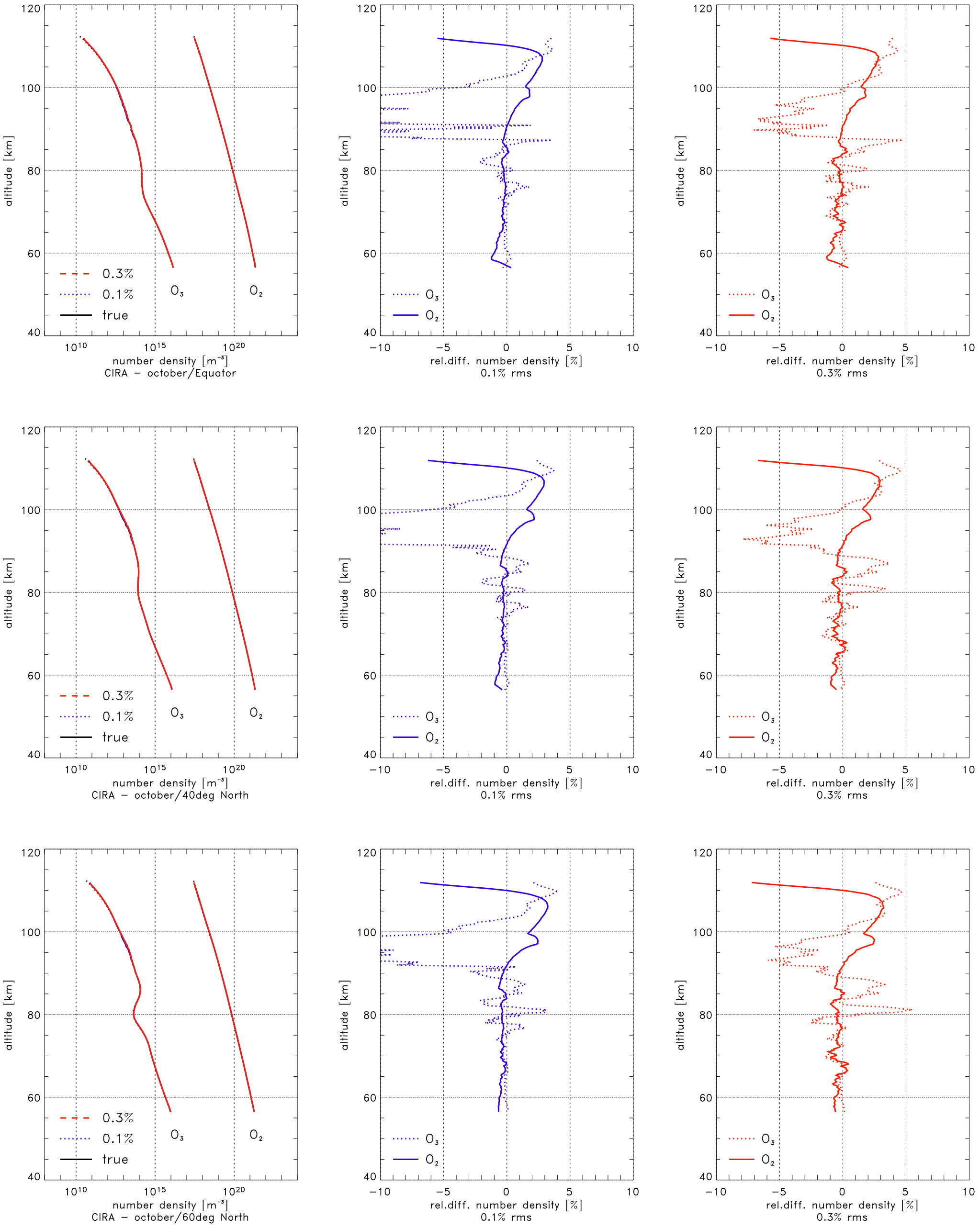

Figure 8.4. Vertical number density of molecular oxygen and ozone resulting from the SMAS forward model. The molecular oxygen density used here was calculated from the CIRA-86 model (October) and the ozone density was based on AFGL-TR-86 data. The blue lines refer the superimposed error of 0.1% and the red lines refer an rms-error of 0.3%, respectively.

8.2 Retrieved Temperature Profiles

This Section illustrates the temperature profile retrieved from the total pressure profile. As described in the Section above four different month (January, March, July and October) for the northern hemisphere are shown (Figs.8.5 - 8.8). From the plot follows that an accurate profile of the temperature can be obtained with the SMAS sensor concept, analogous to the density profiles of molecular oxygen, up to an altitude of about 105 km. Also this figures shows the the influence of the rms-error, and no bias departure of the retrieved temperature from residual errors in the discretization of the Abel integral (the numerical solution of the Abel transform), the spectral inversion procedure and the numerical solution of the hydrostatic integral has been observed.

As described at the beginning of Chapter 8, results of the SMAS temperature retrieval for three different cases are shown: (1) the upper panel shows the situation at the Equator, (2) the middle panel for mid latitudes (40 deg North) and (3) the lower panel denotes the situation at high latitudes (60 deg North). The left panel of the Figs.8.5 - 8.8 illustrates the temperature for the ideal case (black solid line), the retrieved temperatures with superimposed rms-error (blue dotted line: 0.1% rms-error, red dashed line: 0.3% rms-error). The middle and right panel illustrates the case of 0.1% rms-error (blue line) and 0.3% rms-error (red line), respectively. The vertical resolution of the profiles is about 2 km.

The error of the retrieved temperature profile for the 0.1% error case is less than 2 K for the height region up to an altitude of about 105 km. The situation is similar with the superimposed rms-error of 0.3%, where a temperature profile slightly more noisy but still accurate to better than 2 K up to about 105 km results. Generally, as expected, the temperature accuracy decreases with increasing rms-error on transmission. In summary, a good estimation of the temperature profile over the whole mesosphere can be done with the SMAS sensor concept.

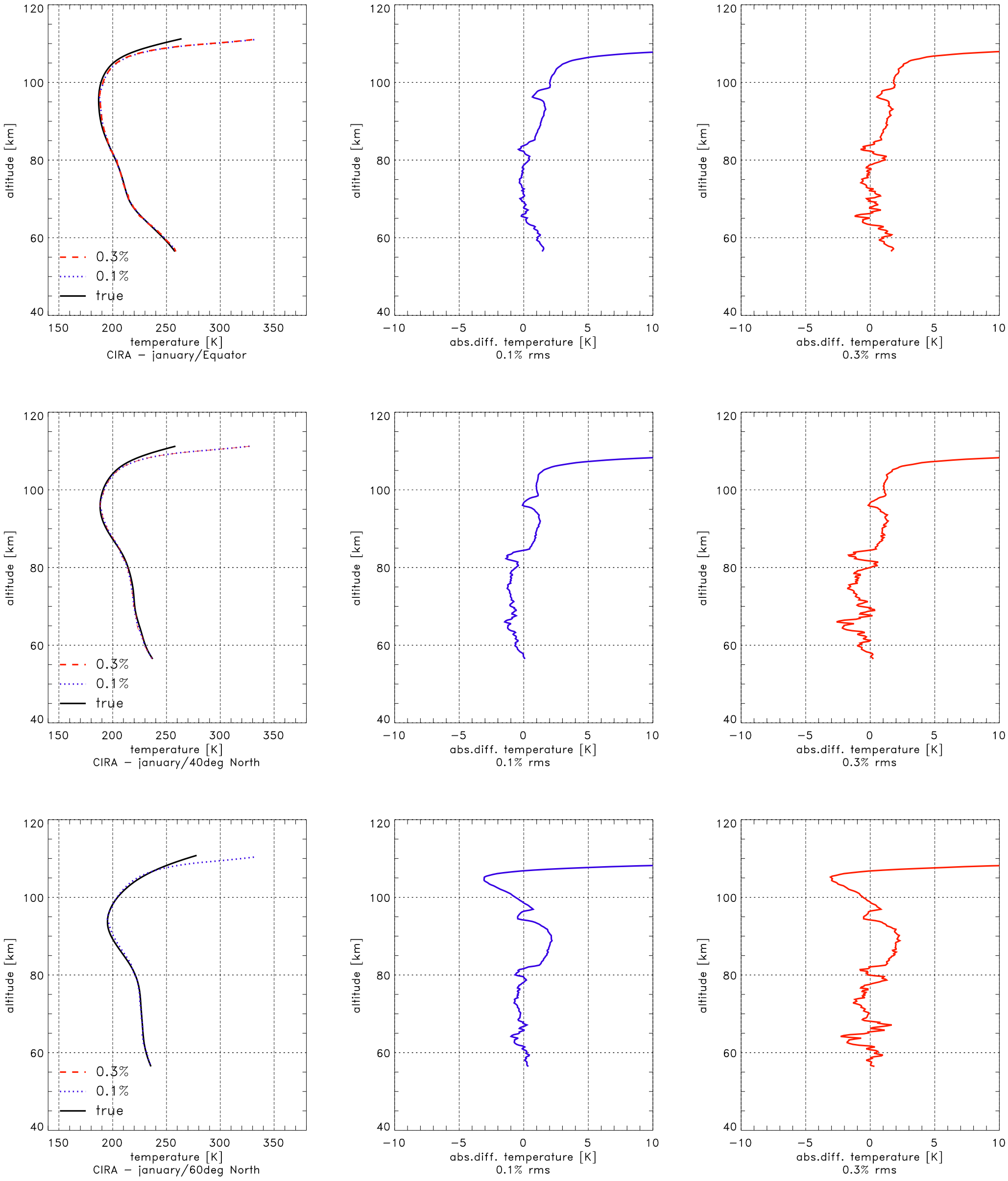

Figure 8.5. Temperature profiles resulting from the SMAS forward model and absolute departure of the retrieved atmospheric temperature for January/northern hemisphere. The blue lines refer the superimposed error of 0.1% and the red lines refer an rms-error of 0.3%, respectively. The black solid line in the left panel denotes the true case.

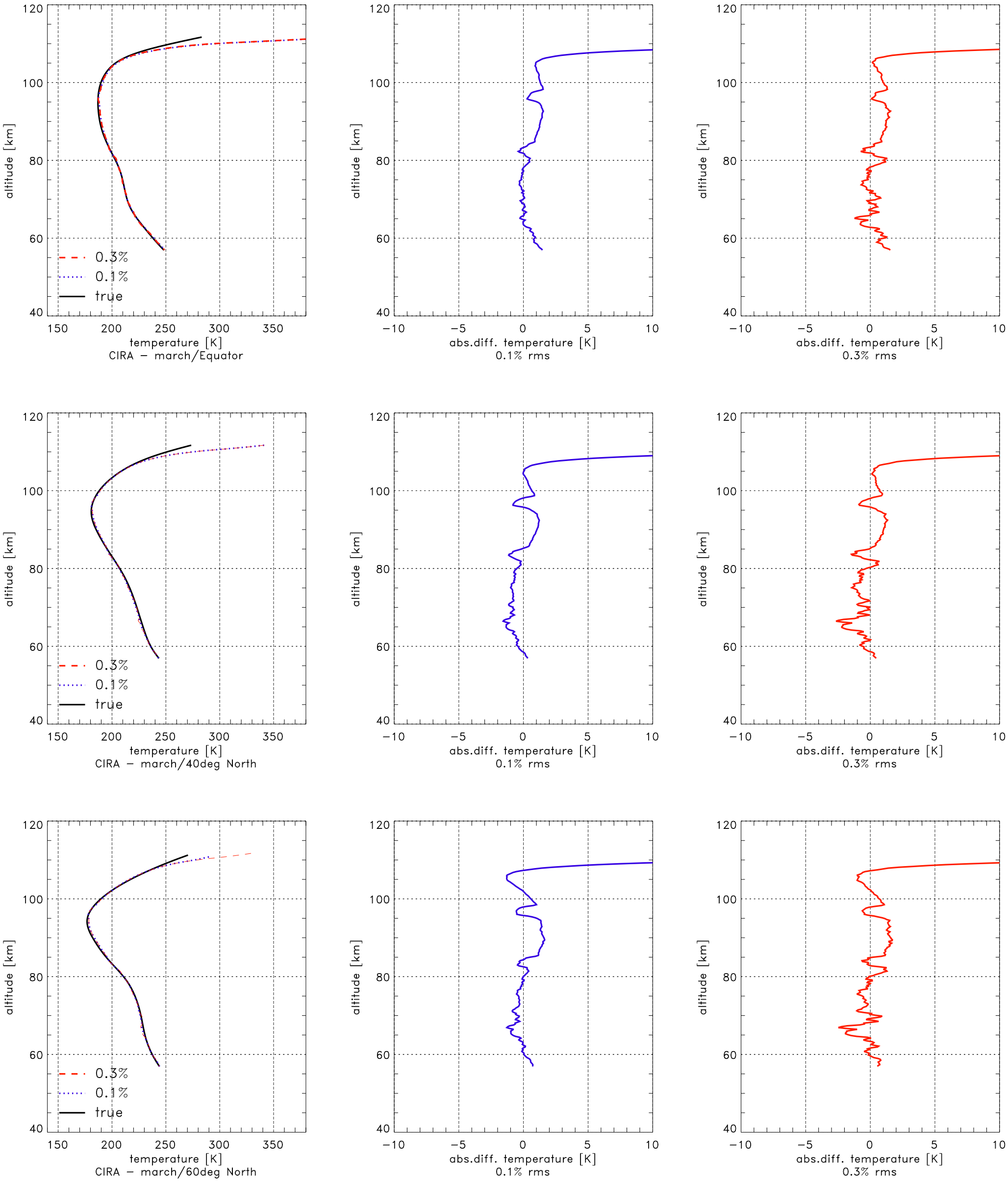

Figure 8.6. Temperature profiles resulting from the SMAS forward model and absolute departure of the retrieved atmospheric temperature for March/northern hemisphere. The blue lines refer the superimposed error of 0.1% and the red lines refer an rms-error of 0.3%, respectively. The black solid line in the left panel denotes the true case.

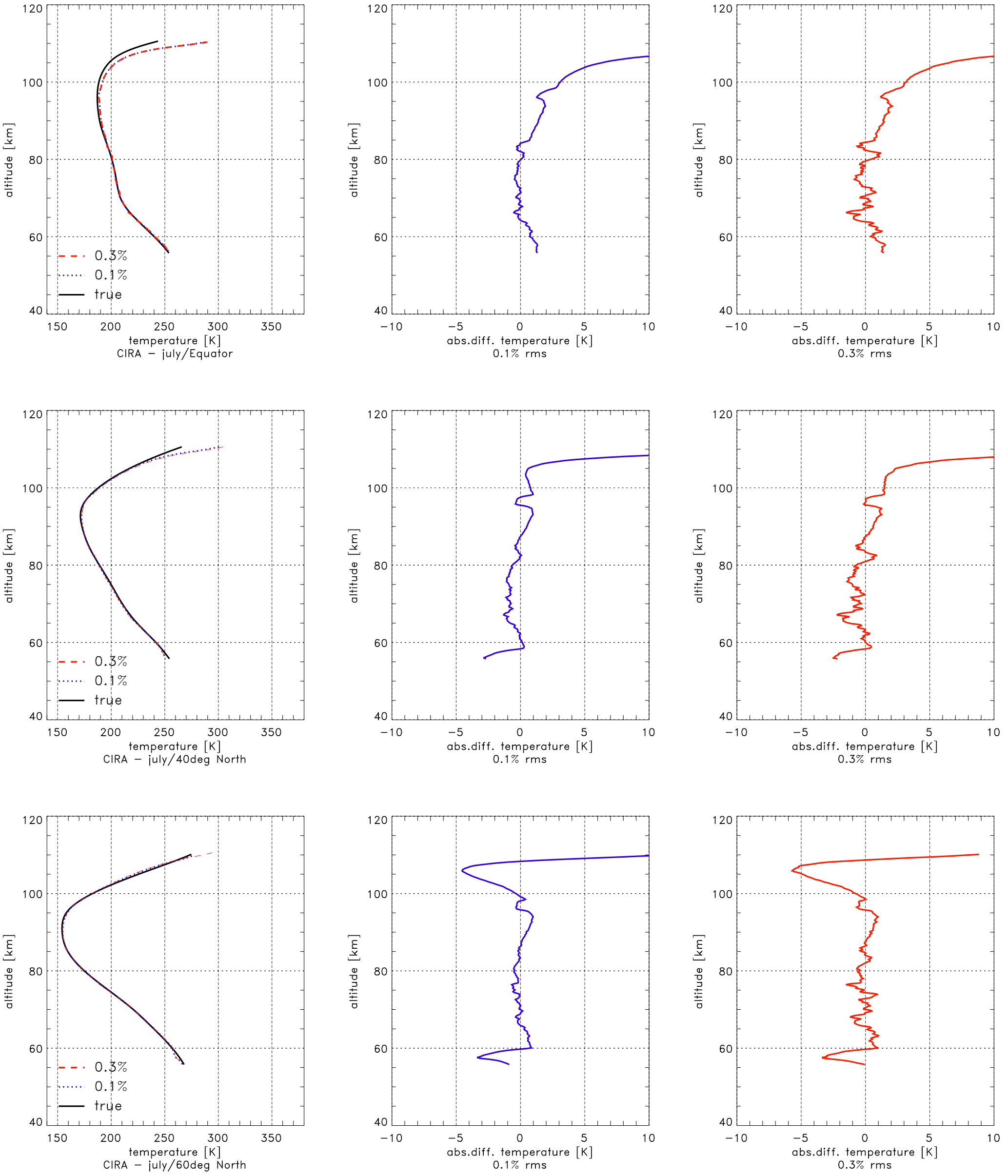

Figure 8.7. Temperature profiles resulting from the SMAS forward model and absolute departure of the retrieved atmospheric temperature for July/northern hemisphere. The blue lines refer the superimposed error of 0.1% and the red lines refer an rms-error of 0.3%, respectively. The black solid line in the left panel denotes the true case.

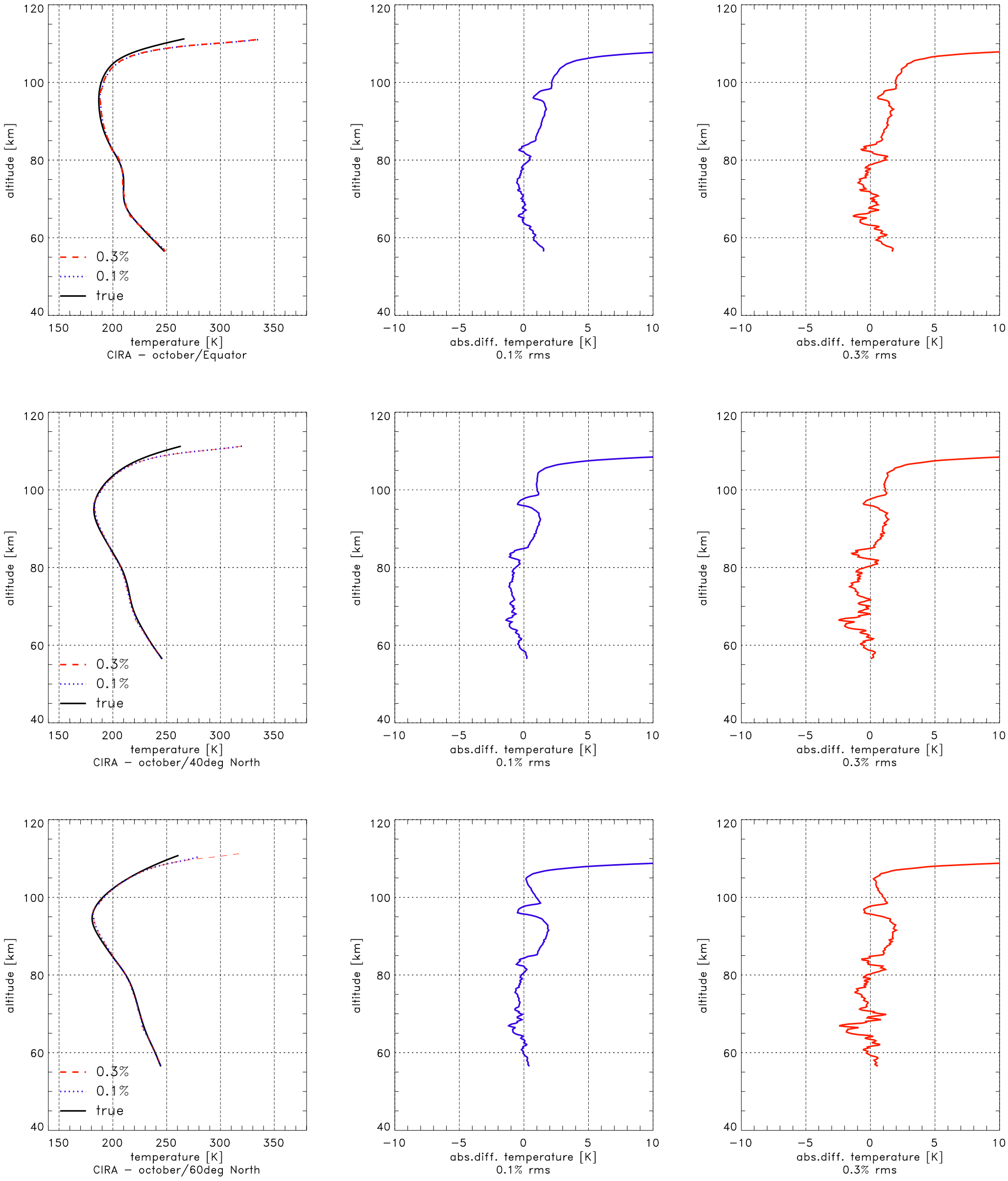

Figure 8.8. Temperature profiles resulting from the SMAS forward model and absolute departure of the retrieved atmospheric temperature for October/northern hemisphere. The blue lines refer the superimposed error of 0.1% and the red lines refer an rms-error of 0.3%, respectively. The black solid line in the left panel denotes the true case.

Summary & Conclusions

In this study — the ENVI-ATCHANGE Programme, Part 1 — the exploitation of data from two different occultation techniques was discussed and results show in general good performance. Stellar occultation with GOMOS on Envisat, once developed to monitor ozone, is now is in a phase were data became reliable and one can start to use them for long term trend studies. For SMAS, a solar occultation sensor concept, we showed its feasibility and presented results of a simulation study, which left us with the desire for a real mission in future. Comparing both instruments there is still a lot of potential for cross-validation and exploitation of retrieval techniques.

Part 2 of the ENVI-ATCHANGE Programme, proposed to ASA-BMVIT, is planned to start using the validated Envisat/GOMOS and MIPAS data for climate change monitoring and analysis.

GOMOS - Global Ozone Monitoring by Occultation of Stars

We developed an optimal estimation algorithm for retrieval of atmospheric profiles from Envisat/GOMOS-measured level 1b transmission data. In this study ozone and temperature profiles were retrieved, which is the primary focus of the algorithm, though the whole processing chain is capable of retrieving other trace gases (e.g., NO_2) simultaneously.

We applied refractive occultation retrieval to bending angle data from GOMOS star tracker data (SFA/SATU) gaining refractivity, density, pressure, and temperature profiles. This allows to improve the background fields required by the raytracing in the ozone retrieval part.

In conclusion, the approach adopted for an efficient retrieval of ozone profiles has yielded encouraging results for simulated data, with ozone profile accuracy <3% from mid stratospheric up to mid mesospheric regions. The application to real data clearly showed errors depending on transmission data quality and the selected star magnitude. The ozone retrieval performs best for bright stars (magnitude: -1.44 to 2) at low and mid latitudes for heights from 25 km to 65 km. There the signal coming from the measurement enables to accurately see ozone structures. Ozone profiles at high latitudes suffer from occultations for dim stars only, which leads to larger biases and higher standard deviations. Comparisons with ECMWF ozone profiles show biases of up to 20% throughout all latitude regions.

Simulated temperature errors based on optimally initialized bending angle profiles show a high retrieval quality with errors of <2 K below 35 km and <1 K below 25 km. Real GOMOS data was then incorporated successfully into our retrieval. GOMOS

SFA/SATU temperatures where compared to CHAMP, MIPAS, and ECMWF analysis data and showed rms-errors of 2 - 3 K from 25 km upwards. Below 25 km, temperature errors increase due to the small set of data available < 25 km as well as due to large fluctuations in SFA/SATU data.

SMAS - Sun Monitoring Atmospheric Sounder

The SMAS occultation sensor concept allows for a retrieval of the atmospheric key parameters temperature and ozone (amongst others), furnishes a good estimation of the atmospheric state in the mesosphere. The measured limb transmission data can be related to height profiles of the major absorbing species which are for the mesosphere, at middle ultraviolet wavelengths, molecular oxygen and ozone. Molecular oxygen profiles can be converted into pressure and temperature profiles. These data are of major importance for atmospheric analysis and process studies as well as for middle atmosphere modeling.

The SMAS retrieval algorithm computes robustly atmospheric data within the required accuracy (temperature errors less than 2 K at 2 km vertical resolution up to a height of about 100 km), including a realistic noise level. For a future work the SMAS transmission data should be processed with an optimal estimation algorithm similar to the one described in Section 3.2.1 for a verification of the results shown in these work. Furthermore the small nitric oxide photo dissociation structures near 191 nm and 183 nm (c.f. [43]), constituting the primary mechanism for NO_x removal in the middle atmosphere, should be regarded.

In summary, the SMAS sensor concept bears great capability to monitor mesospheric temperature and ozone for producing long-term stable data with high vertical resolution and accuracy.

Acknowledgments

The authors gratefully acknowledge discussions with and support by U. Foelsche, A. Steiner, M. Schwärz, A. Löscher, J. Fritzer, and J. Ramsauer (IGAM, Univ. of Graz, Austria). The European Space Agency is thanked for operating the Envisat satellite and for its related Announcement of Opportunity and free access to Envisat data, which was vital for this work. The data were accessed under Envisat AO project No. 620 (PI G. Kirchengast) and AO Projects led by IMK Karlsruhe (PI H. Fischer) and SA/CNRS (PI A. Hauchecorne), respectively. D.-Y. Wang and H. Fischer (IMK, Karlsruhe, Germany) and A. Hauchecorne (SA/CNRS, Verrières-le-Buisson, France) are thanked for their support to the project. We are thankful to V. Sofieva, J. Tamminen, and Erkki Kyrölä (FMI, Helsinki, Finland) for discussions and their contributions. We acknowledge G. Barrot, B. Theodore, and O. Fanton d'Andon (ACRI-ST, Sophia Antipolis, France) for helping with GOMOS data. Furthermore, we are grateful to J. Wickert and T. Schmidt (GFZ Potdam, Germany) for providing CHAMP occultation data. The authors are grateful to A. Hauchecorne also for his co-supervision of the Ph.D. thesis of C. Retscher, of which this work is a major part, and for hosting C. Retscher for a 6 month stay in 2001 at SA/CNRS. We thank C. Zehner and S. Casadio (ESRIN, Frascati, Italy) for discussion and support related to Envisat atmospheric payload products.

C. Retscher and C. Rehrl received financial support for the work from Envisat Project AO-620/Part-I funded by the Austrian Ministry for Traffic, Innovation, and Technology (BMVIT) and carried out under contract with the Austrian Space Agency (ASA).

List of Figures

List of Tables

Bibliography

[1] D.G. Andrews. *An introduction to Atmospheric Physics.* Cambridge University Press, 2000.

[2] M.L. Salby. *Fundamentals of Atmospheric Physics.* Academic Press, Inc, 1995.

[3] J.H. Seinfeld and S.N. Pandis. *Atmospheric Chemistry and Physics.* Wiley-Interscience, 1998.

[4] ACRI S.A. et al. GOMOS High Level Algorithms Definition Document. Technical report, ACRI S. A., France, Finnish Meteorol. Institute, Service d'Aronomie du CNRS, and Institut d'Aronomie Spatiale de Bruxelles, 1998. http://envisat.esa.int/support-docs/.

[5] P.B. Hays and R.G. Roble. Stellar Spectra and Atmospheric Composition. *Journal of Atmospheric Science*, 25:1142, 1968.

[6] G.R. Smith and D.M. Hunten. Study of Planetary Atmospheres by Absorptive Occultations. *Reviews of Geophysics*, 28:117–143, 1990.

[7] A.E. Hedin. A Revised Thermospheric Model Based on Mass Spectrometer and Incoherent Scatter Data: MSIS-83. *Journal of Geophysical Research*, 88:10170, 1983.

[8] A.E. Hedin. MSIS-86 Thermospheric Model. *Journal of Geophysical Research*, 92:4649, 1987.

[9] A.E. Hedin. Extension of the MSIS Thermosphere Model into the Middle and Lower Atmosphere. *Journal of Geophysical Research*, 96:1159, 1991.

[10] C.D. Rodgers. *Inverse Methods for Atmospheric Remote Sounding: Theory and Pratice.* World Scientific, Singapore, 2000.

[11] M.J. Rieder and G. Kirchengast. Error analysis and characterization of atmospheric profiles retrieved from GNSS occultation data. *Journal of Geophysical Research*, pages 31755–31770, 2001.

[12] J.L. Bertaux et al. Envisat/GOMOS An instrument for Global Atmospheric Ozone Monitoring. Technical report, ESA Publication Division, 2001. SP-1244 'Envisat - GOMOS'.

[13] E. Weisz. Temperature Profiling by the Infrared Atmospheric Sounding Interferometer (IASI): Advanced Retrieval Algorithm and Performance Analysis. *Wiss. Ber. 2/1998*, 2001. IGAM, University of Graz, Austria.

[14] G.F. Fjeldbo, V.R Eshleman, and A.J. Kliore. The neutral atmosphere of Venus as studied with the Mariner V radio occultation experiments. *Astronomical Journal*, 76:123–140, 1971.

[15] S. Sokolovsky and D. Hunt. Statistical optimization approach for GPS/Met data inversions. In *URSI GPS/Met Workshop*, Tuscon, Arizona, 1996.

[16] S.B. Healy. Smoothing radio occultation bending angles above 40km. *Annales Geophysicae*, 19:459, 2001.

[17] A. Gobiet and G. Kirchengast. Sensitivity of atmospheric profiles retrieved from GNSS occultation data to ionospheric residual and high-altitude initialization errors. Technical report, ESA/ESTEC No. 1/2002, 2002. IGAM, University of Graz, Austria, 58 pp.

[18] A. Gobiet, A.K. Steiner, C. Retscher, U. Foelsche, and G. Kirchengast. Radio Occultation Data and Algorithms Validation Based on CHAMP/GPS Data. Technical report, IGAM/UniGraz No. 1/2004, 2004. IGAM, University of Graz, Austria.

[19] C.B. Lang and N. Pucker. *Mathematische Methoden in der Physik*. Spektrum Akademischer Verlag GmbH, 1998.

[20] H.V. Storch and F.W. Zwiers. *Statistical Analysis in Climate Research*. Cambridge University Press, 1999.

[21] C. Retscher, G. Kirchengast, and A. Hauchecorne. Middle Atmospheric Ozone Sounding by the Envisat/GOMOS Stellar Occulation Sensor. In ISRSE, editor, *29th International Symposium on Remote Sensing of Enviroment*, 2002.

[22] G. Kirchengast. End-to-end GNSS Occultation Performance Simulator overview and exemplary applications. *Wissenschaftlicher Bericht 2/1998, IGAM, University of Graz, Austria*, 1998. IGAM, University of Graz, Austria, 138 pp.

[23] G. Kirchengast, J. Fritzer, and J. Ramsauer. End-to-end GNSS Occultation Performance Simulator Version 4 (EGOPS4) Software User Manual (Overview and Reference Manual). Technical report, Techniqual Report ESA/ESTEC-3/2002, University of Graz, Austria, 2002. IGAM, University of Graz, Austria, 472 pp.

[24] V. Sofieva, E. Kyrölä, M. Ferraguto, and GOMOS CAL/VAL team. From pointing measurements in stellar occultation to atmospheric temperature, pressure and density profiling: simulations and first GOMOS results. In IEEE International, editor, *Geoscience and Remote Sensing Symposium*, volume 5 of *IGARSS '03. Proceedings*, page 2990, 2003.

[25] GOMOS-ESL. ENVISAT-1 Ground Segment GOMOS Level 1b Detailed Processing Model. Technical report, ACRI, 1999.

[26] H. Fischer at al. Envisat MIPAS, An Instrument for Atmopheric Chemistry and Climate Research. Technical report, ESA Publication Division, 2000. SP-1299 'Envisat - MIPAS'.

[27] C. Retscher, G. Kirchengast, A. Gobiet, and A. Hauchecorne. Stratospheric Temperature and Ozone Sounding with Envisat/GOMOS Stellar Occultation. In *OPAC-1, First International Workshop on Occultations for Probing Atmosphere and Climate*, 2004.

[28] ESA SP1196(7). Atmospheric Profiling Mission. *ESA/ESTEC, Nordwijk, The Nederlands*, 7:58, 1996.

[29] G. Kirchengast, M. Gorbunov, N. Jakowski, L. Kornblueh, U. Mallow, A. Rius, C. Rocken, M. Rothacher, G. Schmidtke, M. Sust, J. Ward, and A. Wernik. ACLISCOPE-Atmosphere and Climate Sensors Consetellation Performance Explorer (ESA Earth Explorer Oppertunity mission proposal). *Wissenschaftlicher Bericht, IGAM, University of Graz, Austria*, 3:60, 1998.

[30] E. Neske, E.G. Schmidtke, and H. Wolf. Development of high sensitvity EUV silicon diodes. *Report FIPM Freiburg, Germany*, 1997.

[31] R.G. Roble and P.B. Hays. A Technique for Recovering the Vertical Number Density Profile of Atmospheric Gases from Planetary Occultation Data. *Planetary Space Science*, 20:1727–1744, 1972.

[32] P.B. Hays and R.G. Roble. Stellar occultations of molecular oxygen in the lower thermosphere. *Planetary Space Science*, 21:273–279, 1973.

[33] W. P. Chu, M.P. McCormick, J. Lenoble, C. Brogniez, and P. Pruvost. SAGE II Inversion Algorithm. *Journal of Geophysical Research*, 94(D6):8339–8351, 1989.

[34] J.D. Lumpe, C.S. Chang, and D. J. Strickland. Atmospheric Constituent Density Profiles from full Disk Solar Occultation Experiments. *Journal of Quantum Spetroscopy Radiative Transfer*, 46(6):483–506, 1991.

[35] K. Minschwaner, G.P. Anderson, L.A. Hall, and K. Yoshino. Polynomial Coefficients for Calculations. *Journal of Geophysical Research*, 10:10103–10108, 1992.

[36] M. Nicolet, S. Cieslik, and R. Kennes. Aeronomic problems of O_2 photo dissociation- V. Predissociation in the S-R bands of oxygen. *Planetary Space Science*, 37:427 – 458, 1989.

[37] L.T. Molina and M.J. Molina. Absolutte Absorption Cross Section of Ozone on the 185- to 350 nm Wavelength Range. *Journal of Geophysical Research*, 91:14501 – 14508, 1986.

[38] C. Rehrl and G. Kirchengast. Mesospheric Temperature and Ozone Sounding by the SMAS Solar Occultation Sensor. In *OPAC-1, First International Workshop on Occultations for Probing Atmosphere and Climate*, 2004.

[39] W.H. Press, S.A. Teukolsky W.T. Vetterling, and B.P. Flannery, editors. *Numerical Recipes in Fortran - Second Edition.* Cambridge University Press, 1992.

[40] S. Syndergaard. *Retrieval Analysis and Methodolgies in Atmospheric Limb Sounding Using GNSS Radio Occulatation Technique.* PhD thesis, Niels Bohr Institute for Astronomy, Physics and Geophysics, University of Copenhagen, 1999.

[41] A.K. Steiner, G. Kirchengast, and H.P. Ladreiter. Inversion, error analysis, and validation of GPS/MET occulation data. *Annales Geophysique*, 17:122–138, 1999.

[42] R.G. Brown and P.Y.C. Hwang, editors. *Introduction to Random Signal and Applied Kalman Filtering.* John Wiley and Sons, New York, 1997.

[43] K. Minschwaner and V. Starke. Photodissociation of nitric oxide in the middle and upper atmosphere. *Physical Chemistry of Earth manuscript, Department of Physics, New Mexico Institute of Mining and Technology, Socorro, New Mexico*, ST9.2-022:22, 2000.